Proton-Beryllium Interactions at 40 GeV/c

Rory Clarke

Thesis submitted for the degree of
Doctor of Philosophy

Heavy Ion Physics Group,
School of Physics and Astronomy,
University of Birmingham.

September , 2004.

Synopsis

The theory of strong interactions, Quantum Chromodynamics, predicts that the vacuum is not empty, but consists of a strongly interacting and complex structure of virtual quarks and gluons. Ordinary matter in the world around us is mainly made from hadrons, which themselves are made from quarks. It is thought that it is the vacuum that confines the quarks inside the hadron, and their interactions with the vacuum that gives the hadron 98% of its mass. It is predicted that at extreme pressures and temperatures there will be a phase change, where the vacuum 'melts' and the quarks are effectively free. This new state of matter is called the Quark Gluon Plasma (QGP). At the Super Proton Synchrotron at CERN, lead ions accelerated to relativistic energies, were collided with lead targets. During a collision of two lead ions it is possible that the QGP can be created under laboratory conditions here on earth. To detect the signals of plasma formation through the background of normal hadronic interactions is a challenging task experimentally.

This thesis is based on data taken in 1999 at the NA57 experiment. NA57 uses an enhancement of strange particles to detect plasma formation. A large enhancement in strange particle production in lead-lead interactions, with respect to proton-nucleon interactions, is considered a good probe of plasma formation. NA57 took data at two beam momenta, 40 GeV/c per nucleon and 160 GeV/c per nucleon. This thesis is concerned with the work done on the 1999 proton-Beryllium 40 GeV/c data which is used to normalise data from the NA57 40 GeV/c per nucleon lead-lead runs and calculate the strangeness enhancements at this energy. This thesis details the methods used to calculate corrected inverse slopes, see table 4.5, and final yields, see table 4.6 for the proton-Beryllium data for the Λ, $\overline{\Lambda}$ and K^0 signals. Enhancements in the NA57 lead-lead data have been seen when compared to the proton-Beryllium data and are shown in figure 5.1.

To

Mum, Dad, Richard and Nan.

Author's Contribution

The greater part of my analysis has been concerned with the extraction and correction of the Λ, $\overline{\Lambda}$ and K^0 signals from the 40 GeV/c, 1999, proton-Beryllium run. I developed the software, based on previous NA57 lead-lead data, to deal with the extraction and Monte Carlo corrections to this data. I have developed the weighting chain procedure to deal with the lower proton statistics, when compared with lead interactions. To take into account the distribution in the beam and primary vertex the extraction methods and weighting chain have been exhaustively developed and tested. Using the weighting chain and with efficiency tables calculated at Birmingham [1], I extracted inverse slopes and yields for the Λ, $\overline{\Lambda}$ and K^0 signals. I also investigated a number of background correction techniques and developed a combinatorial V^0 mixing method to perform a background subtraction on the $\overline{\Lambda}$, based on code from a previous lead-lead correction used by NA57, and corrected the $\overline{\Lambda}$ inverse slopes and yields for this background.

Other areas I have worked on involved combining the 1999 40 GeV/c data with data from the proton-Beryllium run 2001. This is currently ongoing at Birmingham. I developed techniques and software to allow the computer farms at Birmingham to decrease the amount of CPU time taken to process the weighting chain. I reviewed the current ideas involving the QCD vacuum in the context of the Quark Gluon Plasma. I have also helped during NA57 experimental runs at the SPS,CERN, to monitor the data-taking during shifts.

Acknowledgements

Always having lived in London, I remember first arriving at Birmingham University and how nervous I was. I worried about how I would fit in and with hindsight I would like to say that my concerns were unjustified. Over these past few years I have been privileged to meet people whose influence and friendship will shape my life for years to come. I will always look back at my time here with fond memories. Of course, none of this would be possible if it were not for financial support of the Government, administered by PPARC.

I would like to personally thank all the members of the Birmingham NA57 group for sharing with me their sheer genius and cunning in this subject, and the friendship and support that made it such a pleasurable experience. My supervisors, Dr. Orlando Villalobos Baillie and Dr. David Evans, deserve special praise for dealing with my constant questions and dilemmas with their usual natural good humour and deep insight and for their patience and time helping me prepare this thesis.

I also wish to thank Dr Roman Lietava for all of his help and skill which has been invaluable for my analysis and fellow student and colleague Stephen Bull whose friendship and determination has been both a blessing and a lifeline during some of the darker moments of the analysis.

The other members of the group have always been happy to share their time and help. I would like to thank Professor John Kinson, Dr. Frank Votruba, Dr. Gron Jones, Dr. Paul Norman and Dr. Ian Bloodworth for helping me over the years. I should also like to thank the other members of the NA57 collaboration for all their help at the collaboration meetings at CERN and via email. To the current NA57 students, Paul Bacon and Richard Platt, I wish them the best of luck in their studies.

The computing facilities here at Birmingham are second to none and this due to the dedication of Dr. Lawrie Lowe who has kept everything running like clockwork and who can generate solutions to seemingly impossible computing problems with the skill of a magician. I would also like to thank Simon Hands from Swansea University for his input and comments on the theory chapter of this thesis.

On a personal note I would like to thank Dr. Ray Rivers of Imperial College, University of London, who initially introduced me to this exciting subject. I would like to thank my tutors at the Royal Holloway and Bedford New College, University of London, for getting me this far. It would also be amiss not to mention my physics and chemistry teachers from Ramsden School, Mr. Reynolds and Mr. Townsend, whose passion for their subjects cut through that foggy teenage mist of girls and cars and inspired me all those years ago. Finally, I would like to thank my parents who always encouraged me, my brother who was always there when I needed him and Teo for our adventure and being more than I deserve.

Contents

List of Figures

List of Tables

Chapter 1

Introduction

The nucleus of an atom is made up of protons and neutrons which themselves are made from three quarks. The strong force, carried by gluons, binds the quarks. There are six types of quarks called, (with the lightest first), up, down, strange, charm, bottom and top with each having a corresponding antiparticle. They have spin 1/2, that is, they are fermions. Quarks carry fractional electromagnetic charge along with one of the three charges of the strong force, labelled by colour, called 'Red' 'Green' or 'Blue'. The antiparticles carry 'anti-colour'. Experimentally, free quarks have never been observed and it is found that all matter is made from colour singlet combinations of a quark and an anti-quark, (mesons) or three quarks (baryons). A table of the quark properties can be seen in table 1.1. Here the six 'flavours' of known quarks are listed along with their 'bound', or dynamical mass and their free or 'bare' mass which is only ever found indirectly from 'hard' quark-quark interactions. For bound hadronic matter, the baryon number and charge sum to integer values. Table 1.1 shows anti-quarks carry opposite sign, charge, baryon number and colour to quarks. Quarks also carry the following quantum numbers,

Table 1.1: Table of Quark Properties.

Flavour	Charge EM	Charge Colour	Baryon number	Mass (dynamical)	Mass (bare)
u=up	$+\frac{2}{3}$	R,G,B	$+\frac{1}{3}$	350 MeV/c^2	$\approx$ 5 MeV/c^2
d=down	$-\frac{1}{3}$	R,G,B	$+\frac{1}{3}$	350 MeV/c^2	$\approx$ 9 MeV/c^2
s=strange	$-\frac{1}{3}$	R,G,B	$+\frac{1}{3}$	550 MeV/c^2	$\approx$ 150 MeV/c^2
c=charm	$+\frac{2}{3}$	R,G,B	$+\frac{1}{3}$	1.8 GeV/c^2	$\approx$ 1.3 GeV/c^2
b=bottom	$-\frac{1}{3}$	R,G,B	$+\frac{1}{3}$	5.3 GeV/c^2	$\approx$ 4.3 GeV/c^2
t=top	$+\frac{2}{3}$	R,G,B	$+\frac{1}{3}$	No bound state known	$\approx$ 174 GeV/c^2

- Isospin, labelled +1/2 for u,d and -1/2 for $\bar{u}, \bar{d}$. Isospin is conserved under strong and electromagnetic interactions but can change under the weak interaction.

- The flavour quantum numbers, Strangeness, 'S', Charm, 'C', Bottom, 'B' and Top, 'T' are equal to zero for all quarks apart from the quarks that carry that name. The flavour quantum number is equal to -1 for Strange and Bottom quarks or +1 for the Charm and Top quarks, with the reverse labelling for their anti-quarks. These quantum numbers are conserved under strong and electromagnetic interactions but can change under the weak interaction. Isospin, labelled differently from these other quantum numbers, indicates that the masses of the u and d quarks are almost identical and they can be considered as degenerate states.

1.1 QED and Electric Charge

Quantum Electrodynamics (QED) describes quantised interactions of electromagnetic fields in the absence of gravity. Force between particles is exchanged in discrete packets called field quanta.

Quantum mechanics, (QM), allows the energy of empty space to fluctuate within the uncertainty of the time between interactions. The energy fluctuations on the fermionic field will result in electron-positron pairs that momentarily exist and then annihilate with each other. This phenomenon of QED is called a vacuum fluctuation as it happens in empty space in the presence of an electric field [2]. Even though these particles cannot be detected, they can be shown to exist through the Lamb Shift [3]. This is seen by measuring the $2s_{\frac{1}{2}}$ and $2p_{\frac{1}{2}}$ energy levels of the hydrogen atom. These two levels can be calculated from QM and would be degenerate if the potential were simply the Coulomb potential. However, at higher energies, i.e. as the electron is brought close to the nucleus, QED adds corrections to this potential via leading order diagrams. This predicts a shift of E/$\hbar$=1057MHz between these levels. This has been measured with an accuracy of better than 0.01% [4]. These corrections include a -27MHz effect coming from the interaction of the electron with the cloud of virtual particles that surround the hydrogen nucleus.

Now consider measuring the charge on an electron; far from the electron, where the vacuum is empty, the coupling constant for QED rapidly tends to $\alpha_{em} = \frac{1}{137}$ and the force on the test particle falls off as a Coulomb potential, see figure 1.1. As the test charge is brought closer to the electron it penetrates the cloud of virtual particles that surround it and feels the charge of the 'bare' electron. The coupling constant increases rapidly with decreasing distance as the higher order QED corrections are added and α_{em} is seen to increase rapidly as the test charge is brought closer. At distances greater than the atomic radius this 'bare' charge is being screened by the virtual particles that surround it. This can be seen in figure 1.1. The bare electron's charge is in fact the source of the virtual particles that screen it at large distances.

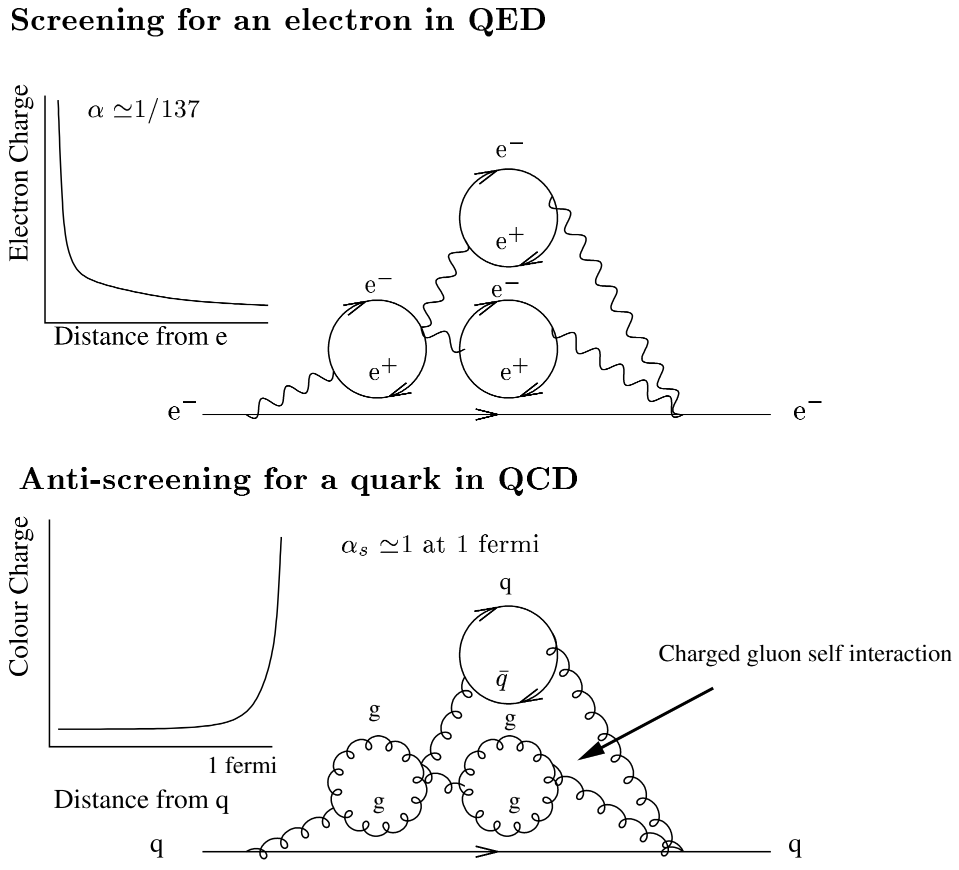

Figure 1.1: QED charge screening vs QCD colour screening.

1.2 QED, QCD and the Quantum Vacuum

Quantum Chromodynamics, QCD, is the field theory for the strong force of nuclear matter. In QCD there is not one but three charges, labelled, red, green and blue. In QED the force is carried by virtual photons, but in QCD force is carried by eight different colour charged field quanta called gluons.

An important difference between QCD and QED can be seen from looking at the structure of their Lagrangians. The Lagrangian is a bridge between classical and quantum mechanics. All of the interactions are 'contained' in a Lagrangian. In classical physics, if a group of particles and the forces between them are written in a Lagrangian form, the equation of motion of these particles is obtained by solving the Euler-Lagrange equations for each group of multiplied quantities. A similar case holds for the QED and QCD Lagrangians, where the particles and their interactions have been replaced with quantised fields [5, 6, 7].

The QED Lagrangian is given in equation (1.1). It is expressed in standard four-vector notation and we assume a summation over each pair of repeated indices. The first term describes a free quantised Electro-Magnetic, (EM), field in terms of the EM field strength tensor. The last term describes a free electron of mass m_e at rest. The middle term describes the interaction between the EM field and electron field.

In this example we are only interested in the first term, which is written out in terms of the four-vector potential $A^{\mu} = (\phi, \underline{A})$ in (1.2).

$$\mathcal{L}_{QED} = -\frac{1}{4}F^{\mu v}F_{\mu v} - \overline{\psi}_e\gamma^{\mu}\left[\partial_{\mu} + ieA_{\mu}\right]\psi_e + m_e\overline{\psi_e}\psi_e \qquad (1.1)$$

$$F_{\mu v} = \delta_{\mu}A_{\nu} - \delta_{\nu}A_{\mu} \qquad (1.2)$$

$$\mathcal{L}_{QCD} = -\frac{1}{4}\sum_{\alpha=1}^{\alpha=8} F_{\alpha}^{\mu v}F_{\mu v}^{\alpha} - \overline{\psi}_n\gamma^{\mu}D_{\mu}\psi_n + \sum_{n=1}^{n=N_f} m_n\overline{\psi_n}\psi_n \qquad (1.3)$$

$$F_{\mu v}^{\alpha} = \delta_{\mu}A_{\nu}^{\alpha} - \delta_{\nu}A_{\mu}^{\alpha} + C_{\beta\gamma}^{\alpha}A_{\mu}^{\beta}A_{\nu}^{\gamma} \qquad (1.4)$$

The QCD Lagrangian (1.3) is similar to QED. In the first term we do not have one EM field but eight gluons, numbered by the gluon colour index $\alpha = 1 - 8$. The last term describes not one fermionic electron but the free fermionic quark fields, with number of flavours, $n = 1, .., N_f$. The middle term uses simplified notation. In this case, the D^{μ} term is a more complicated object which, in essence, parallels the terms in the square brackets from the QED Lagrangian (1.1). If these were the only major differences between QED and QCD they would both behave in a similar fashion for electron or quark interactions. However, if we expand the gluon field tensor as we did before we see there are now three terms in equation (1.4) compared to two in equation (1.2). The final term in equation (1.4) is a self interaction between the gluon quanta. This allows the gluons to interact, unlike the uncharged photons in QED, see figure 1.1. This self interaction of the Gluons has some dramatic consequences for the theory of QCD, one of which is the concept of the QGP.

1.3 The Strong Coupling Constant, Confinement and Asymptotic Freedom

The coupling between quarks and gluons, and gluons and gluons, is determined by the strong coupling constant, see equation (1.6). This is not constant but linked to the nature of the vacuum interactions via a process called 'renormalisation' [3]. For empty space, i.e. at low energy, this strong coupling is found to be very close to one for the vacuum fluctuations of gluons [8]. The strong coupling and colour charge of the virtual gluons produced in a vacuum fluctuation means they will themselves be surrounded by a strong gluon field from equation (1.4). There is no mass barrier for a massless virtual gluon to produce secondary gluons, and the gluons they produce will have just as strong a field, surrounding themselves in turn with gluons, and so on [3]. This self interaction of the virtual gluons and the strong coupling constant makes the empty QCD vacuum unstable [9, 8]. Virtual gluons will propagate out and polarise the QCD vacuum within the period allowed by the uncertainty relation. In QCD, these domains of virtual gluons form to minimise the overall energy of the vacuum [8]. There are many ways to do this and the low temperature QCD vacuum has a complex 'foam-like' structure that is changing all the time called the gluon condensate.

Consider trying to add a colour charge, say a red quark to this vacuum. The strong red gluon field surrounding the quark will polarise the local QCD vacuum. This will take energy in order to overcome the current polarisation. As the local area is polarised, the increased local red charge will now be interacting with more of the already polarised gluon vacuum, requiring more energy. The red charge of the gluon field will propagate out, converting the whole of the vacuum to this charge; but it would require an infinite amount of energy to do this. However, if there were a 'sink' for charge, say a nearby anti-red quark, the colour polarisation would remain local and the overall neutral colour of this combination will disturb the vacuum less. The minimum disturbance to the vacuum is achieved with the gluon flux between the two quarks confined to a 'tube' structure and not spreading out, called a 'colour flux tube'. This would allow a quark-antiquark pair to be added to the vacuum with a finite amount of energy. This combination is a meson, a bound state of a quark and antiquark with overall neutral colour charge. The other combination is three quarks, the baryon. The gluon self interaction (1.4) and the strong coupling constant (1.5) restrict the addition of coloured quarks to the QCD vacuum to colour neutral combinations. Furthermore, as the quarks are separated, the minimum disturbance to the already polarised vacuum will confine their own gluon exchanges to colour flux tubes. As the quarks are separated, the greater the force needed to exclude the current vacuum polarisation and keep the local vacuum polarised to the quarks own colour field. A simple analogy is the stretching of a rubber band. The gluon field is said to have an 'anti-screening' effect compared to the 'screening' effect of QED where the virtual photons can spread out into the vacuum and the force drops, as the Coulomb force, with increasing separation. From figure 1.1 and equation (1.6) the coupling between the quarks increases as the inverse log of distance at a separation of around 1fm. In the QCD vacuum, quarks will need more energy to be separated as the distance between them increases and they will be effectively confined. The QCD vacuum is said to 'abhor colour charge' and quarks are confined to distances less than 1fm.

1.3.1 Asymptotic freedom

The QCD coupling constant for the strong force 'α_s' between two quarks is given by equation (1.5) where n_f is the number of flavours, and Q^2 is the relative momentum between the source and probe quarks. From the uncertainty relation, in natural units, $Q^2 = \frac{1}{r^2}$ equation (1.5) can be written in terms of the coupling as a function of separation r^2 shown in (1.6). Λ^2 is a scale parameter from renormalisation found from experiment. As $r \rightarrow \frac{1}{\Lambda}$ there is an 'infrared divergence'. This divergence is very strong close to the value of Λ and indicates strong quark confinement as $\alpha_s \rightarrow 1$. From experiment this value of Λ is found to be around the typical mass of the lightest hadrons, $\approx$ 200 MeV, giving the maximum separation of the quarks of an order $r \approx$ 1fm as seen in figure 1.1. As the distance between the quarks is decreased, the value of α_s will tend to zero as the inverse log of distance between the quarks. The coupling between the quarks and gluons tends to zero and they act as if they are free fields. This is called Asymptotic Freedom.

$$\alpha_s(Q^2) = \frac{12\pi}{(33 - 2n_f)\log(\frac{Q^2}{\Lambda^2})} \tag{1.5}$$

$$\alpha_s(r^2) = \frac{12\pi}{(33 - 2n_f)\log(\frac{(1/r)^2}{\Lambda^2})} \tag{1.6}$$

1.3.2 The QCD Vacuum and Quark Mass

A proton is made up of a uud quark combination but has a mass of 1 GeV, about 50 times the bare mass of the quarks in table 1.1. It is thought that this mass, some 98% of the mass of the proton, comes from the interaction with the vacuum quark fields. Along with the previously discussed gluon vacuum fluctuations there will also be quark-antiquark pair fluctuations of the vacuum. Again, consider adding a test probe quark to this vacuum. The quarks are fermions with spin 1/2 and will have a helicity, or 'handedness'[8]. If our 'probe' quark is a left-handed quark it can annihilate with a left-handed anti-quark from a virtual pair. This will liberate the pair's right-handed quark partner. From the observer's point of view we see a left-handed quark spontaneously transform into a right-handed quark and helicity is not conserved. It can be shown that for helicity to be conserved the quark must be massless and hence moving at the speed of light. The QCD vacuum has given the quark dynamic mass, see top figures in 1.2.

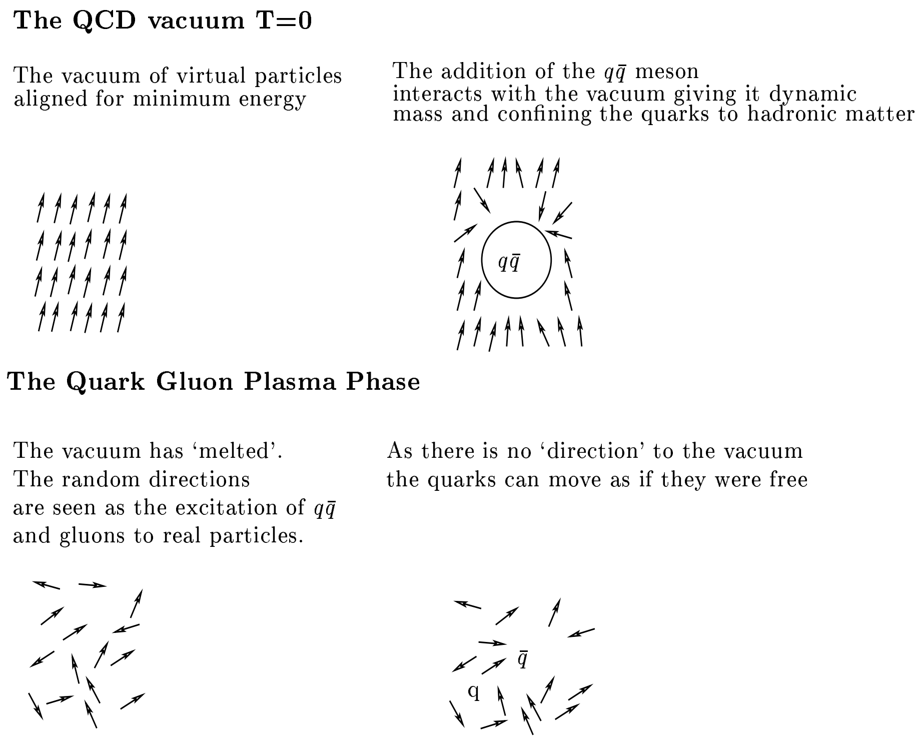

Figure 1.2: The QCD Vacuum

1.4 The Quark Gluon Plasma

As we increase the kinetic energy of the real quark interactions they will act more violently with their interactions on the vacuum gluon and quark-antiquark pairs. These interactions will give the virtual particles kinetic energy and there will be a phase change when these interactions excite the virtual particles to have enough energy to become real, physical, particles [10]. This phase change is similar to the ferromagnet taken over the Curie temperature T_c, where the magnetisation is lost. The vacuum is said to have melted. In fact there are two phase changes, the melting of the gluon vacuum and the melting of the quark vacuum. From lattice QCD calculations it seems that these phase changes happen at the same point but the question is still undergoing strong theoretical investigation [9]. The melting of these two vacua will have very different effects. As the gluon condensate melts, there will be no colour neutral vacuum to confine the interactions between the quarks. The anti-screening with distance will cease, see lower figures in 1.2, and quarks will no longer be confined by the strong force. As the quark-antiquark pair vacuum melts, the quarks will no longer interact with the vacuum pairs and change helicity. In this phase they will no longer gain mass from moving through the vacuum and their mass will drop from their dynamical mass to their current, or bare mass [11]. This is called Partial Chiral Symmetry Restoration. If Chiral Symmetry is restored the helicity will be a good quantum number and will be conserved during interactions, but this argument still needs some clarification as helicity is only a good quantum number for massless particles. From table 1.1 it is seen that the bare masses of the quarks are not zero. However, for the up, down quark, this 'bare mass' is much less than the average Kinetic Energy (K.E) of the quark in the fireball. This can be seen by considering the average energy of quarks in the QGP. In a typical 160 GeV/c heavy ion collision in a laboratory, in units where the Boltzmann constant = 1 and temperature is measured in MeV, $\mathrm{T}_{fireball} = \mathrm{K.E}_{partons} \approx 200\mathrm{MeV}$. Up or down quarks will have a bare mass $\approx 5 - 9\mathrm{MeV}$, which is much less than 200 MeV, and we can assume that they are effectively massless when compared to their K.E. This is not quite so true for the strange quark with a bare mass of 150MeV, so dynamic Chiral Symmetry Breaking is effectively removed. In this phase, where quarks are deconfined and reduced to their bare mass, a QGP is said to have formed.

1.5 Cosmology, Mass and Heavy Ion Collisions

It is thought that the early Universe was in the QGP phase. The experiments with heavy ion collisions will allow us to study a 'micro-bang' in a laboratory. However, there are some differences that have to be considered: there are no gravitational forces to slow the micro bang; the QGP of the early Universe would have lasted for about 10^{-5} of a second, 10^{18} times longer than the micro bang [9]. The longer lifetime of the early Universe would allow weakly interacting particles to thermalise inside the plasma, changing the properties of the phase transition. Another difference to consider would be the initial baryon number, see table 1.1. The early Universe would have close to zero baryon number, i.e. matter-antimatter symmetry up to one part in 10^9. Collisions with ions contain no initial valence anti-quarks and therefore have large initial baryon number densities.

It is possible that the cores of neutron stars are in the QGP phase. In this case, the phase transition from hadronic matter to QGP is carried via the overall baryon number density instead of temperature. Matter is crushed in the core of a star until the shells of the nucleons overlap and 'melt'. This is expected to happen with matter compressed to around four times nuclear density [9].

Finally, the QGP gives a unique probe into the world of the vacuum. At T=0 the vacuum is not empty but a highly complex structure composed of virtual quarks and gluons. As previously mentioned, some 98% of the mass of a hadron, i.e. all the matter we see around us, comes from the interactions with this vacuum. At $T \rightarrow T_{QGP}$ the vacuum is expected to 'melt' into a simpler structure, the QGP, see bottom diagrams in figure 1.2. The experimental results from these studies have a direct bearing on the current theory surrounding this complex subject.

1.6 Results from QCD

The magnetic field of a ferromagnet does not gradually diminish as it is heated but spontaneously changes at a point when the spins in the magnet can no longer align themselves due to the thermal motion of the atoms. From lattice QCD and statistical physics calculations, such as the MIT Bag Model [9] a similar thing is predicted for the QCD vacuum. When the energy scale decreases the QCD coupling constant increases. This leads to a breakdown of QCD as a perturbation theory (1.5). Because of this, perturbation methods, which require a coupling much smaller than unity, and which have been so successful in QED, cannot be used with QCD to model 'soft', i.e. large separation r or low quark momentum transfer Q^2 processes. To model the phase change for a QGP other methods have to be used to investigate matter under these conditions. One method is to divide spacetime into a lattice. The system is then mapped onto this lattice of discrete space time points and the QCD equations (1.3) with $\alpha_s \rightarrow 1$ can be solved numerically avoiding the problem of non-converging solutions with perturbative methods. However, it requires the use of very powerful computers to solve even simple problems. It was results from lattice QCD investigating the asymptotic freedom for quarks at high energies that led to the idea of a QGP [9].

1.6.1 Temperature of the Phase Transition

Hadrons can be represented as free quarks and gluons that are confined in a 'bag' surrounded by a QCD vacuum [12, 13, 14]. The QCD vacuum is colour neutral so coloured quarks and gluons cannot appear outside the bag. Inside the bag the vacuum has melted and they are free to move. Outside the bag the QCD vacuum exerts a pressure on the bag which must be equalised by the kinetic energy of the quark gas inside the bag.

When the pressure of a hadron gas, '$P_{\text{Hadron Gas}}$', is equal to or greater than the bag pressure confining the quarks, 'P_{Bag}', the hadrons will melt to form the QGP, 'P_{QGP}', see equation (1.7).

$$P_{QGP(critical)} = P_{\text{Hadron Gas}} - P_{Bag} \tag{1.7}$$

Even though this is a highly simplified model it gives a QGP transition temperature of the right order. For massless u and d quarks and a typical hadron with a 'bag constant' of 500MeV/fm^{-3} this transition temperature is estimated to be 144 MeV or $1.67 \times 10^{12} K$ where 1MeV = 1.16×10^{10}K[15]. One of the main assumptions of this model is that the phase transition will be of first order. This may not be true in reality [16]; however it is less than the equilibrium temperature in a typical Pb-Pb collision, which is approximately 200 MeV at the SPS, suggesting that a QGP could be produced in a laboratory.

1.7 The QGP Phase Diagram

It is found that a phase transition could be caused by sufficiently large energy densities or for sufficiently large baryon number densities (baryochemical potential). In a heavy ion collision or the early universe the phase transition is caused by conversion of kinetic energy into heat, i.e mainly by entropy. The other possibility is a 'cold QGP' could form in the centre of a neutron star from a high baryochemical potential, shown as 'μ_b' along the X axis of figure 1.3, as matter is crushed under the influence of gravity at the centre of the star, increasing the baryon number density. Figure 1.3 shows the phase space of the various stages of quark matter. The vertical axis shows the average KE of the partons, or the temperature, and the horizontal axis shows the baryochemical potential. The QGP phase could be found at around three to four times nuclear density in the region 'neutron stars' [9]. The region of Chiral Restoration marks the transition from dynamic to bare quark masses for the up down and strange quarks. It is expected that there is a mixing of hadronic and

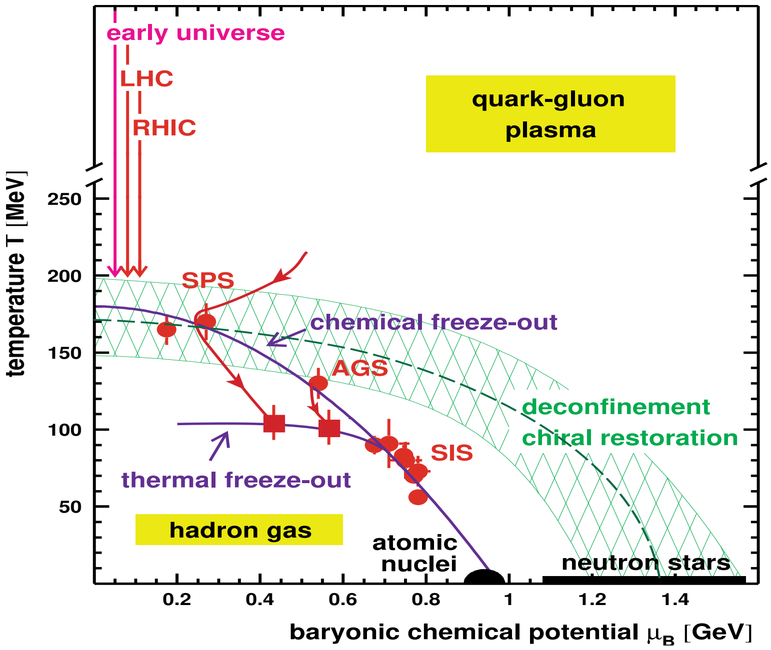

Figure 1.3: A phase diagram for the QGP

QGP phases during this transition as shown by the hatched region.

1.7.1 Chemical and Thermal Freeze Out

There are two transition regions called Chemical and Thermal freeze out. Chemical freeze out marks the point below which inelastic collisions cease and the flavour content of the system is fixed. This is not identical to the QGP phase boundary as the hadron gas may still have enough energy density for inelastic flavour changing interactions. The boundary of thermal freeze out marks the point where elastic collisions are expected effectively to cease.

1.8 Creating a Plasma in the Laboratory

The Super Proton Synchrotron (SPS) at CERN [17] can accelerate lead ions to 99.99 % of the speed of light, with a momentum up to 160 GeV/c per nucleon. The colliding lead ions will form a 'fireball' that should allow enough of the initial kinetic energy to interact long enough for the system to reach a thermodynamic equilibrium via secondary interactions. It may reach equilibrium via interactions of colliding nucleons, forming a hadron gas, or, if the energy density is high enough, via a plasma of interacting quarks and gluons. This latter stage is called the Quark Gluon Plasma or 'QGP'.

Partons within the interaction region will rapidly thermalise and the fireball will have a temperature. The temperature reached in the fireball from a Pb-Pb collision at the SPS, is expected to be around 2.9 x 10^{12} K or 250 MeV [9]. This is a hundred thousand times hotter than the centre of the Sun. Under these conditions, it is predicted that matter undergoes a phase transition to the exotic new state of matter, the QGP [17].

This is shown in figure 1.4. The Y axis shows time and the X axis shows the distance between two colliding lead ions. In the lower diagram 1, two colliding lead ions are shown in the centre-of-mass frame. The ions are travelling at relativistic velocities and are Lorentz contracted along their length. In this diagram the ions are shown colliding head on, or at maximum 'centrality', a collision of this type will have the maximum number of wounded nucleons or 'participants'. A majority of the time the collisions will only be peripheral, with a lower number of wounded nucleons or participants. Diagram 2 shows the time after a collision, the QGP, shown as the central hatched region, only exists for about 5×10^{-23} s before rapid expansion cools the fireball and the quarks and gluons recombine via a phase change into a hadron gas. This is shown in diagram 3, Hadronic interactions are shown as the outer

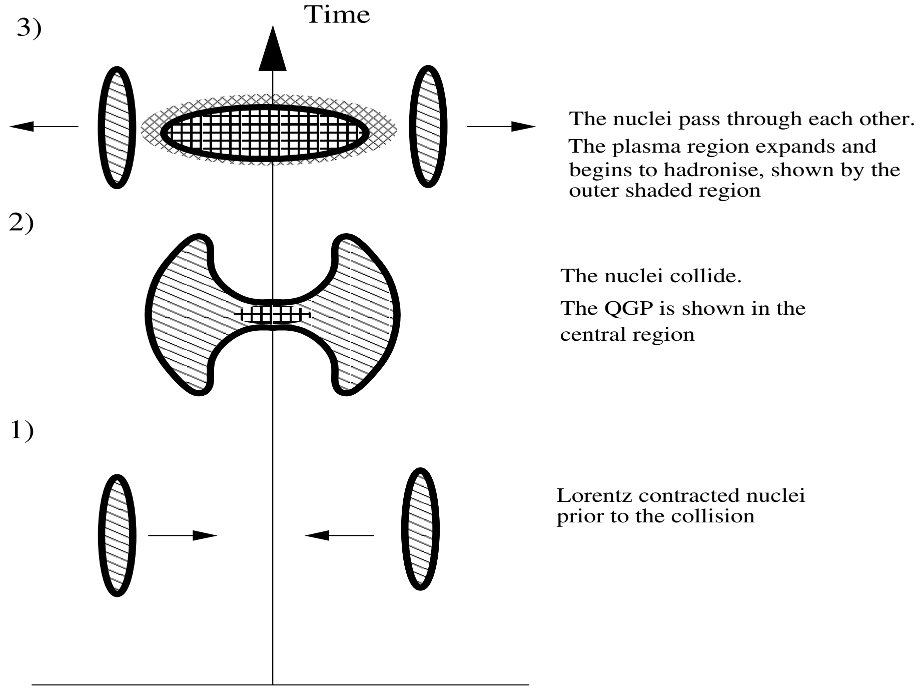

Figure 1.4: QGP formation in the CM frame at different times.

hatched region. Hadronic interactions can still occur in this gas between chemical freeze out and deconfinement in figure 1.3, until about 10^{-22} s when inelastic interactions cease. However, the time required for a hadron gas to reach strangeness equilibrium is about 10^{-21}s, 10 times longer than the hadron gas phase, and this enables us to use hadrons as a probe for QGP formation.

1.8.1 Stopping

In the heavy ion experiments at RHIC and at the SPS beam energies, moving from higher to lower beam energies seems to increase the baryochemical potential of the fireball. This can be clearly seen in figure 1.3 and the phenomenon is referred to as 'Stopping'. The colliding gold or lead ions have high baryon numbers and if the collision is at a very high energy their quarks will have very high longitudinal momentum. In this case, the valence quarks will be found at a higher rapidity, or smaller angles with respect to the beamline, see appendix A. Secondary particles that are created at central rapidity, the region of the fireball, will form with overall zero baryochemical potential. In the lower energy experiments the quarks in the colliding ions lose this longitudinal momentum in the collision process, giving rise to a non-zero baryochemical potential in the central rapidity region.

1.9 Signals of Plasma Formation

Experiments with heavy ions can map the phase space around the expected QGP transition temperature to see what happens at these energy densities. To detect the formation of a plasma experimentally is a challenging task. In a typical example, two lead ions colliding at 160 GeV/c per nucleon incident momentum will produce a multiplicity of some 1800 charged tracks from which signals for the QGP have to be extracted against a large background of normal hadronic interactions. To detect and investigate the formation of this new state of matter, a number of methods have been developed that remain unaffected by the strong interactions in the hadron gas stage. These methods use electromagnetic interactions, techniques that exploit flavour conservation, momentum distributions and regions of correlated charge to probe the QGP region. These methods can be used alone or combined to give a clear picture of the processes that occur during plasma formation.

1.10 DCCs

An indirect method of detecting a QGP would be the formation of Disordered Chiral Condensates (DCCs) [18]. The low mass of the pion, 140MeV, means that it is produced in copious quantities in a heavy ion collision. There are three 'flavours' identifiable by their charge, π^+, π^0 and π^-. In a pure hadronic reaction there should be no preference for the type of pion emitted and π^+, π^0 and π^- should be found with equal probability.

However, the case for a QGP could be different. When the lead ions collide the nucleons will initially be in a highly excited state and far from equilibrium. It is possible that local instabilities from the non equilibrium stage will cause regions of spontaneous 'alignment' of isospin as the QGP forms and the quarks return to their bare mass i.e.. chiral symmetry is restored. From the perspective of a ferromagnet as an approximation to the QCD vacuum, a phenomenon seen at the critical point of the phase transition is that the spins will start to align and random clusters of spins start to oscillate in unity [19, 15]. A similar effect is expected with the production of excited particles from the vacuum at the critical point. Oscillations in a quark vacuum will form domains in the rapidly expanding plasma. These local domains would expand in the plasma as regions of correlated up and down quarks that would hadronise as regions of correlated pions.

If this occurs then one could observe events where there is a strong correlation between the emitted pions. On hadronising there would be regions of neutral pions π^0 and regions of charged pions π^+, π^- emitted and this could be indicated by looking at the ratio of neutral to charged pions from equation (1.8) [20].

$$\frac{\pi^0}{\pi^+ + \pi^0 + \pi^-} \neq \frac{1}{3} \tag{1.8}$$

The idea of a DCC was first proposed to explain rare events observed in cosmic ray experiments [21] called Centauro and Anti-Centauro events where, in the former, there is a deficit of neutral pions and the latter predominantly neutral pions.

1.11 J/ψ Suppression

A direct signal of plasma formation could be the suppression of the bound $\overline{c}c$ system, J/ψ [22, 23, 14] studied in experiments NA50, NA38 [24, 25]. Charm quarks are formed during the initial stage of a collision when the ions just 'overlap'. This pre-thermal equilibrium stage is the point where hard partonic interactions occur, needed to create $\overline{c}c$, see figure 1.5 and table 1.1. If the collision is fairly central,

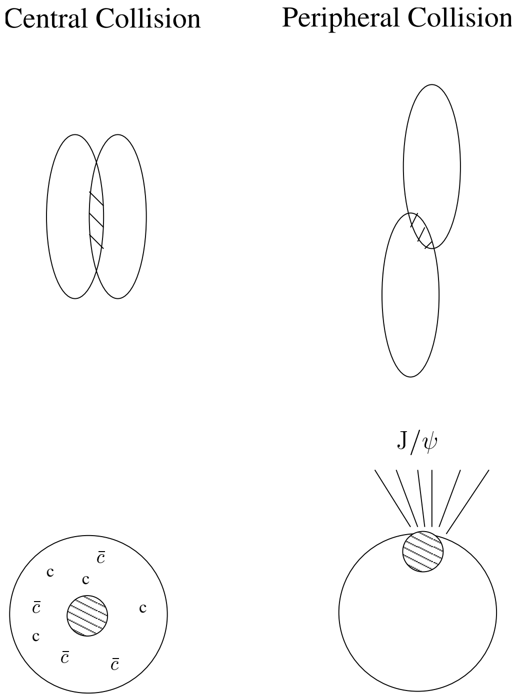

Figure 1.5: J/ψ suppression

i.e. almost head on, a surplus of $\overline{c}c$ will be found at the centre of the plasma. A fraction of these charm pairs can form a J/ψ but as they pass through the QGP, colour screening, an effect analogous to Debye screening, will 'melt' the J/ψ and the signal will be suppressed. This suppression will be a function of the centrality of the colliding ions [9]. A more central collision will result in the charm coming from deeper inside the plasma with a greater J/ψ suppression. Suppression has been seen in the NA50 experiment by a factor of about two [26]. In early work on $J\psi$ suppression it was argued that a suppression may be explained by J/ψ absorption within a dense hadron gas such as shown by equation (1.9).

$$J/\psi + \pi \longrightarrow D + \overline{D} + X \tag{1.9}$$

However, these effects can be accounted for and the data shown in figure 1.6 have excluded this possibility by normalising the data to the expected hadronic suppression. There is a significant suppression after about 2.5 GeV/fm^3 with the increasing 'step-like' pattern after about 3.2 GeV/fm^3 seen in the Pb-Pb data. The large suppression and step like structure indicates a phase transition into a QGP has taken place [26]. At the higher energies available at RHIC and the LHC, it is expected that there could be less suppression as copious $c\bar{c}$ quark pairs are produced in the plasma, increasing the probability of J/ψ production [9]

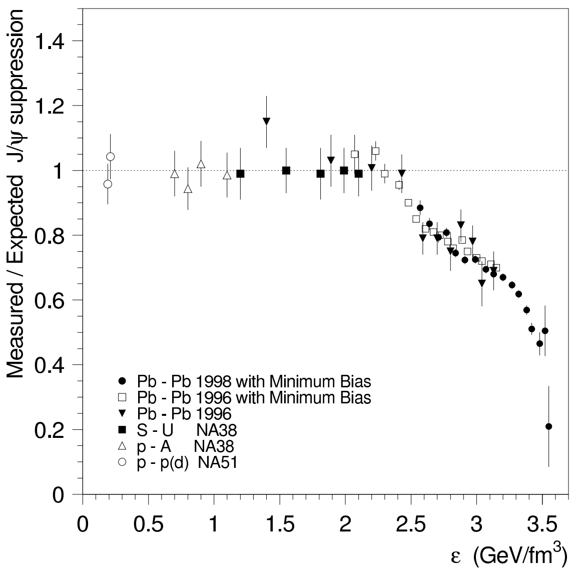

Figure 1.6: J/ψ yield (points) normalised to the yield expected assuming only hadronic suppression (dotted line) as a function of energy density. The decreasing yield of J/ψ after about 2.5 GeV/fm^3 indicates the formation of a QGP.

1.12 Jet Quenching

Consider a quark pair given kinetic energy through a collision. As the quark pairs separate α_s will increase as indicated in equation (1.6), decelerating the two quarks. Acceleration of a charged particle will produce radiation; in QCD the decelerating quarks will produce gluon radiation and a shower of quarks that, in turn, will produce hadrons. In a proton-proton type collision such a two quark event will be seen as a pair of back to back jets [3]. If these jets were formed in a QGP they may dissolve as they pass through the plasma, giving fewer jets compared to a system where a plasma did not form. If the jets formed outside the plasma and one of the jets passed through the plasma, the plasma could dissolve it, leaving an asymmetrical system of jets. A study of this was done recently at RHIC using Gold Gold (Au-Au), Deuteron Gold (d-Au) and p-p collisions [27]. Colliding d-Au is similar to a proton neutron collision and jets formed as normal, showing that nuclear effects did not bring about quenching, but colliding Au-Au is expected to form a QGP which would affect the jets as they passed through it. It was found that the away-side jets in the Au-Au collisions were being suppressed when compared to p-p collisions, see figure 1.7. These jet suppressed events indicate that the away-side jets have been absorbed passing through the QGP [27].

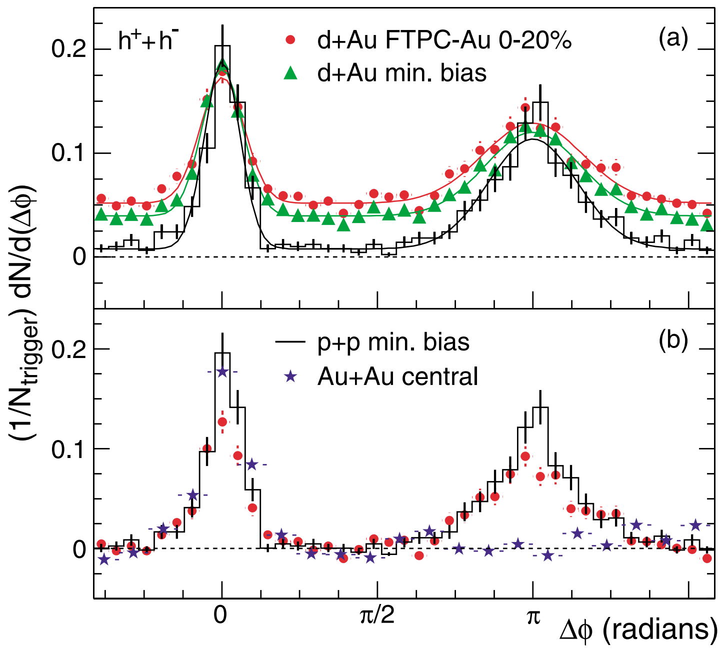

Figure 1.7: Jet quenching at RHIC. Figure (a) shows two jets from d-Au collisions, with no expected QGP formation. Figure (b) shows suppression of the away-side jet with central Au+Au collisions (Star markers) compared to p+p (Line), explained by jet quenching from QGP formation

1.13 High Pt Suppression

Particles with high transverse momenta, $P_t > 2\mathrm{GeV}/c$, are produced early on during a collision. In a proton-proton type collision this results in jet production, but if a QGP forms the partons' energy will be damped as they transverse the medium. Experimentally this will be seen as a suppression of the high P_t region when normalised to the proton-proton interaction. This is seen in figure 1.8. Here the Au-Au and d-Au yields (R_{AB}), interactions have been normalised to the number of wounded nucleons and scaled to proton-proton yields (R_{NN}), giving the ratio,

$R = \frac{Yield(AB)}{No_{coll(AB)}.Yield(NN)}$. From this figure we see an enhancement of the d-Au. This

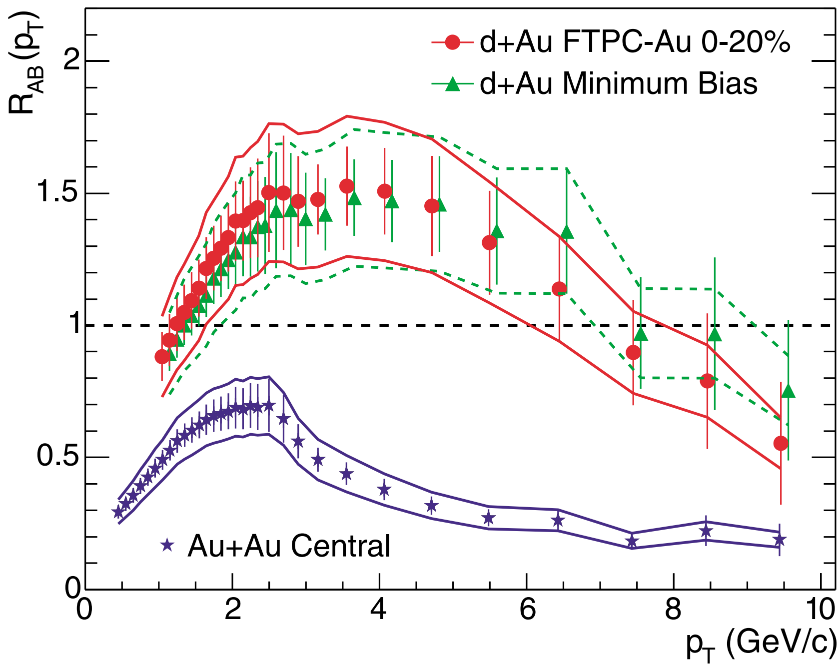

Figure 1.8: High P_t suppression at RHIC

effect is understood as a manifestation of the Cronin Enhancement [28] seen in p-N collisions. However, there is a suppression of single particle production at all P_t for the Au-Au interactions and this is most easily understood via the mechanism of QGP formation [27].

1.14 Direct Photons

Photons do not feel the strong force and will escape the plasma unaffected, acting as a direct signal of its formation. They are produced in a plasma through the process of [14] $q\bar{q} \rightarrow \gamma q$ and $gq \rightarrow \gamma q$. Direct photons and leptons would allow the initial moments of the collision to be studied but are difficult to detect due to the large background from particle decays, principally that of the π^0. There could be a detectable excess of direct photons within the transverse momentum range of $1 \leq P_t \leq 3$GeV/c, where the signal-to-background ratio is optimal.

1.15 Dilepton Enhancement

Leptons produced in the plasma will also escape without interacting with the strong force and act as a direct signal of plasma formation. Single leptons would not be detectable due to the high background from hadronic decays, the main background coming from $\pi^{\pm}$ decays, but dileptons may be detectable [29]. A lepton pair can only be formed from the virtual photon when a quark and anti-quark collide in the QGP. This process is identical on a quark level to the hadronic scattering of a π^{+} and $\pi-$ which forms leptons via the Drell Yan mechanism which will be a considerable source of hadronic background for this signal, see equation 1.10.

$$q\overline{q} \rightarrow \text{Lepton}^{+} + \text{Lepton}^{-} \tag{1.10}$$

The masses of the light mesons, such as the ρ with a mass of 0.769 GeV [30], would shift to a lower value if chiral symmetry were restored and they would be created more easily in the QGP. If the lifetime is short enough to decay inside the QGP the dilepton signal would be enhanced. In figure 1.9, the measured yields are compared to the expected yield from hadronic decay channels and an enhancement can be seen between 0.2-0.7 GeV/c^2, possibly coming from reduced mass ρ decays. A similar enhancement has been seen with dimuons between 1.6 and 2.5 GeV/c^2 in the NA50 experiment. This range is referred to as the Intermediate Mass Range, or IMR. This mass range, between the mass of the ϕ and J/ψ, is a non-resonant part of the spectrum where signals from enhancement in charm quark production or thermal dimuons, from the QGP, may survive. An enhancement of dimuon production in Pb-Pb at 158 GeV/c and S-U at 200 GeV/c with increasing participants, relative to proton-nucleon collisions is seen in this mass range, suggesting the formation of a fireball in these collisions, see left hand plot of figure 1.10. In the right hand plot the mass spectrum of dimuons for Pb-Pb at 158 GeV/c has been fitted with various estimated parameters. The closest fit to the observed data comes when fits for thermal and increased charm contributions from an expanding fireball are added, shown as the solid dark line [31]. The data shows an enhancement of dimuons but more detailed work will be needed to measure open charm production directly before final conclusions can be drawn from this type of analysis. Open charm production data are currently being analysed by the NA60 experiment [32, 33] that will help to understand the physical mechanism behind these observations.

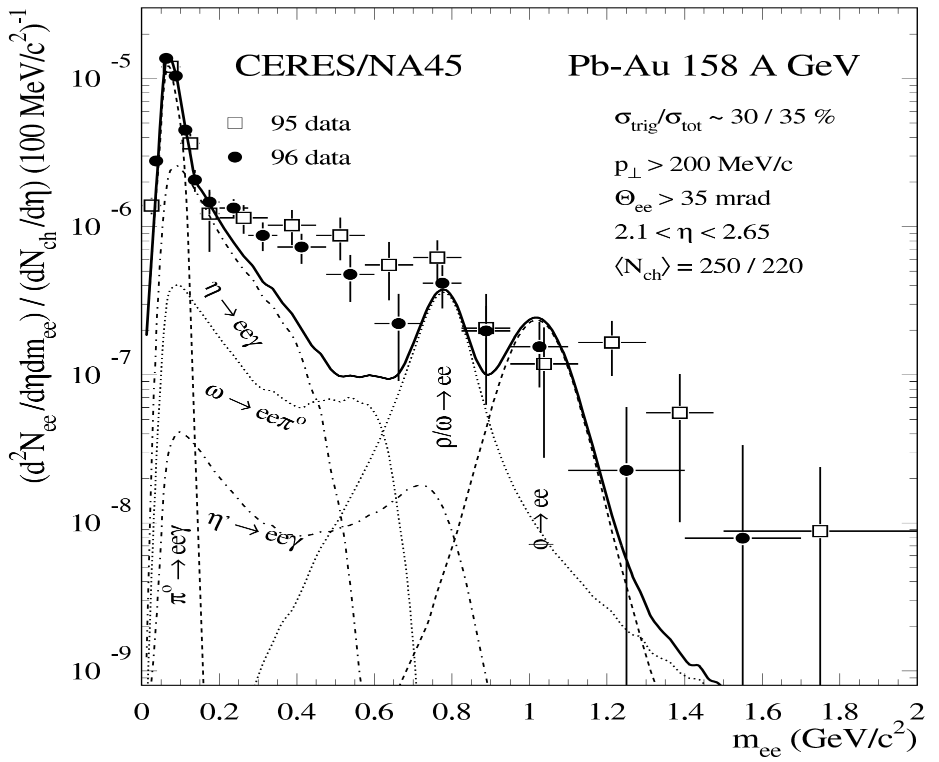

Figure 1.9: Light meson dilepton enhancement in NA45. The yields were normalised to the number of charged particles per event and plotted vs. e^+e^- mass. Expected yields from different hadron decays are shown. The strong excess for the region $0.42 < m_{ee} < 0.7$ GeV cannot be accounted for by hadronic decays, suggesting a possible shift in the ρ mass.

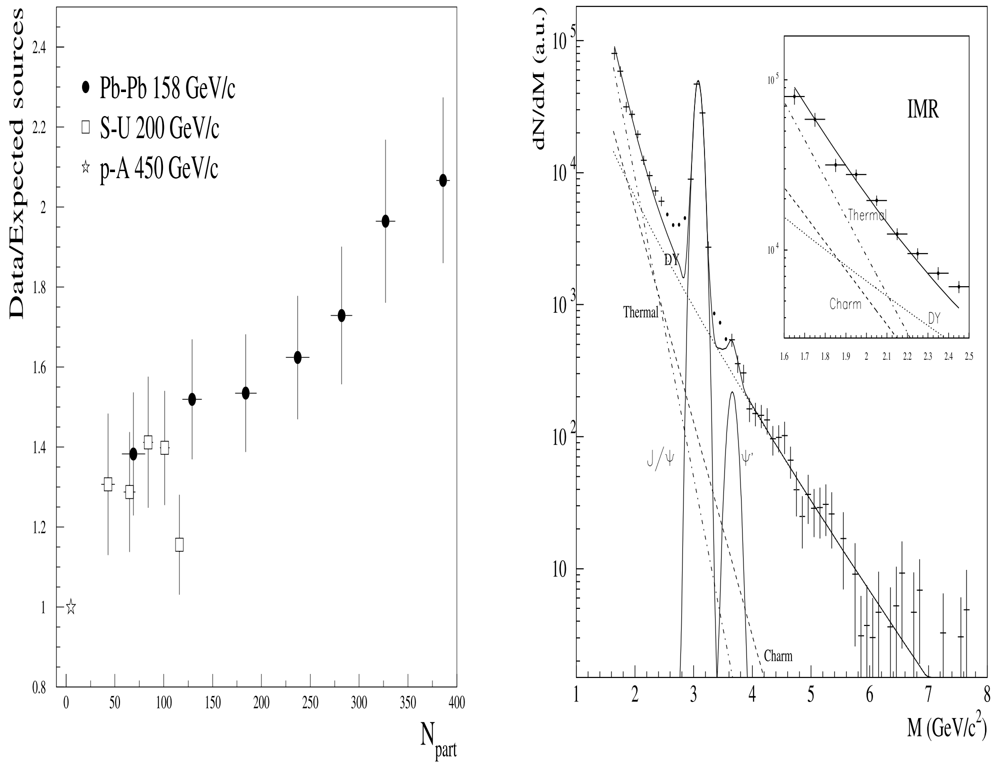

Figure 1.10: Dilepton enhancement from the NA50 experiment. [31, 24] In the left hand plot, the enhancement in the IMR of dimuon production for Pb-Pb and S-U collisions with increasing participants relative to p-A interactions is shown. In the right hand plot, the yields of $\mu^+ \ \mu^-$ are plotted as a function of $\mu^+ \ \mu^-$ effective mass. Expected Drell-Yan, D mesons are also plotted along with fits to an increased charm and thermal contributions from an expanding fireball scenario, the sum of which is shown as the solid black line, which gives the best fit to the experimental data.

1.16 Strangeness Enhancement

An enhancement in the yield of hyperons in Pb-Pb interactions with respect to normal hadronic interactions is considered a good indicator of plasma formation [9, 14, 29]. The colliding ions will consist of u and d quarks only so strange quarks and anti-quarks would have to be produced during the collision, see figure 1.11. The bare mass of the strange quarks is also of the same order of magnitude as the temperature of the QGP, in SPS Pb-Pb interactions, if chiral symmetry has been restored, see table 1.1. Hadronic interactions would not have time to affect the strangeness in a fireball via flavour changing reactions, as it will last for the order of 10^{-23} of a second, so a significant enhancement in strange particle production would have to take place with $s\bar{s}$ formation. With a partial restoration of chiral

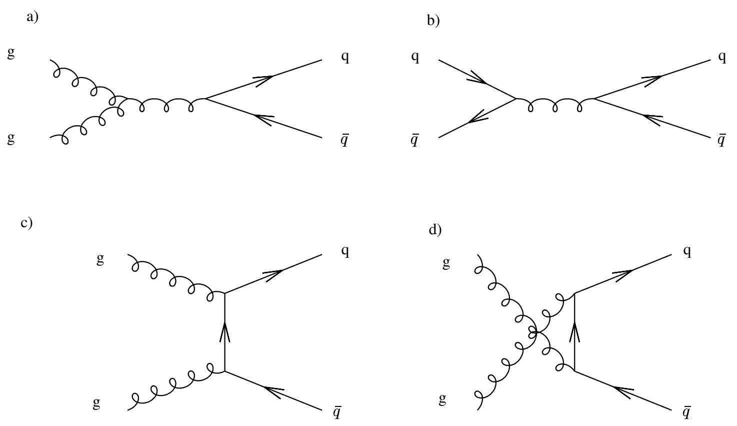

Figure 1.11: Possible strangeness channels.

symmetry it would only require an energy of around 300 MeV to produce $s\bar{s}$ pairs from $gg \longrightarrow s\bar{s}$. It has been shown that this is the dominant process in a QGP [9] at around a typical temperature of 200 MeV and for a thermalised QGP $s\bar{s}$ pairs should be readily produced.

There are three main effects that are expected to occur in a QGP which will favour strangeness production:

- Pauli blocking [14] where the production of $u\overline{u}$ and $d\overline{d}$ pairs are suppressed. Quarks are fermions and, in the finite volume of a plasma, only a finite number of a given flavour can occupy a given energy level, i.e for u and d there are isospin, spin and colour quantum numbers, or six degrees of freedom for the lowest energy level. At SPS energies the energy levels available for $u\overline{u}$ and $d\overline{d}$ production will rapidly fill up after the collision as there will already be a substantial number of valence quarks from the colliding ions in the fireball, see section 1.8.1. This will favour the production of $s\overline{s}$ pairs. However, this will not be true, at RHIC and the LHC energies.

- Production of $s\overline{s}$ pairs in a plasma, with the reduced mass of the strange quarks, will be energetically favourable to the production of strange baryons in a hadronic system. In a hadronic system, the lowest energy needed to produce a Λ in,

$$p + \pi \longrightarrow p + \Lambda + K^{+} \tag{1.11}$$

will be of the order of 570 MeV, and to produce $\overline{\Lambda}$

$$p + p \longrightarrow 2p + \Lambda + \overline{\Lambda}, \tag{1.12}$$

would require an energy of 2.23 GeV, this is approximately seven times the energy if chiral symmetry has not been restored and therefore much less likely to occur. Also, in hadronic reactions, it is energetically favourable to produce strange baryons, as opposed to anti-baryons, while in a plasma the production of anti-strange quarks occur with the production of strange quarks.

- The lifetime of the fireball will be about 3×10^{-23} second. If a QGP were to form it is believed that the reaction rate for the production of $s\overline{s}$ pairs would reach equilibrium or near equilibrium [9]. In a hadronic interaction the production rate would be ten to thirty times lower [34] and would be unlikely to have time to reach strangeness equilibrium during the lifetime of the fireball, further reducing the strangeness production.

Because the interaction rate is much slower in a hadronic system and the energy needed to produce the strange quarks much higher than in a QGP it is unlikely that an enhancement effect would be seen. The detection of a large enhancement in strangeness should be a positive signal that a QGP has formed. Furthermore, particles with a higher strangeness number would be expected to be enhanced more [9]. In particular, the antihyperons are particularly difficult to produce in hadronic reactions due to the energy requirements and their enhancement would act as a good indicator of QGP formation.

The experiment that will be the subject of this thesis, NA57 [35], detects strangeness enhancement via the following list of weak decay channels with only charged particles in the final state,

- A K^0 is 50% K_s^0 and 50% K_l^0. The K_s^0 is detected in NA57.
- $K_s^0 = \frac{1}{\sqrt{2}}(|K^0> + |\overline{K^0}>) \longrightarrow \frac{1}{\sqrt{2}}((\overline{d})s + d(\overline{s})) \longrightarrow \pi^+ + \pi^-$,
- $\Lambda = (uds) \longrightarrow p + \pi^-$,
- $\overline{\Lambda} \longrightarrow \overline{p} + \pi^+$,
- $\Xi^- = (dss) \longrightarrow \Lambda + \pi^-$,
- $\Omega^- = (sss) \longrightarrow \Lambda + K^-(\overline{u}s)$.

The enhancements for the families of particles that contain strange quarks at 160 GeV/c beam momentum from NA57 [35] are shown in figure 1.12. The first two bins show enhancements for particles with at least one quark in common with the colliding particles and the next two bins show particles with no quarks in common with the nucleon. The final bin shows the enhancement of the combined '$\Omega + \overline{\Omega}$' signal. The vertical axis gives the enhancement per nucleon compared to the p-Be interaction. p-Be data are taken as the interaction volume will be too small for a QGP to form and are used to normalise the Pb-Pb data. There are three things to note from this plot:

- The enhancement of the triply strange $\Omega^- + \bar{\Omega}+$ is up to a factor of twenty;
- The particles and the anti-particles both show significant enhancements;
- The enhancements have a hierarchy which increases with increasing strangeness content of the particle.

Together, these effects are a strong signal of plasma formation at 160 GeV/c. Similar data taken at 160 GeV/c per nucleon (160 A GeV/c) by the predecessor to NA57, WA97, was used as an announcement by CERN in February 2000 that a new state of matter had been discovered. The NA57 experiment at CERN examined strangeness enhancement at 160 GeV/c and the lower beam momentum of 40 GeV/c. The 40 GeV/c p-Be data taken with the NA57 experiment in 1999 will be used to normalise the Pb-Pb data and it is these p-Be data that are the topic of this thesis.

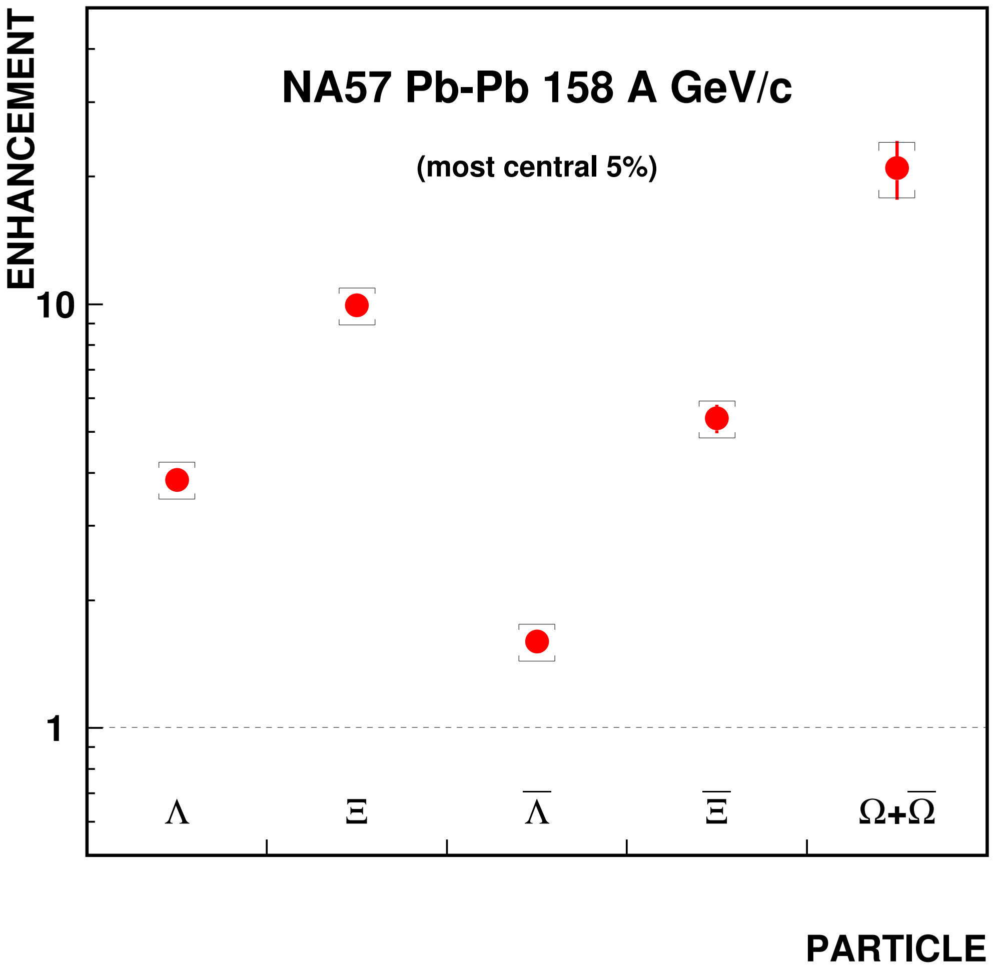

Figure 1.12: Enhancement of hyperons at 160 GeV/c per nucleon Pb-Pb interactions (points) for different hyperon species. Data normalised to 160 GeV/c p-Be interactions, (bottom line) where QGP would not be expected to form. NA57, 160 GeV/c per nucleon.

Chapter 2

The NA57 Experiment

The NA57 experiment [35] was the successor to the WA97 experiment [36] and extended the measurements in centrality and energy range. NA57 measures strangeness enhancements in Pb-Pb interactions at 160 A GeV/c, the same as WA97, and a lower beam energy of 40 A GeV/c. The lower beam energy will supplement the WA97 data and both beam energies will extend the measured centrality of collision data for Pb-Pb interactions to a lower limit of 50 wounded nuclei per interaction. It uses a Beryllium target as a control at the same energies which is equivalent to an interaction where a QGP would not be expected to form [35].

2.1 The Super Proton Synchrotron, SPS

The NA57 experiments were conducted at the SPS accelerator located at CERN. The SPS can accelerate protons to 450 GeV/c and lead ions up to 160 GeV/c per nucleon, (160 A GeV/c), for use in fixed target experiments. In the future it will be used as the proton and lead ion injector into the LHC, see figure 2.1.

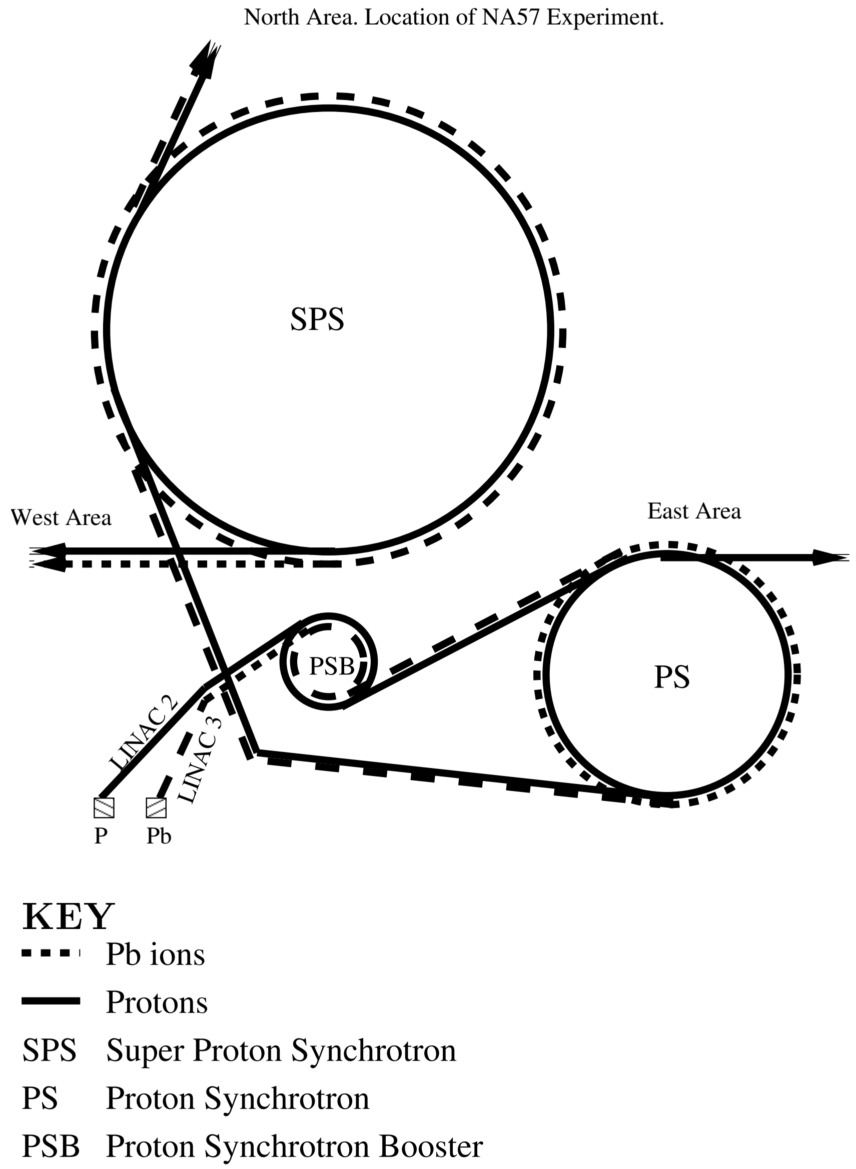

Figure 2.1: Layout of the SPS.

The ions are accelerated in stages before they reach the final SPS ring. Protons are initially accelerated by a linear accelerator, Linac 2 and partially stripped lead ions, $^{208}Pb^{25+}$, by Linac 3. The acceleration of lead ions is more complex than that for protons. Table 2.1 lists the injection and extraction energies of each section [37]. Each acceleration of the particles is performed by a number of RF cavities along the

Table 2.1: Injection Energies and Timings

Injection PSB		
Parameter	Partial stripped $^{208}Pb^{53+}$ ions	p
Momentum	4.2 A (per nucleon) MeV/c	50 MeV/c
Time	288ms	415ms
Injection PS		
Momentum	95.4 A MeV/c	1.0 GeV/c
Final Stripper Injection SPS PS, 90%-100% stripped Pb ions		
Momentum	4.25 A GeV/c	19.07 GeV/c
Time	0.5s	0.5s
Extraction SPS PS, 100% stripped		
Momentum	160 A GeV/c (400 GeV/c total)	400 GeV/c

rings of the PS, PSB, SPS, and the linear accelerators. The acceleration is provided within the cavities by a potential difference, which is not constant but pulsed. The beam has to be at the correct position within the cavity to be accelerated and the particles are accelerated in groups called ‘bunches’. In the circular accelerators, the SPS, the PSB and PS there are a number of bending magnets and focusing magnets along the circumference to keep the bunches within the beam pipe. Numerous effects can cause the bunches to become de-focused, two of which are gases within the beamline, a particular problem with the acceleration of lead ions owing to their large interaction cross section, and the bending magnets, due to the gradient of the bending field and the finite width of the bunch.

The bunch is refocused using quadrupole magnets. As the bunch passes through a quadrupole it will be focused along one axis and de-focused along the other. A single quadrupole on its own will not focus a beam but a second quadrupole with the field rotated by 90^0 located near it, in an arrangement called a 'Doublet', can give an overall net focusing of the bunch. In reality a number of doublets are used for optimal focusing.

The focal point of this arrangement of quadrupole magnets will depend on the momentum of the particles within the bunch. There will always be a small spread in the momentum of the particles in the bunch which will cause it to become de-focused as it passes through the doublet in a way that can be likened to chromatic aberration in optics. A sextupole magnet is added to the doublets to correct for this.

To keep the lead beam from dispersing at lower momenta as it travels round the PSB the vacuum has to be kept at an order of magnitude lower than needed for protons. Maintaining a vacuum at these levels was a challenging task for the design and running of the lead ion facility [38].

The lead ions do not enter Linac 3 fully stripped of their ions. This is due in part to the ion production; and to avoid a further upgrade of the vacuum system. The lead ions are stripped in two stages. Stripping cannot be done inside the circular accelerators and is done at the injection stages. The first stripper is at the end of the Linac 3. This is a basically a metal foil which yields Pb^{+53} from the Pb^{+25} ions that are accelerated through the Linac. The next stripper is placed between the PS and the SPS. As the SPS also worked as an injector for LEP the stripper had to be moved in and out of the beam on a pulse by pulse basis. This final stripper was in the range of 90%-100% efficient for stripping the Pb^{+53} ions.

The heavy ion facility is capable of producing lead ions at 160 GeV/c and a lower beam energy of 40 GeV/c by re-tuning the acceleration sequence. However, it is not efficient to produce protons at 160 GeV/c and 40 GeV/c. This was achieved by colliding maximum beam energy protons from the SPS with a lead target and then using a dipole magnet and collimator to separate and select the required beam momenta.

2.2 The NA57 Experiment

The experiment consists of the following key parts,

- A lead target or beryllium target and a lead or proton beam.
- A number of scintillators connected to a trigger.
- The Goliath Magnet which bends charged particles for momentum measurement.
- A telescope consisting of 13 silicon pixel arrays to detect the charged decay products and telescope microstrips.
- A number of Multiplicity Strip Detectors (MSD), used to record information on particle momentum and the centrality of a collision.
- A trigger and data acquisition system which decides when an event of interest is to be recorded.

Figure 2.2 shows a diagram of the 1999 experimental setup,

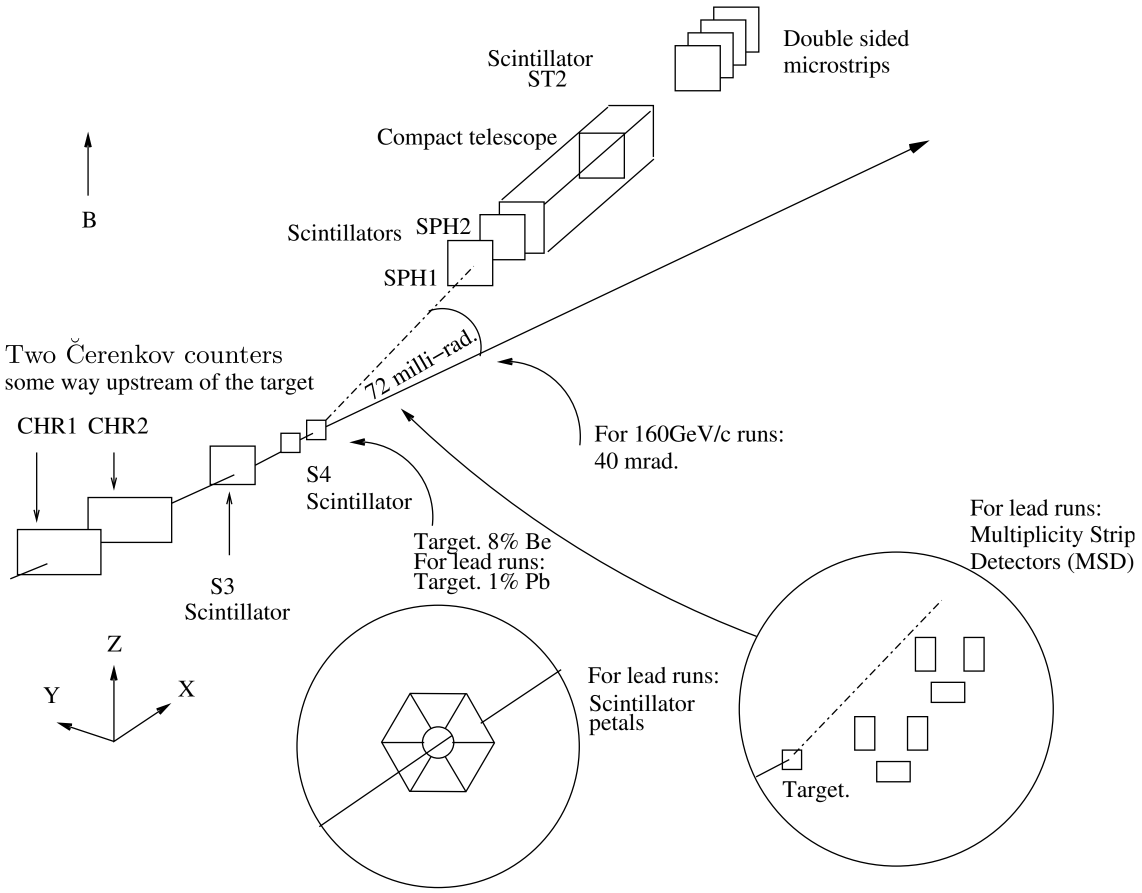

Figure 2.2: Layout of the 1999 NA57 experiment.

2.3 The Target

The targets have to be thick enough to get a reasonable interaction rate but thin enough to keep multiple interactions in the target to a minimum. For Pb-Pb interactions the target was 1% of an interaction length; this is around 400μm thick. For p-Be interactions, the beryllium target is much thicker. At 8% of an interaction length, this is 3.26 cm thick.

2.4 The Goliath Magnet

The telescope and other detectors were mounted on a bench, that is not in vacuum and was placed in the Goliath magnet, see figure 2.3. The beam line is terminated with a thin window that will seal the vacuum but allow the ions to pass through and reach the target. Inside the magnet, the X axis is the beam direction and the Z axis is the field direction in the vertical plane of the magnet. In this case, the magnetic field will cause the charged particles to follow a curved path in the horizontal X-Y plane. This plane is called the 'bend plane'.

Goliath is a warm magnet operating at around 3000 A and producing a field of around 1.4T with a smaller compensating magnet added, called David, running at around half the current. Data is taken with Goliath in both polarities to cancel possible irregularities in the field distribution.

2.5 The Telescope

The charged decay tracks are detected by a telescope made of 13 silicon pixel detector planes with a total of about 1.1 x 10^6 pixels. Seven planes use the Omega2 chips with a pixel size of 75 x 500μm^2 and six planes use the newer Omega3 chips

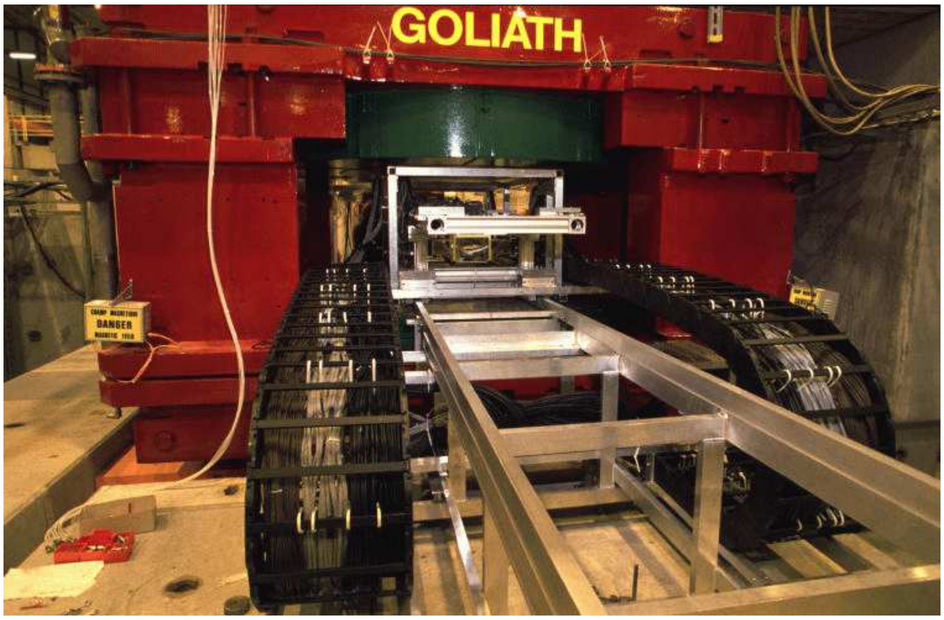

Figure 2.3: Goliath magnet with bench removed.

with pixel size of 50 x 500μm^2. The planes are 5cm square and are arranged in a telescope that is 30cm long [35]. This telescope is placed in such a way that it views the central rapidity region of a collision, see appendix A. For the laboratory frame the rapidity is $y_{lab} \cong 2.9$ for p-Pb and $\cong 2.2$ for p-nucleus. The rapidity is viewed over a region of $\pm y_{com} = 0.5$, see figure 2.4. In the CM frame of a collision the telescope would be placed perpendicular to the collision axis. However, NA57 is a fixed target experiment and the longitudinal component of momentum will be Lorentz boosted forward in the laboratory frame, see appendix B. For the p-Be runs, the telescope is placed at an angle of 72 mrad to the beam axis to view the central region. The Lorentz boost has the advantage that the lifetime of particles is greater when viewed in the lab frame thus giving longer decay tracks and a better primary vertex position for the decay. For the 1999 data-taking, only the first ten planes of the telescope were used to take data, see figure 2.5.

In order to detect the weak decay of the strange family of particles in NA57 the telescope is placed at a distance of 40cm-60cm (p-nucleus,Pb-Pb) from the target. However, if we wanted to look at the shorter lived charm family of particles, the telescope would have to be placed within a few centimetres of the target. This is the aim of the NA60 experiment [32, 33].

In the bend plane, high momentum particles would have a large radius of curvature and pass through the telescope approximating straight lines and giving low momentum resolution. To aid in resolving these high momentum events a set of silicon microstrips was placed further downstream of the telescope so as to give a larger lever arm.

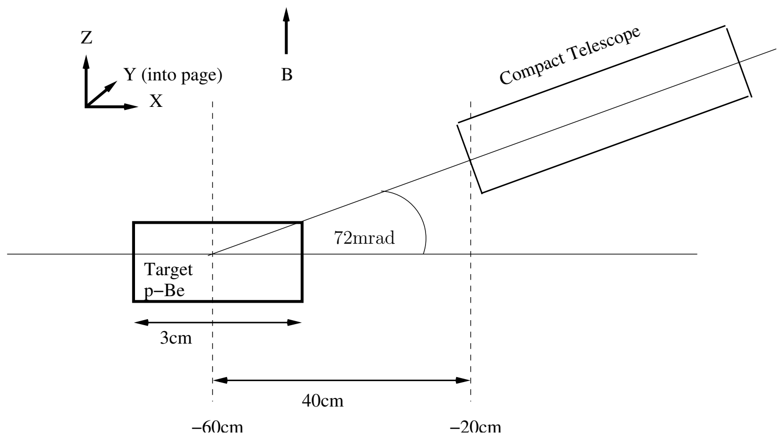

Figure 2.4: Diagram of telescope setup.

2.6 The p-Be Trigger System

The trigger monitors signals from the scintillators and two Čerenkov counters, some 100m upstream of the target, to make a decision on whether a good event has occurred, figure 2.2. There are two triggers, an older NIM system and a modern VME system. The VME trigger is a sophisticated microcomputer trigger designed by

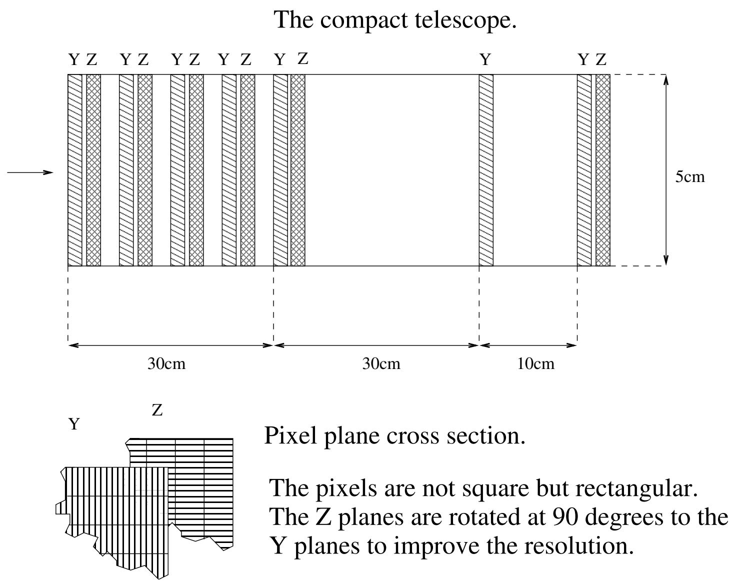

Figure 2.5: Diagram of telescope pixel planes.

Birmingham University and the NIM trigger is made up of logical units that are wired together in crates. Initially, the NIM was used as the main trigger while the new VME trigger's performance was assessed in a series of tests. The trials were a success and the trigger was upgraded to the VME for data-taking during the rest run, with the NIM used as a backup in case the VME needed to be taken offline for further performance testing.

The Signals from the scintillators and Čerenkovs were monitored by the trigger system and when all the trigger conditions were met, data from the telescope and the silicon microstrips were read out and recorded by the Data Acquisition System [39].

2.6.1 p-Be Proton Identification

The beam from the SPS is not constant. It is pulsed for 2.3 seconds every 14 seconds with about 10^7 particles per spill. Only about $\frac{1}{8}$ of these particles will be protons, the rest will mainly be pions. The two Čerenkov counters, some 100m upstream of the target, are used to identify proton interactions. The second Čerenkov is identical to the first and is there to confirm the signal. The Čerenkov gas pressure is set such that pions and kaons passing through it will give a signal in the counter and that protons will not. The NOT signal in both detectors is taken as a signal of protons. The S3, and S4 scintillators detect any particles that passed through the target, figure 2.2. S3 lies outside Goliath and S4 inside. The S4 detector is smaller, 8mm×8mm, and closer to the target, so will indicate the number of 'on' target particles where the S3 detector can be used to give information on the beam intensity. This trigger condition is written,

$$(\overline{\text{Čerenkov1}}.\overline{\text{Čerenkov2}}).\text{S3}.\text{S4} = \text{proton beam} \tag{2.1}$$

Where the '.' means a logical 'AND' and the bar a logical 'NOT'.

2.6.2 Telescope Trigger.

The trigger monitors charged particles that have passed through the SPH1 and SPH2 scintillators in front of the telescope and the ST2 scintillator at the rear of the telescope, figure 2.2. The signal from either SPH1 or SPH2 will be larger if more than one track passes through them into the telescope. Each signal on its own has a large Landau tail, but the signals from both detectors can be compared to confirm the number of tracks. A selection can be made so that at least one charged track or at least two charged tracks pass through the telescope. One charged track triggers are needed to get Λ cross section rates to normalise the data and two charged tracks are used for normal data-taking.

The final trigger condition for a p-nucleus event is written,

$$(\overline{\text{Čerenkov1}}.\overline{\text{Čerenkov2}}).\text{S3}.\text{S4}.(\text{N}_{\text{tracks}}(\text{SPH1}).\text{N}_{\text{tracks}}(\text{SPH2})).\text{ST2} = \text{Event}. \tag{2.2}$$

2.6.3 Pb-Pb Centrality Trigger

Although not used in the p-nucleus data-taking, Pb-Pb runs require the 'Centrality' of an interaction, i.e. the number of nucleons that take part in the interaction, to be triggered on. The multiplicity of charged tracks in the hexagonal array of six scintillator 'petals', placed 10 cm upstream of the target, shown in figure 2.2, is used by the trigger to decide if the interaction was central enough to be recorded. This is triggered if a high multiplicity is recorded in five out of the six petals. For events with centralities of interest a set of silicon microstrip detectors downstream of the target is used to sample the charged particle distribution.

Offline, the number of wounded nuclei in the collision are calculated from the charged particle multiplicity. This is done by fitting a corrected multiplicity distribution to the Glauber model [40]. This allowed centrally triggered events down to fifty wounded nuclei per interaction to be recorded by the NA57 experiment [26].

2.7 The 2001 p-Be Run

The 2001 experimental setup for p-Be at 40 A GeV/c is essentially the same as the 1999 40 A GeV/c setup and the 2001 run complements the 1999 data and increases the statistics. This increase in statistics is useful in reducing anti-lambda background signal which is fairly high with the 1999 data alone.

2.8 WA97 and NA57's Motivation

The following fixed target experiments, performed at CERN, contributed to the study of strangeness production as a probe for the QGP. WA (West Area at the SPS) experiments were performed at the Omega Spectrometer, a 1.8 T superconducting magnet. NA (North Area at the SPS) experiment, NA57 used the 1.4T Goliath magnet. NA35 and NA49 used a 1.5 T field and NA36 used a 2.7 T field;

- NA35 [41, 42]: (p,O,S)-(S,Pb) at 60 and 200 GeV/c per nucleon
- NA36 [43, 44]: (S,Pb)-(Au,Fe,Cu,S,Pb) at 60 and 200 GeV/c per nucleon
- WA85 [45]: S-W and p-W collisions at 200 GeV/c per nucleon
- WA94 [46]: S-S and p-S collisions at 200 GeV/c per nucleon
- WA97 [36]: Pb-Pb, p-Pb and p-Be collisions at 160 GeV/c per nucleon
- NA49 [16, 47]: Pb-Pb, collisions at 160 GeV/c per nucleon.
- NA57 [35]: Pb-Pb, p-Pb and p-Be collisions at 160 GeV/c and 40 GeV/c per nucleon.

WA85 and WA94 have shown an enhancement of Ξ and Λ going from proton-nucleus to nucleus-nucleus collisions of a factor of three [29]. WA97 compared the spectra of hyperons and antihyperons from Pb-Pb collisions, where a QGP would be expected to form, with that from proton induced reactions, used as a control, and covered central rapidity down to around 100 wounded nucleons and transverse momenta of a few hundred MeV.

An enhancement of strangeness was found at WA97 in the Pb-Pb collisions, as described in section 1.16. There was an enhancement for Ξ of a factor of five going from p-nucleus to Pb-Pb and an enhancement greater than an order of magnitude for Ωs. In February 2000, this was one of the major pieces of evidence backing an announcement by CERN that a new state of matter had been created. The NA57 experiment has taken further data for this enhancement at 160 GeV/c, see figure 1.12.

NA35 and NA36 were the predecessors of NA49. NA49 [16, 47] is a large acceptance tracking spectrometer that is capable of measuring 70% of the common hadronic signals from an interaction on an event-by-event basis. One of its recent results from kaon to pion ratios seems to show that the phase transition to a QGP may not be of first order but this is still undergoing vigorous theoretical discussion [16].

NA57 has a narrower acceptance and increased resolution over NA49 and uses a silicon pixel telescope to study hyperons coming from the central region with higher statistics. This design allows NA57 to look for the onset of plasma formation through the enhancement of strangeness. NA57 refines the results of WA97 in two ways;

- It increases the centrality range over that of WA97. WA97 took data with a centrality down to around 100 wounded nuclei in a Pb-Pb collision, NA57 extended that lower limit down to around 50 wounded nuclei.
- WA97 took data at a beam energy of 160 GeV/c per nucleon (160 A GeV/c) and NA57 took data at both 160 A GeV/c and 40 A GeV/c [35].

2.8.1 The Proton Beam Runs

In the WA97 and NA57 fixed target experiments, p-Pb and p-Be collisions were used as control data to simulate proton-nucleon collisions where no plasma would be expected to form. The yields in Pb-Pb interactions and the number of participants in the collision can then be normalised to the p-Pb data. As a QGP would not form in the control data any enhancement of the Pb-Pb data relative to this control would indicate increasing strangesess production. A problem with this assumption comes from the Pb nucleus having a large number of nucleons. This suggest that p-Pb control data may have multiple wounded nucleons which would bias the normalisation. Also, the effect of the decay products passing through the large volume of the Pb nucleus should also be considered.

It would seem that the ideal way to simulate proton-nucleon collisions in a fixed target experiment would be to use liquid deuterium, with a proton and neutron, as the target but apart from the problems of using this material, the interaction length is too large and the interaction rate within the area covered by the detector would be too low to be of use.

A Beryllium target is solid at room temperature, making it much less of an issue to handle, and it is also some 26 times as dense as liquid hydrogen, [30], increasing the interaction rate. The nucleus of beryllium has four protons and natural beryllium has equal numbers of protons and neutrons. The beryllium nucleus is much smaller than the lead nucleus which eliminates the possibility of secondary nuclear interactions and the beryllium nucleus is isospin symmetric, unlike the lead nucleus. The enhancements of Pb-Pb interactions normalised to p-Be and p-Pb data were the same, [48]. The equality between the p-Be and p-Pb yield data show that, at the SPS beam momenta, secondary wounded nucleons or the larger interaction volume in the Pb nucleus are not an issue for the normalisation of the enhancements. It can be concluded that the large enhancemet seen in strangeness production are genuine and are not due to some unaccounted-for nuclear effect from the normalisation to p-Pb or p-Be.

2.8.2 Data Collected at the NA57 Experiment

Table 2.2 shows the data collected by the NA57 experiment [35] for various interactions and years. For NA57 160 A GeV/c proton reference data from WA97 p-Be (180 M events) and p-Pb (290 M events) have been used.

Table 2.2: Data collected by NA57. For NA57 160 GeV/c proton reference data, the proton reference data from WA97 at 160 GeV/c p-Be (180 M events) and p-Pb (290 M events) has been used

System	Beam momentum	Sample size	Collected
Pb-Pb	160 A GeV/c	230 M events	November 1998
p-Be	40 GeV/c	60 M events	July 1999
Pb-Pb	40 A GeV/c	290 M events	November 1999
Pb-Pb	160 A GeV/c	230 M events	October 2000
p-Be	40 GeV/c	110 M events	September 2001

Chapter 3

Particle Reconstruction

If an interaction satisfies the trigger conditions the hits on the pixel planes in the compact telescope will be read out. For the Pb-Pb runs, multiplicity information from the microstrip detectors will be read out as well. This defines an 'Event' record and is written onto a mass storage medium for further off-line analysis. This data intensive process is managed by dividing the data into roughly half hour data-taking blocks, referred to as 'Runs'. The paths of the charged decay tracks are reconstructed off-line with a three dimensional fitting program called ORHION. An example of the reconstruction is shown in figure 3.1.

During data-taking there a two common trigger conditions set by the SPH1 and SPH2 scintillators at the front of the telescope, see figure 2.2. These scintillators give a signal proportional to the number of charged tracks passing through them. Two minimum threshold levels are used for the trigger condition, one track and two tracks. A number of runs used a one track trigger for normalisation of the final sample. The two track trigger was used for normal data-taking as the signals of interest will decay into two or more charged tracks in the telescope.

Once ORHION has reconstructed the events, the candidate signals of interest are separated from the sample and further selections are chosen to reduce the background. Selections on the geometry of the experiment and the kinematics of the decay are chosen as these will not distort the signal distribution but uniformly reduce the background distribution with respect to the signal of interest.

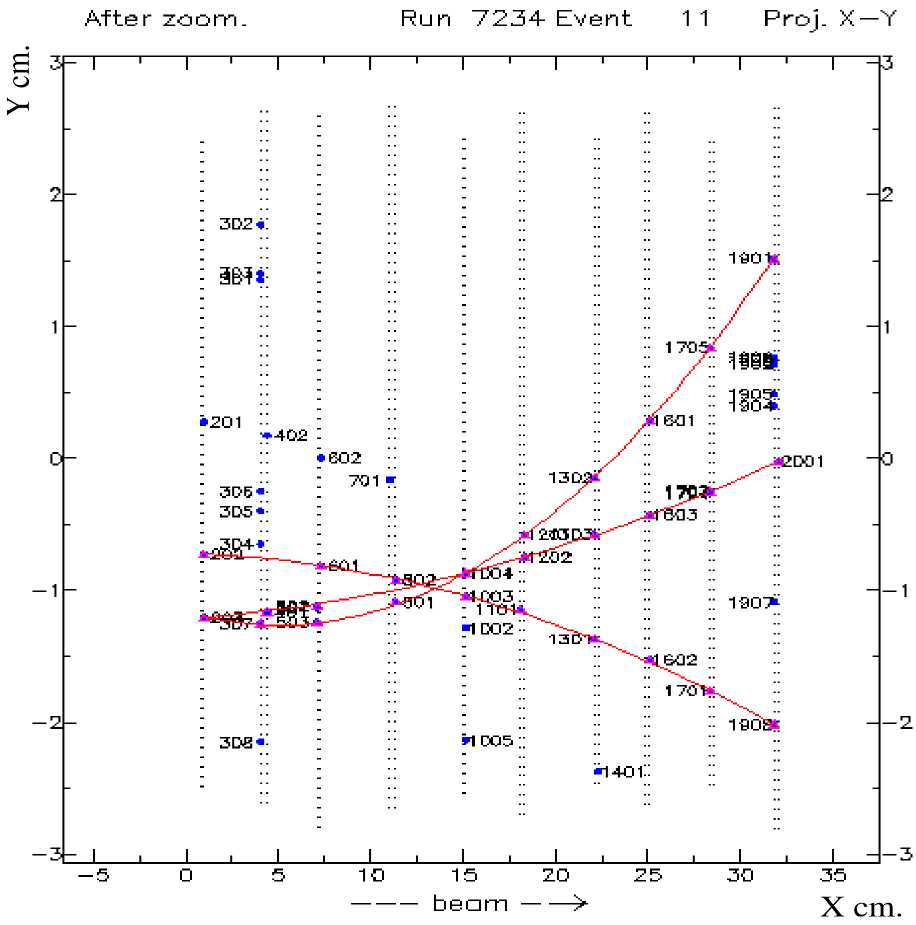

Figure 3.1: Reconstructed tracks from the pixel planes for one event

3.1 Sailor and Cowboy Decays.

Decays in NA57 take place inside a magnetic field. Two oppositely charged particles that originate from the same point will have either a 'cowboy' and 'sailor' type topology in the bend plane of the magnetic depending, randomly, on the angle of the decay plane with respect to the line of flight of the parent particle. If the transverse momenta of the charged decay tracks, at the decay position, point in the direction of the force the charged tracks experience from the magnetic field, the tracks will be swept away from each other and never cross. This gives a sailor topology. If the charges are swapped the transverse momenta will point in the opposite direction, at the decay position, to the force from the field. In this case they will bend away and then, later on, toward each other, giving a cowboy topology, see figure 3.2.

The V^0 mode is when either the cowboy or sailor decay points back to the target, the Cascade mode consists of a cowboy or sailor that point to a decay vertex, along with a secondary charged particle. The weakly decaying strange particles detected by NA57, Λ, K_s^0 decay in the 'V^0' mode and Σ, Ω in the Cascade mode. The detection of the cowboy topology is favoured as its twin crossing of two charged tracks will have better acceptance in the telescope.

The location and length of the NA57 compact telescope, see figure 2.4, accepts the cowboy topology, which will have the second crossing point within the active volume of the telescope, but will have poor acceptance for the sailor decays which have separated by the time they reach it. The off-line analysis program ORHION reconstructs cowboy V^0 decays in two stages. First the track momenta, positions and charges are reconstructed from the hits on the pixel plane and field direction information. Next, using an iterative procedure, oppositely charged tracks are compared to find the pairs that have the two crossing vertices needed to select a cowboy type topology.

The V^0 decays are separated into regions of Λ, $\overline{\Lambda}$ and K_s^0 decays using the Podolanski-Armenteros plot, see appendix C. To find the reconstructed mass of the parent particle from the momentum and charge of the decay tracks in one of these regions, the published mass of pions or protons are used [30]. Equation (3.6), on page 77, shows an example of this for the reconstructed mass of the K_s^0.

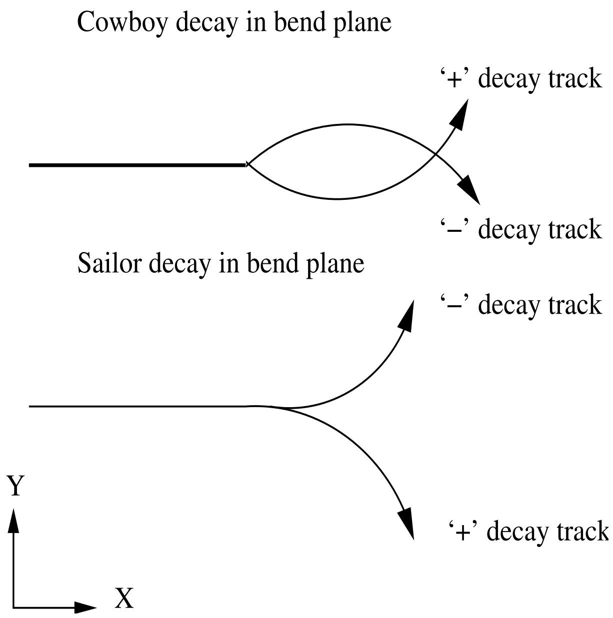

Figure 3.2: A cowboy and a sailor decay

3.2 Investigation of the Beam

For the Pb-Pb interactions the high number of tracks per trigger and the thin target allow the primary vertex to be reconstructed accurately on an event by event basis from the multiplicity in the telescope. This was unsatisfactory with the 40 GeV/c p-Be interactions due to the low track multiplicity in the telescope. In these interactions the source of the decays can be distributed anywhere along a target which is 3.26 cm thick. The low charged particle multiplicity with p-Be interactions then makes it impossible to locate the primary vertex on an event by event basis using this method.

The starting point for obtaining information from the beam involved averaging the interactions over whole runs. There were 160 runs numbered 7005-7309 and at run 7200 the field polarity was changed. To investigate the beam, the V^0s line of flight were traced in the bend plane, XY, to a point located at Z = -17.85 cm, see section 3.2.2 for details about adjustments made to this Z position. The Y position was averaged for each run and projected vs. run number, see figure 3.3. The beam was seen to be unstable before run number 7100, which tallied with notes in the experimental logbook [49] concerning beam stability during these runs. In conclusion, these runs were excluded from further analysis. The effect of changing the magnetic field was found to shift the Y vertex from 0 to -.1 cm. Next, Y was fixed and Z was averaged which showed there was no shift in Z with field change, which is as expected as this is not the bend plane.

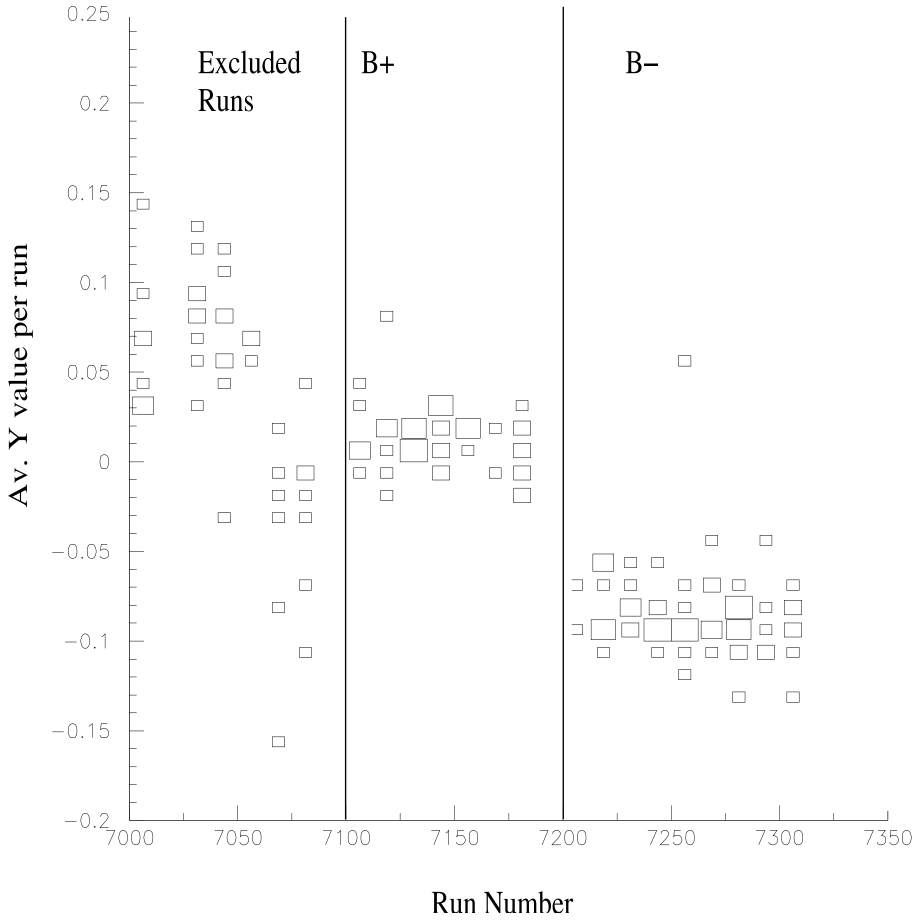

Figure 3.3: Y projection average per run

3.2.1 Primary Vertex and Beam Location

In three dimensions, the intercept of the $V^0 s$ line of flight with the beam along X can be found by projecting the V^0 line of flight onto the fixed planes XY or XZ. Figure 3.4 shows how the X axis can be located using these methods. In case 1, in the XY plane, the V^0 line of flight intercept with the Y axis, fixed at 0.0 cm and then -0.1 cm for the change in magnetic field polarity, $B^{\pm}$, gives the location of the X axis, see figure 3.5. In this plane the telescope, and hence the $V^0 s$ line of flight will almost be parallel to the X axis of the beam. The error in the intercept position will become very large as these lines become parallel, giving very poor resolution. The fit for the vertex is improved in case 2, the XZ plane. The intercept of the V^0

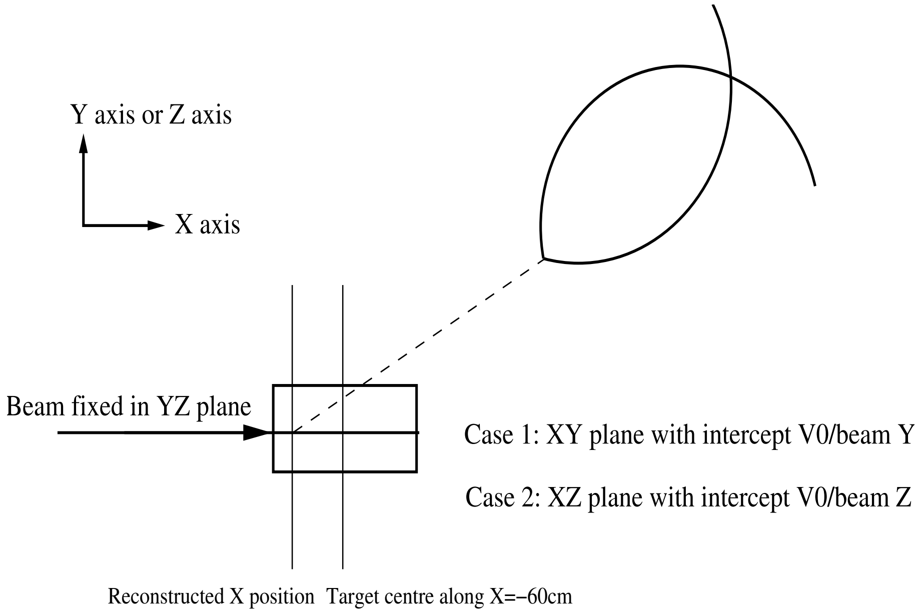

Figure 3.4: Calculation of the X intercept of the V0

line of flight with the Z axis was fixed at -17.5 cm. In this plane the telescope is at 72 mrads to the beam and the $V^0 s$ line of flight is non-parallel to the X axis. The primary vertex resolution along the X axis was greatly improved in this plane but gave the target centre at -61.5 cm in X, 1.5 cm different from the survey value of 60 cm recorded in the logbook. This value is the distance to the target centre and was measured very accurately during the setup of the experiment [49]. However, the nominal beam position is not as accurate, as it is taken to be the centre of the beamline, surveyed for the Z axis at -17.5 cm from the experimental logbook [49]. It was found that the peak of the primary vertex distribution was strongly correlated with the location of the Z axis, see section 3.2.2 and the cause of the 1.5 cm difference. The optimal value of Z was found to be -17.85 cm which gave the target centre in X as -60.0 cm as required.

The plot in figure 3.6 shows the V^0 line of flight traced to the plane XY located at Z=-17.85 cm. The peak is now located at -60.0 cm along the X axis as expected. From this a selection was made on the maximum spread of the beam along the Y axis of 2 cm and an upper limit along the X axis of -50 cm.

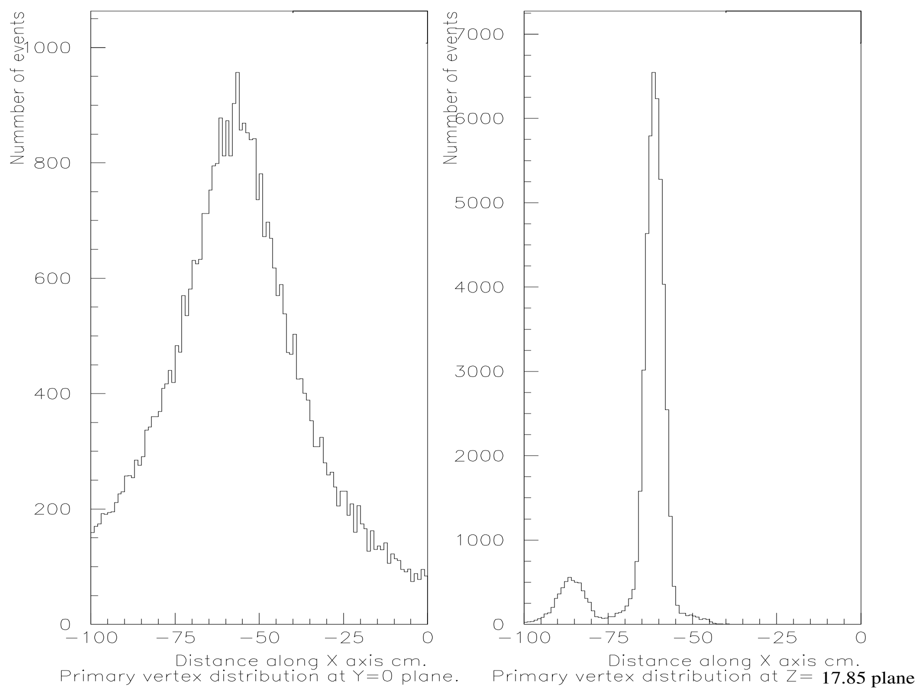

Figure 3.5: Primary vertex location for V^0 intercept in the XZ and XY plane

It was noticed that in figure 3.5 there is a peak at -86 cm just behind the target distribution. From the logbook of the 1999 experiment [49] this second peak is located at the position of the S4 scintillator. To remove interactions with the S4 counter this secondary peak was removed with a selection at -67.5 cm along X, a selection was also made at -52.5 cm as this is outside the target region.

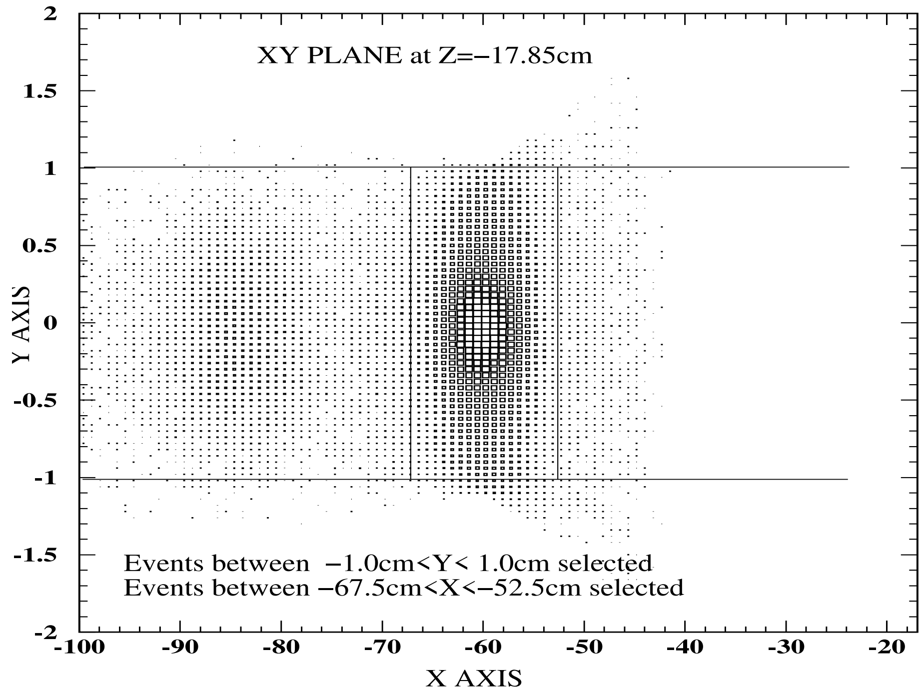

Figure 3.6: XY projection of V^0, Z=-17.85

3.2.2 Location of S4

The centre of the target in X can be measured as a distance from the beampipe and was found to be -60 cm $\pm$0.1 cm in X. The nominal position of the beam in the YZ plane is taken as the centre of the beam pipe. Z is then centred on S4 at the start of the data-taking. A value for the nominal beam centre was given in the logbook [49] as -17.5 cm in Z and 0.0 cm in Y. Using this position for the Z axis gives a peak for the X axis at -61.5 cm. Further investigation in the logbook showed that the measured position of the S4 counter centre was found to be 4 mm lower than the nominal beam value in Z, if measured from the base of the Goliath Magnet, this would make the location of the beam in Z -17.9 cm. This location assumes that the beam will not drift over the whole data-taking and gives no information about the location of the beam along the Y axis, which being in the bend plane, is likely to be affected as the field changes.

To investigate this with real data the location of the Z axis was moved until the peak of the X axis intercept was located at -60 cm using the intercept method of case 2 in section 3.2.1. The correlation between the X axis peak and the location of the Z axis is very sensitive. In equation (3.4) the unknown 'Constant' from the previous equations has been eliminated to give an expression for the target intercept along the X axis, x'. From equation (3.5), using a beam-telescope angle of 72 mrads, the shift of the target intercept $\delta x'$ is an order of magnitude greater than the corresponding shift in δz.

$$\begin{aligned}
\tan\theta_{V^0.Beam} &= \theta_{V^0.Beam} \text{ for small theta} && (3.1)\\
z_{(V^0\ decay)} &= \theta_{V^0.Beam}\ x_{(V^0\ decay)} + Constant && (3.2)\\
z'_{(V^0\ intercept\ with\ beam)} &= \theta_{V^0.Beam}\ x'_{(V^0\ intercept\ with\ beam)} + Constant && (3.3)\\
x - \frac{(z-z')}{\theta} &= x' && (3.4)\\
\delta x' &= \frac{-1}{\theta}\delta && (3.5)
\end{aligned}$$

Investigating this with the real data indeed showed that a change in Z of about 0.1 cm gave a change in X of about 1.0 cm. The target centre was located at -60.0 cm when the Z axis was located at -17.85 cm. This value is within the errors of the measured value of Z = -17.90 cm for the S4 counter centre found from the logbook [49]. The Z measurement of -17.85 cm is quite accurate using the intercept method and with the information from the 'Target' V^0s discussed in section 3.3, the error can be put at around ± 0.01 cm. This difference between the measured centre of S4 and the beam at -17.5 cm was quite large. It can be accounted for from the previous results on beam drift at the start of the run. During this period the beam would have been focused on S4 at the start of the data-taking but it has been shown that the first 100 runs showed excessive drift and were excluded. This drift could be the cause of the defocussing and for further analysis the beam was adjusted to -17.85 cm in Z. Another consideration from this defocussing is the beam spread. The beam spread in Z was found to be larger than the dimensions of S4, see figure 3.10 and the tails of this distribution lie outside the 4×4 mm area of the S4 counter. This would chop the beam profile and this effect needed to be replicated with the beam simulation in the Monte Carlo, used to correct the physics results via the weighting chain, discussed in Chapter 4.

3.3 Target V^0s

The beam width and the location of the beam in Y and Z were investigated using the method of target V^0s. Normally, the V^0 decay vertex for a signal of interest would be selected to lie some way from the target to reduce the background of charged tracks from normal hadronic decays that would be mis-constructed as a V^0. This is done by excluding decays within 15 cm of the target centre, see upper figure 3.7. However, if the V^0s within the target region are selected, the fact that a majority of these have been constructed from background tracks can be used to locate the beam in the YZ plane. These V^0 are named 'target V^0', see lower figure 3.7. The target V^0s will be constructed from charged particles of opposite charge, mainly pions within this target region. As most of these tracks do not come from strange particle decays, the Podolanski-Armenteros Plot used to select signals of interest in the final analysis can now be used to select the background target V^0s, see appendix C. If the target V^0s data contained a high proportion of V^0 that were real signal, the Armenteros Plot would show this as curved bands. Figure 3.8 shows the Armenteros plot of the target region, -58.4 cm to 61.6 cm, using the raw data from the 1999 background tapes. See appendix C for a description of the Q_t and α variables. The uniform distribution of V^0s shows that there is no obvious signal and most decays will be the target V^0 background.

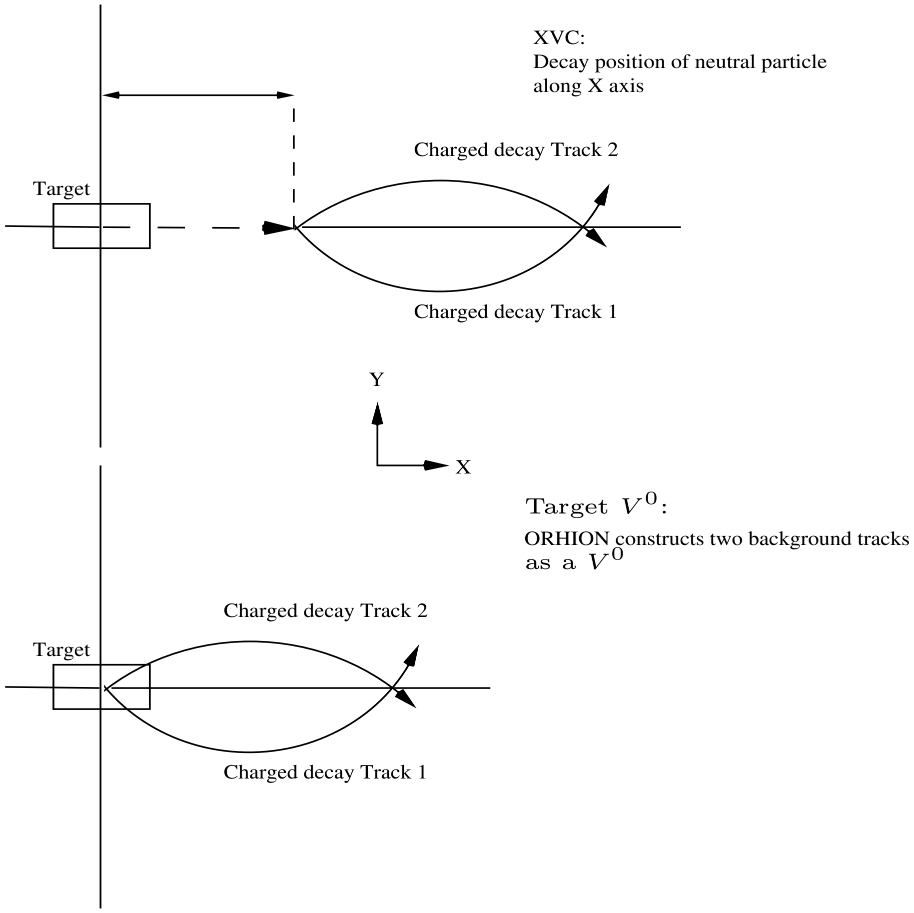

Figure 3.7: Real V^0 decay vertex and target V^0 vertex

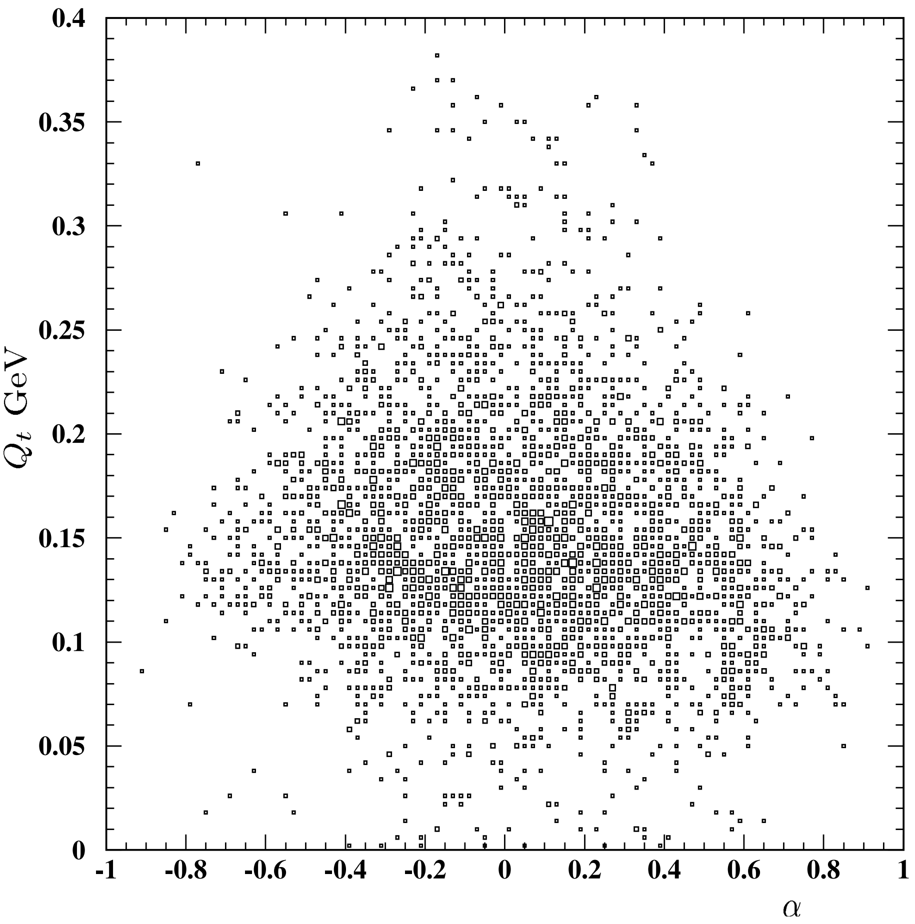

Figure 3.8: Armenteros plot of the target V^0 candidates

To be certain that there is no contamination from strange particle decays, the mass bands for the particles of interest, the Λ, $\bar{\Lambda}$ and K_s^0 were removed. For the K^0, a shifted mass was used to centre this selection on 504 MeV with width 6 MeV, see section 3.9 for an explanation of this shift. For the Λ and $\overline{\Lambda}$ the mass cuts were located at 1.12 GeV with a width of 4 MeV, see table 3.1.

The remaining target V^0s were then used to reconstruct the primary vertex information. The primary crossing vertex, being made of two background tracks, represents the interaction of the beam with the target. The plots in figure 3.9 show the field up and field down primary vertex along the Y axis. Figure 3.10 shows the primary vertex reconstructed by the target V^0s along the Z axis. This was found to be unaffected by the change in field direction as it is not in the bend plane of the magnetic filed. The plot shows the Z axis data taken over the field up and field down data. With Gaussian fits, the location of the beam in Z was found to be -17.86 cm and the location in Y 0.05 cm for field up and -0.13 cm for field down. With the beam location set to -17.85 cm $\pm$ 0.01 cm in Z, the location of the target centre in X was found to be -60.0 cm, in agreement with the survey value. The values in Y were taken to be accurate to within an error of $\pm$ 0.05 cm and selected as 0.0 cm for field up and -.1 cm for field down in later analysis. These final beam values are shown as lines on the plots.

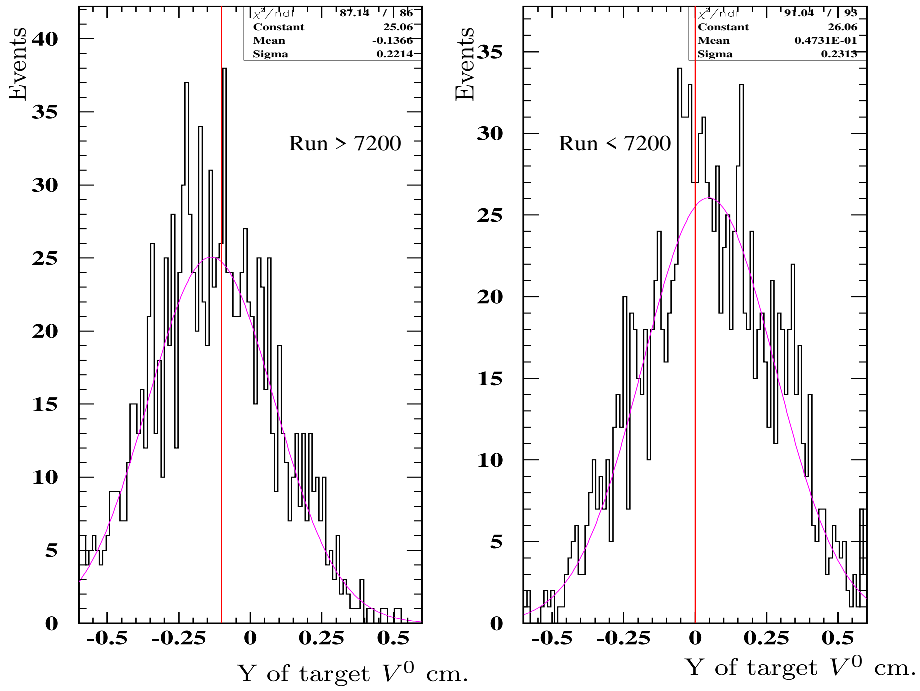

Figure 3.9: Field up and down Y vertex positions for target V^0 candidates in Y

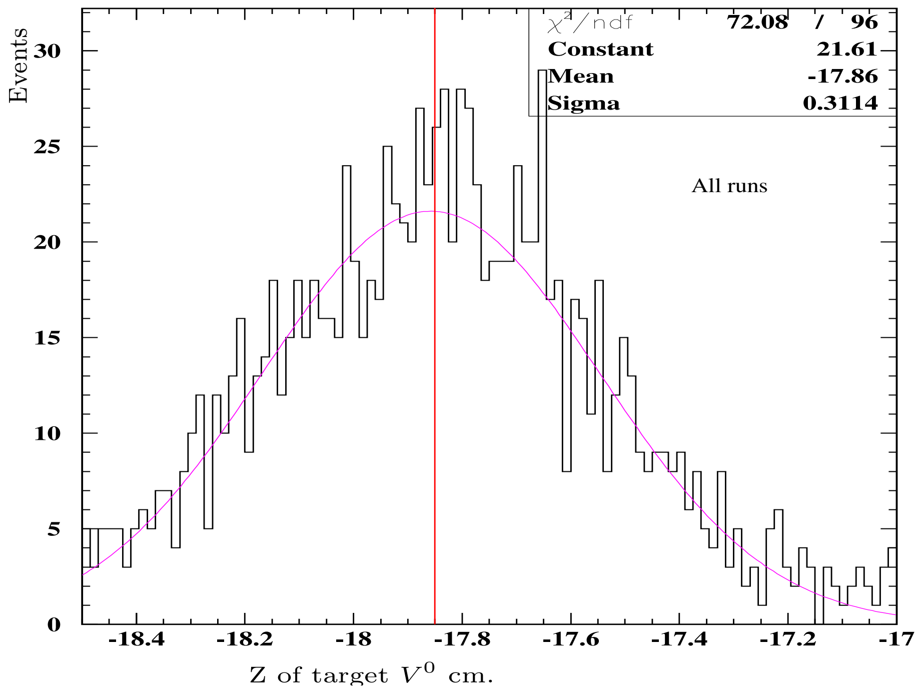

Figure 3.10: All runs for target V^0 candidates in Z

3.4 The Podolanski-Armenteros Plot

The quality of the V^0 candidates can be assessed by studying the Podolanski-Armenteros plot for the p-Be data [50]. This is described in appendix C. Selections were defined to separate Λ,$\overline{\Lambda}$ and K^0 candidates. The Podolanski-Armenteros plot for the 1999 p-Be data is shown in figure 3.11. The data were separated into three regions by selection in the Armenteros 'α' variable. The K^0 region merges into the tails of both Λ regions. This contamination was found to be significant for both Λ samples and removed. Affected events were excluded, with a K^0 mass selection located at 504.0 MeV and with a width of 6.0 MeV, see figure 3.12. The K^0 mass was found to have been shifted from the particle data group value of 497.7 MeV, see [30]. This shift is investigated further in section 3.9 and for this analysis the shifted mass has been used as the centre of the selection.

Another selection was applied to remove contamination from e^+e^- pairs formed via photon conversions. The photon is massless so electrons will be produced with a transverse momentum of zero with respect to the line of flight of the photon. For this reason, photon conversions are restricted to low values of q_t on the Armenteros plot and can be removed. The effect of these selections can be seen in figure 3.12. It is possible to see the background is fairly uniform under the signals, and after the regions had been identified, specific selections on the reconstructed mass of the V^0 were investigated to reduce background further.

Figure 3.11: The Armenteros plot for p-Be 1999 40 A GeV/c data.

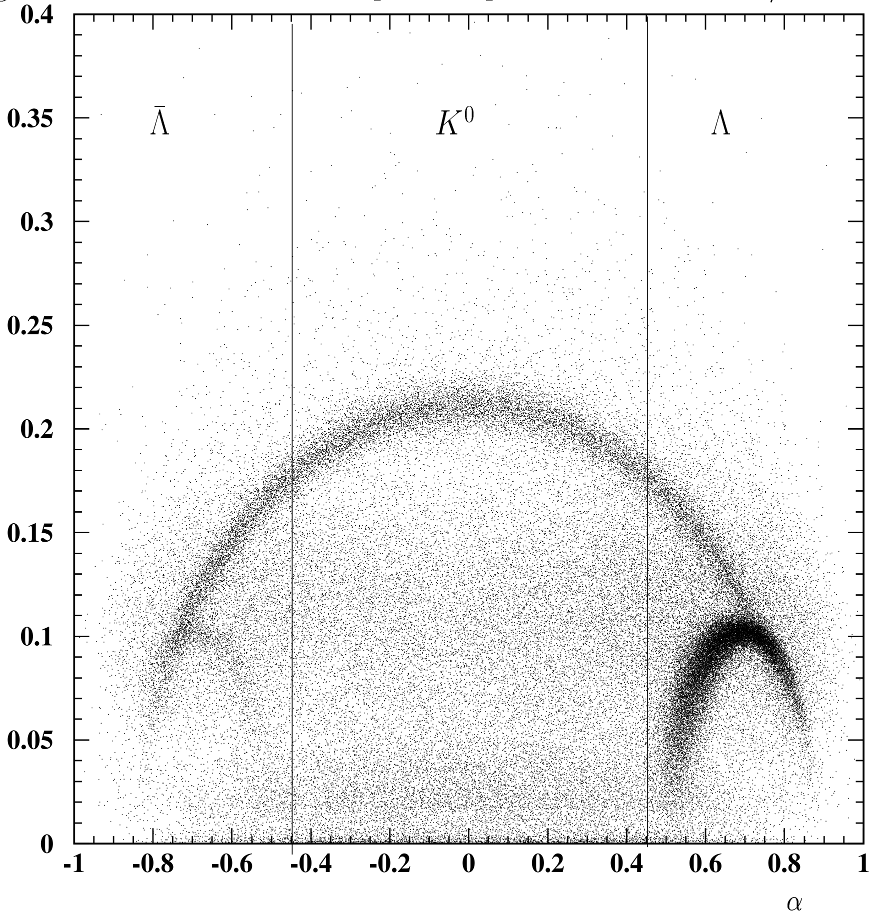

Figure 3.12: Armenteros with selections applied

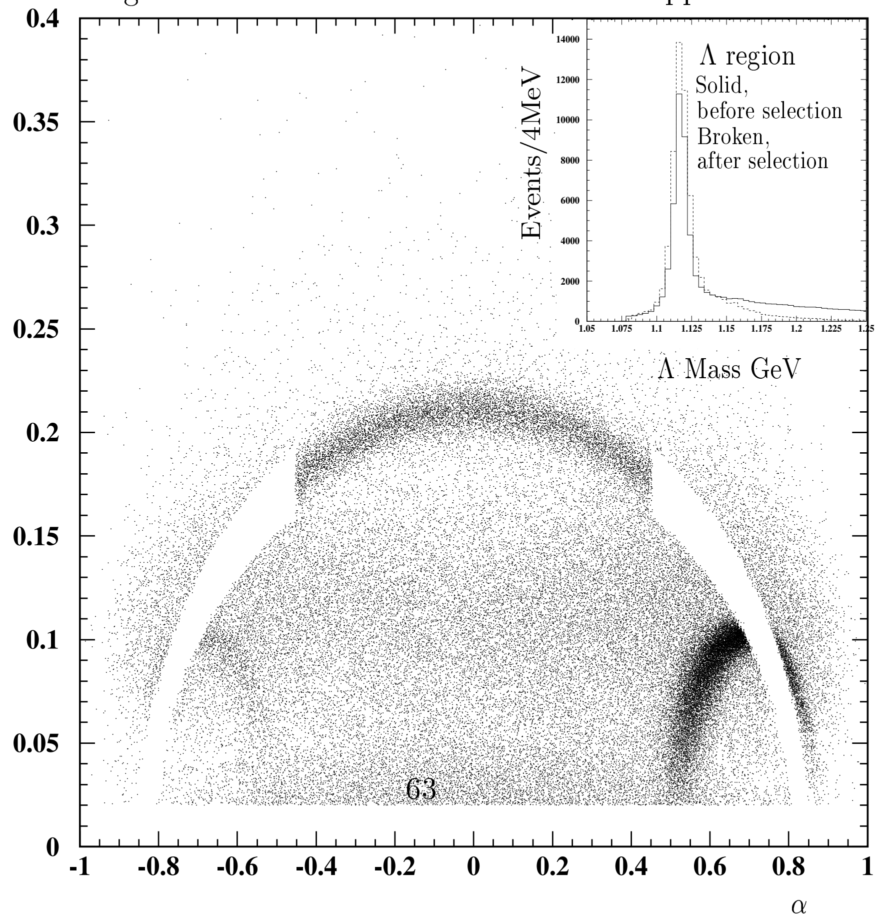

3.5 Secondary Interactions from the Pixel Planes

When the high energy charged tracks strike the pixel plane it is possible that charged particles ejected from the material may be reconstructed as V^0s. If this were to occur either the decay vertex or the crossing vertex of the cowboy decay will originate from the location of the pixel planes. This contamination is removed at the planes from a selection along the X axis, see figure 3.14. The crossing vertex can be reconstructed from the decay vertex by noting,

- The decay tracks follow a circular path in the bend plane so a vector that connects the centres of the two circles must be perpendicular to a vector that connects the decay vertex and the crossing vertex
- Momentum will be conserved at each vertex so the cross product of the momentum of the two tracks at a decay vertex must be equal in magnitude and of opposite sign to the cross product at a crossing vertex

The contamination was most visible in the K_s^0 signal when only selecting on α to remove the Λ and $\overline{\Lambda}$ signal. This is seen figure 3.13, these plots show the sailor vertex along the X axis vs. the sailor line of flight traced back to the target. In the left hand side figure, the K_s^0 signal has been selected with only the α cut, the bands of contamination from the telescope planes are clearly visible. In the right side figure, only the ϕ selection has been added (see section 3.7.4) which dramatically reduced the contamination. On applying all selections, the contamination from the pixel planes was found to be negligible. For p-Be interactions at 40 GeV/c, contamination to the Λ and $\overline{\Lambda}$ could also be ignored after all other selections were applied and so no selections were made using the crossing vertex.

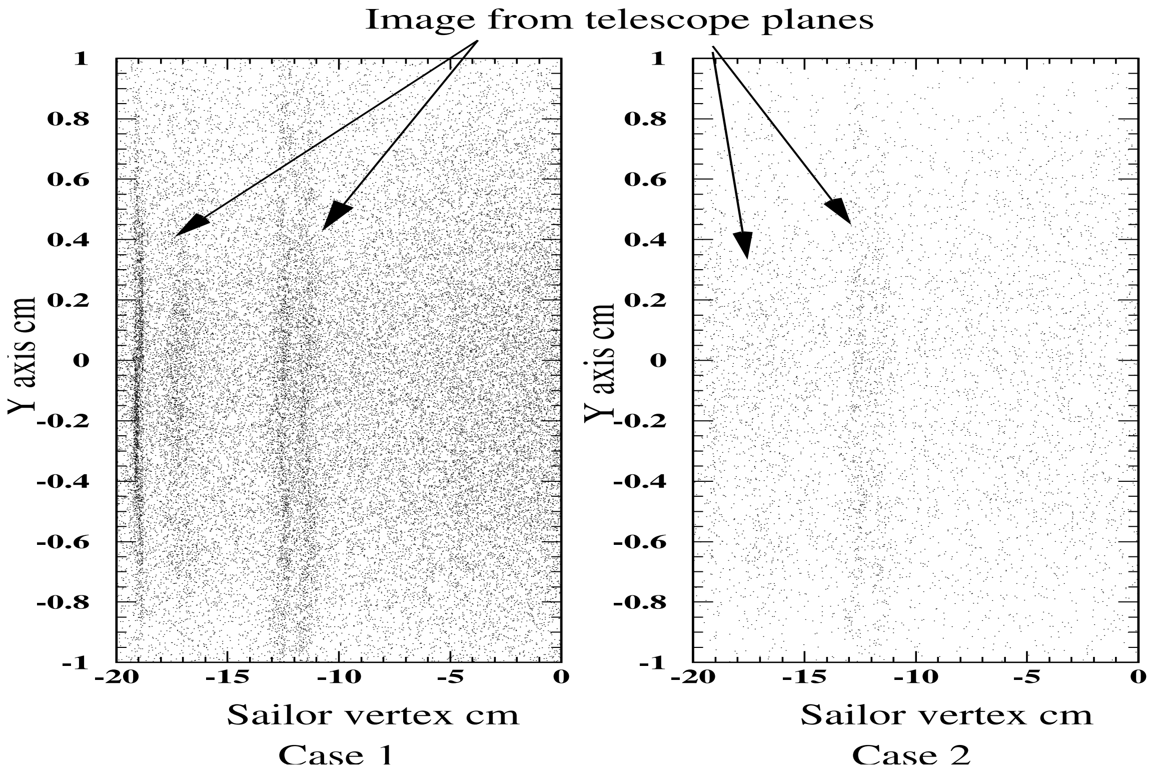

Figure 3.13: Sailor decay vertex vs. Y decay position. Left figure shows K_s^0 with α selection, right figure shows with additional ϕ selection .

3.6 Geometry Selections

A number of selections were made on the geometry of the V^0 interactions. For example, selections were made on the position of the decay vertex of the V^0 along the X axis, called 'XVC'. The intercept of the V^0 line of flight with the Y axis, called 'BYV', and the intercept of the two charged V^0 decay tracks extrapolated to the Y axis, 'BYPOS/BYNEG'. These will be explained in more detail in the following sections, but the main aim of these selections was to reduce contamination from background tracks by confining the decays of the V^0 to different areas of phase space. Figure 3.14 shows the meaning of the above variables diagrammatically, point '1' along the dotted line on the X axis shows BYV, the V^0s line of flight intercept with the Y axis, the arrow labelled '2' shows the decay point of the V^0 along the X axis, XVC and the dotted curved line '3' shows the intercept of a charged track traced back to the Y axis, BYPOS/BYNEG.

To investigate these selections the primary vertex selections were applied and the signal under investigation, $\Lambda, \bar{\Lambda}, K_s^0$ was selected from the raw data using the Armenteros 'α' variable. To inspect a particular variable, it was plotted vs. the reconstructed V^0 mass, allowing any signal to be clearly seen and a selection made on the variable to remove the background, see figure 3.19 for an example of this. Once a selection had been chosen the reconstructed mass distribution of the V^0 decay, with all the selections *apart from* the variable of interest applied, was subtracted from the reconstructed mass with all the selections applied *including* the variable of interest. If the selection only removed background this distribution should not show any signal peak. This process was continued and refined until all the selections were optimised. Finally, as the Λ and $\overline{\Lambda}$ decays only differ by having the order of their charged decay tracks reversed, all the selections for these signals were kept symmetrical.

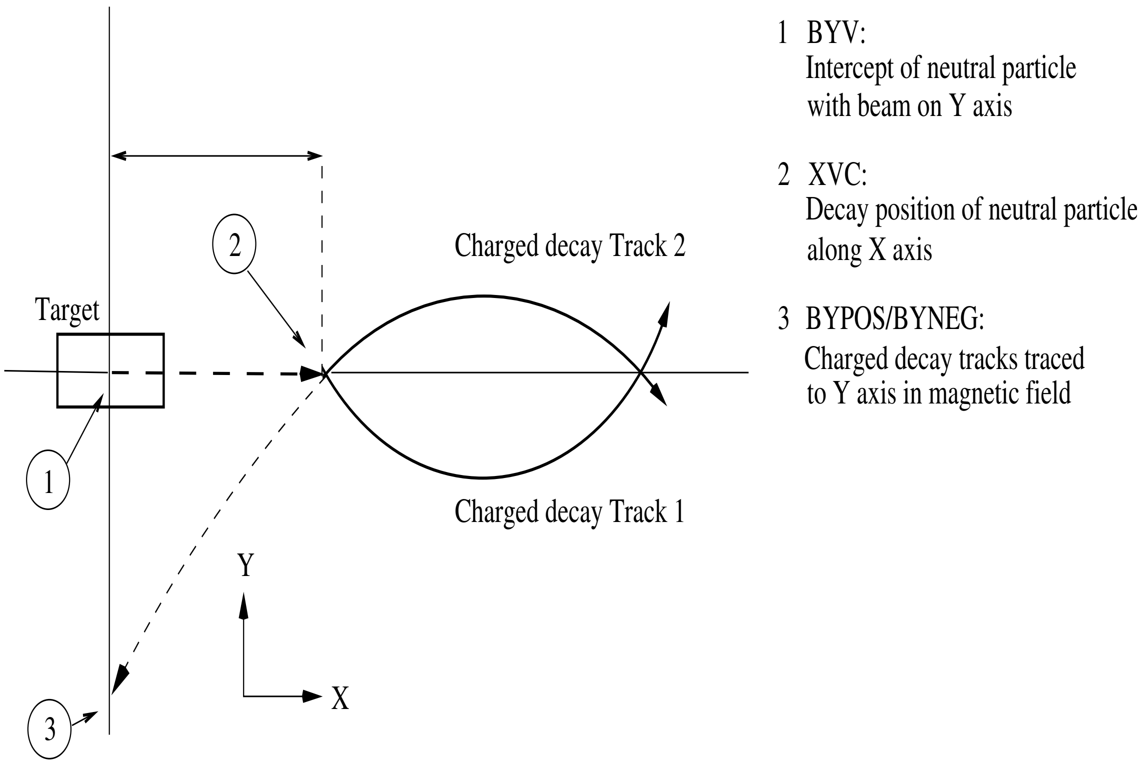

Figure 3.14: Decay selections made on the geometry of V^0.

3.7 V^0 Decay Length XVC

A selection was made on the decay length of the neutral V^0,('XVC' in Fig 3.14). Figure 3.15 shows the mass signal for the Λ plotted against the decay length. The plot shows the two selections used to remove contamination. The first region with the decay length toward the front of the compact telescope, shown to the right of the line -27.5 cm seems to show a clear band of signal but from measurements of the apparatus in the experimental logbook [49] it was found that this region was inside the SPH1 and SPH2 scintillators at the front of the telescope, see figure 2.2. To remove decays that fall inside these scintillators, V^0 decay lengths greater than -27.5 cm were excluded. The second region excluded decay lengths less than -45 cm, again a region of signal seems to be shown but a detailed investigation of this region showed increasing contamination coming from the target where charged tracks, mainly pions, were being reconstructed as V^0 decays, see section 3.3. The contamination is worse with the $\overline{\Lambda}$ signals so this region was removed. The XVC selections were chosen to be the same for the Λ, $\overline{\Lambda}$ and K_s^0 signals, see table 3.1.

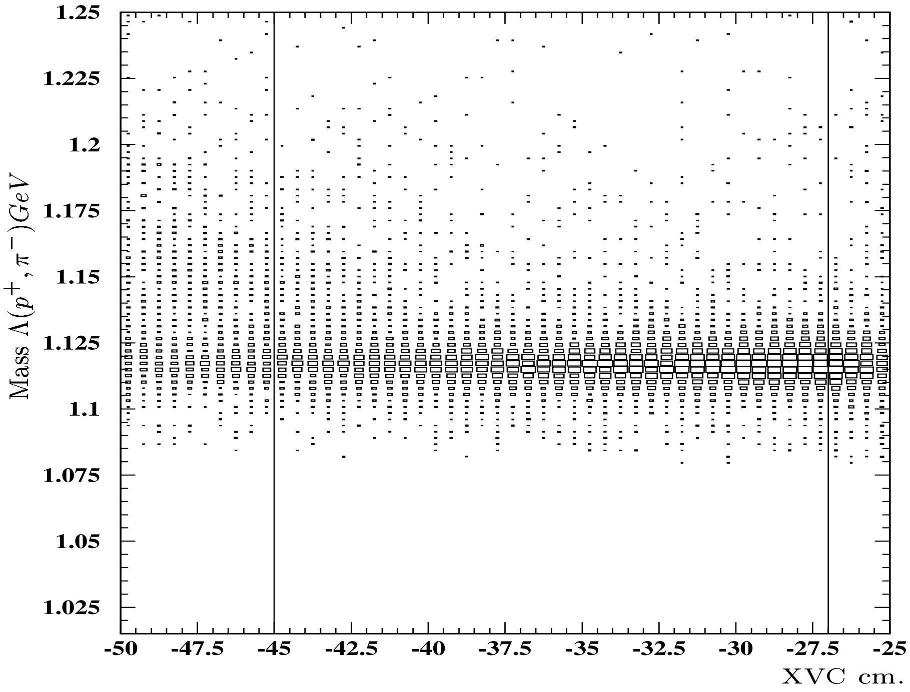

Figure 3.15: Cowboy decay vertex, XVC, vs. Λ mass signal.

3.7.1 Neutral V^0 Impact at Y Axis.

This selection traced the neutral V^0 line of flight back to the X position of the target, see 'BYV' of Fig 3.14. The value for the Y intercept at the target is related to the beam width, a wider beam at the target will give a larger distribution in BYV. The neutral Λ, $\overline{\Lambda}$ and K_s^0 decays should peak around the centre of the Y axis within the spread of the beam, see figure 3.16.

Events outside $\pm$ 0.6 cm along the Y axis were removed for all signals, see table 3.1. It is not possible to apply this procedure to find the origin of the neutral V^0 from the Z axis because the method used to resolve the primary vertex of the

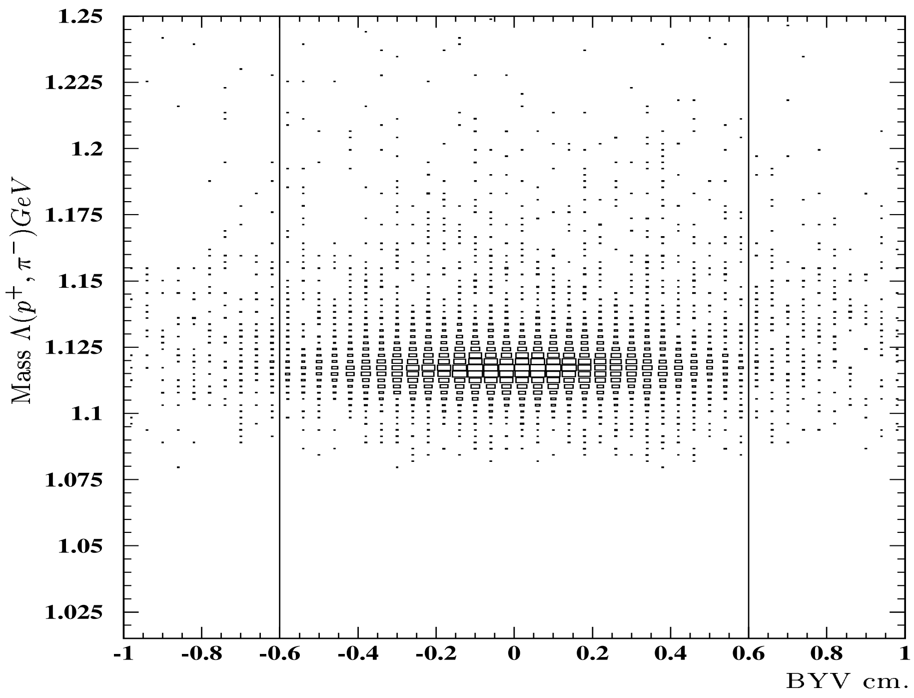

Figure 3.16: Neutral V^0 at Y axis vs. Λ mass signal.

V^0 fixes this at -17.85cm as described in section 3.2.1.

3.7.2 Charged Track Impact Parameter

This method made selections on the charged particles after their trajectories had been traced back to the YZ plane at the target centre X position, see 'BYPOS/BYNEG' of figure 3.14. In figures 3.17 and 3.18 the negative tracks have been extrapolated back to the target Y and Z plane for Λ decays. The negative track in the Λ decay will be a π^- and the distributions are seen to peak away from a central point. This is due to the smaller momentum of the π^- being swept away from the target centre in the magnetic field. Tracks that originate from the centre are likely to be background V^0s and were removed. The higher momentum protons will not have separated as far in the magnetic field, so this selection was not applied. The data were removed inside the following regions around the Y and Z axis for the charged pion tracks, for the Λ, BYNEG less than $\pm$ 0.2 cm and BZNEG less than $\pm$ 0.05 cm. The same selections were made for the $\overline{\Lambda}$ with the signs of the tracks reversed, see tables 3.1 and 3.2. For the K_s^0 decays, data with BYNEG less than $\pm$ 0.4 cm and BZNEG less than $\pm$ 0.1 cm were removed see table 3.3.

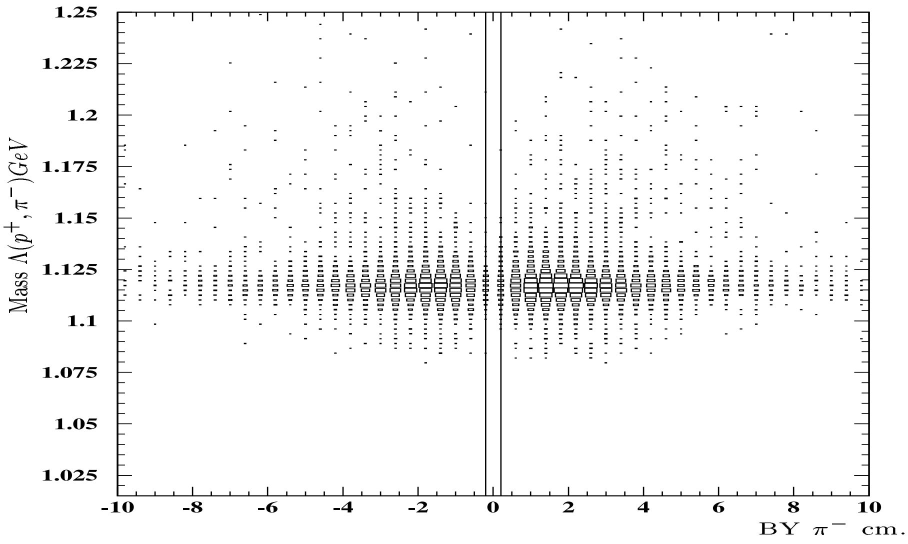

Figure 3.17: BY impact parameters vs. Λ mass signal

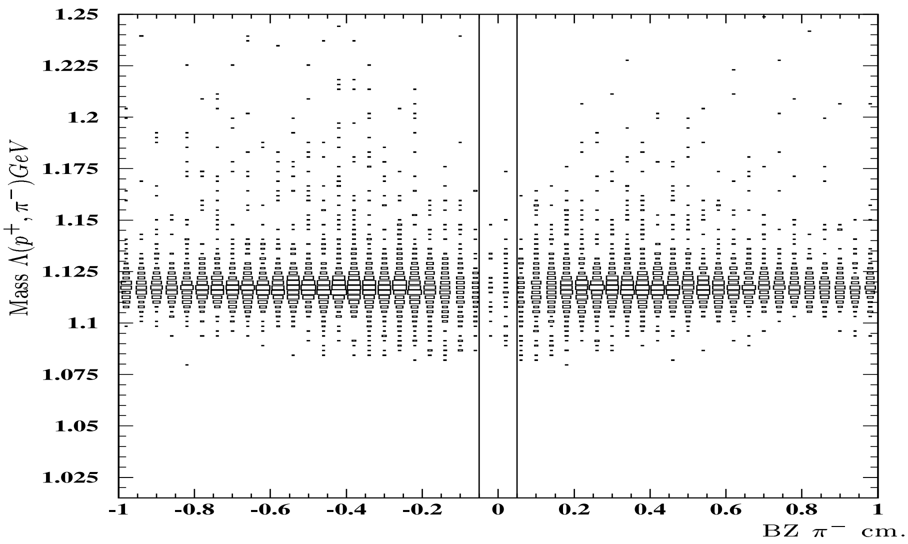

Figure 3.18: BZ impact parameters vs. Λ mass signal

3.7.3 Closeness of Approach

A V^0 is constructed from two charged tracks in three dimensions. There would be a common point of origin for V^0 decay tracks but the finite resolution of the experimental apparatus means this distance between the two charged tracks will not be zero after the reconstruction but will lie within an acceptable range of the closeness of approach. A maximum distance of 0.1 cm was initially taken for the distance between two tracks during construction of V^0s from the raw data but fine tuning of the final $\overline{\Lambda}$ sample reduced this distance to 0.07 cm for all signals, see figure 3.19 and table 3.1.

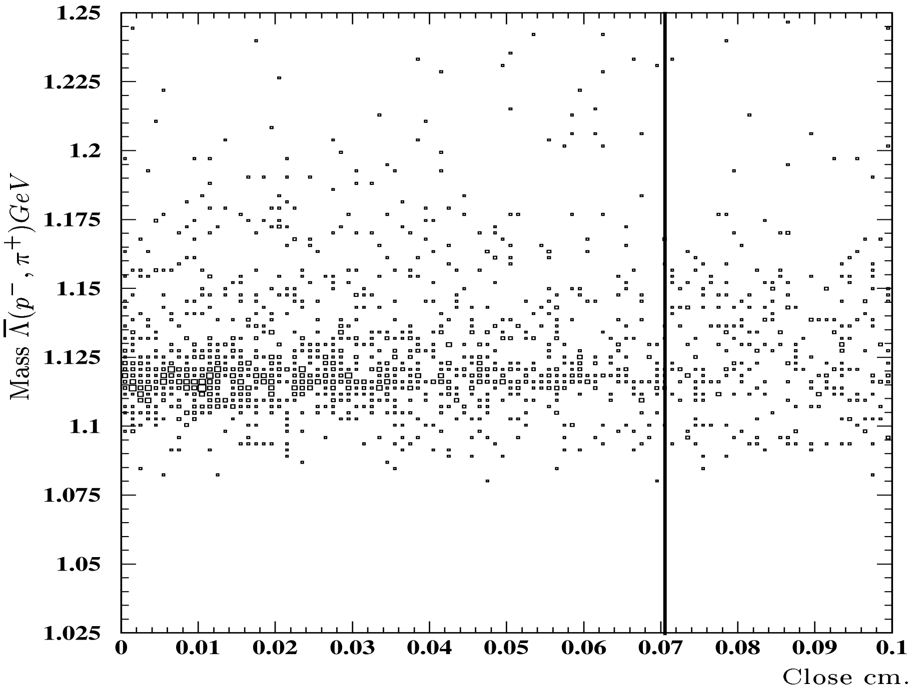

Figure 3.19: Separation of V^0 tracks at decay minima vs. Λ mass signal.

3.7.4 V^0 Decay Angle, ϕ

The topology of a V^0 decay will lie on a plane. ϕ is the angle that the decay plane of the two charged tracks makes with the Z axis when the decay plane intersects the YZ plane, see figure 3.20. The two decay tracks are not quite back-to-back in this projection, but the average ϕ from the two tracks was taken to compensate for this. When $\phi = 0$ radians the V^0 decay plane lies perpendicular to the bend plane, and for small values of ϕ, the tracks will show little curvature as the transverse momentum of the decay vector will be perpendicular to the field vector. This will affect the reconstruction processes in ORHION as the charged tracks will not be swept away from each other in this plane increasing the probability of background tracks reconstructed as V^0 decays. V^0s with small ϕ angles were removed, see figure 3.21. The ϕ selection was only applied to the Λ and $\overline{\Lambda}$ signals, removing all data with ϕ less than 0.10 radians, see table 3.1.

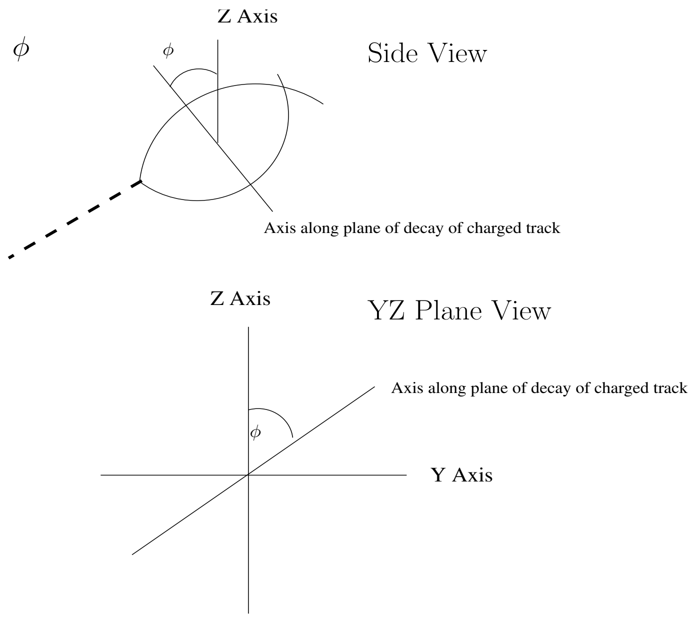

Figure 3.20: ϕ decay angle.

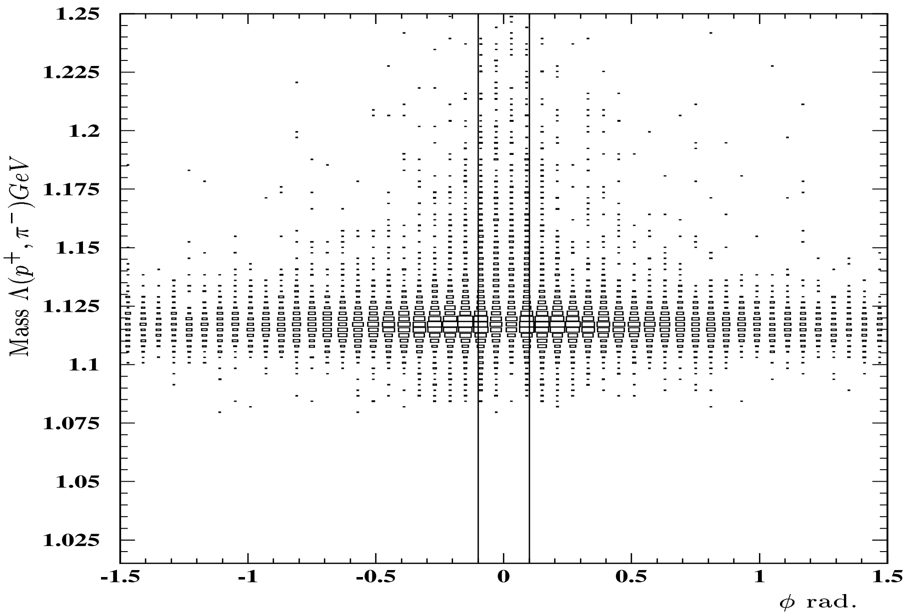

Figure 3.21: ϕ selection vs. Λ mass signal.

3.8 Fine Tuning Selections

The individual selections needed to be tested for stability. With the $\overline{\Lambda}$ signal this was crucial as the selections needed to remove as much background as possible whilst keeping high statistics. The approach to fine tune the selections started by selecting reasonably loose ranges for all the variables and observing the effect of altering a selection on a variable with the other selections applied. The selection under observation was repeatedly adjusted with the other variables until all the selections were optimised. This iterative procedure was particularly important to find the optimum reduction in background, combined with the highest statistics, for the rarer $\overline{\Lambda}$ decays. Figure 3.22 gives an example of this for the BYV selection on the Λ sample. An initial investigation has shown the best selection on BYV to be less than $\pm$ 0.6 cm. With all other selections applied, the impact variable BYV has been separated into six different bins and plotted against mass. In this example the bins span the range 1-6. Each bin width is 0.05 cm and for each of these bins a Gaussian was fitted to the distributions. In figure 3.23 the mean mass of each fit is shown on the left hand side plot. The error on the mean is small enough to ensure that any change in the mean position is not statistical. By bin four the value starts to drift suggesting from figure 3.22 that the background is higher under these bins. On the right hand side plot the spread of each distribution is compared to the first bin. By bin four the distribution width is greater than double. The first bin is clearly inside the signal from figure 3.22 and the selection of 0.6 cm lies between bin 3 and 4. This suggested that widening the selection will not increase the signal. From a visual inspection of figure 3.23, decreasing the selection will remove areas with a strong signal. From this analysis the absolute value of BYV was chosen to be 0.6 cm. The selections were investigated still further by comparing them to Monte Carlo simulations of the experiment, as will be described in the next chapter.

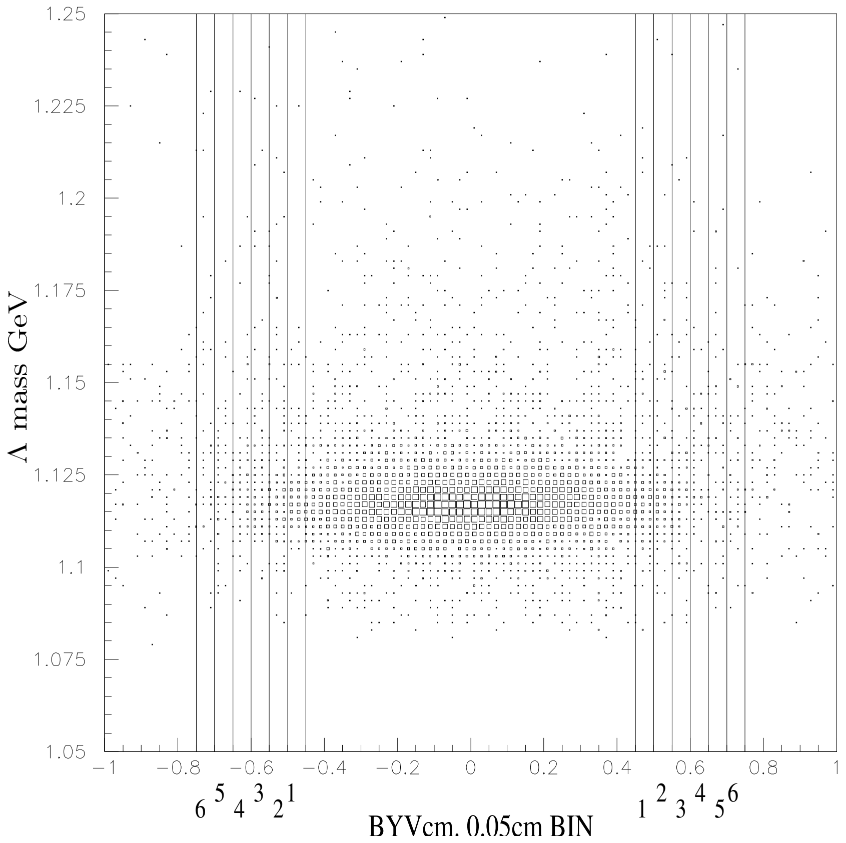

Figure 3.22: BYV vs. Mass. The mass of the (p, π^-) for the six numbered bins, around the $\pm$ 0.6 cm selection, are projected in figure 3.23.

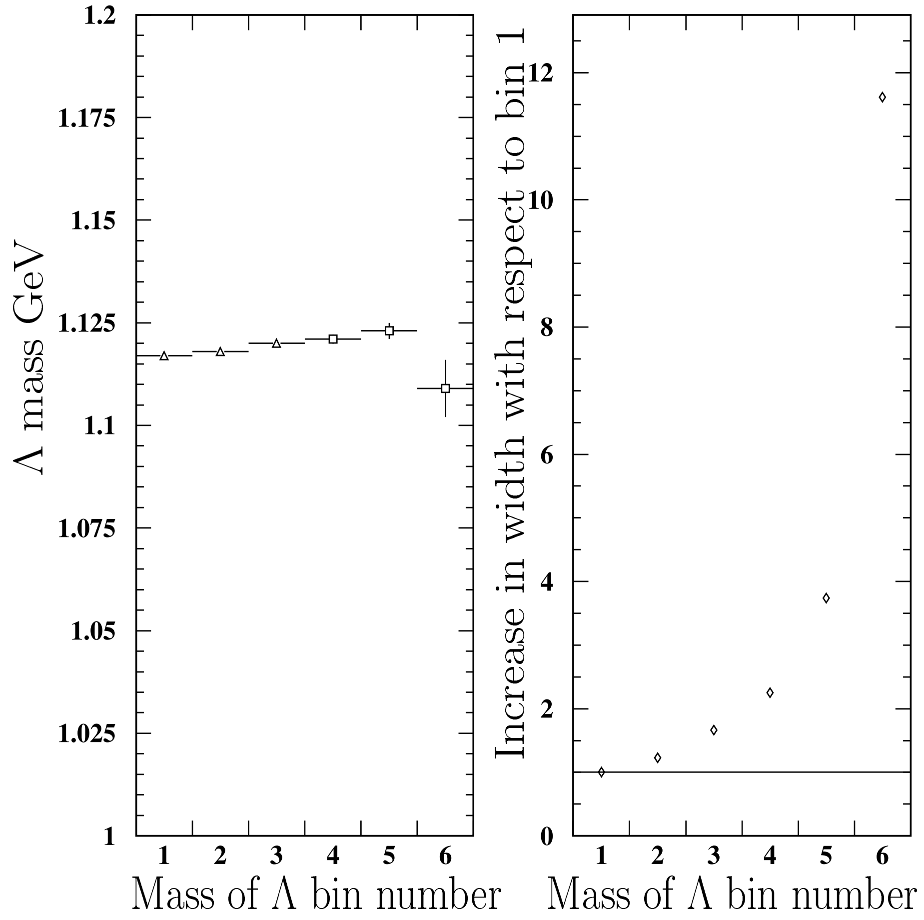

Figure 3.23: Left hand plot shows the mass of the (p, π^-) signal, per bin. Right hand plot shows increasing width of Gaussian fits to the mass signal, per bin, (Points), with respect to the first bin, (Line).

3.9 K^0 Mass Shift

The mass signal for the K^0s was seen shifted by 8 MeV from the Particle Data Book value of 497.7 MeV [30] to 506 MeV ± 0.5 MeV. This could happen if the radius of curvature of the charged V^0 decay tracks in the bend plane is being overestimated. This is possible if the measurement of the length of the compact telescope was overestimated, see figure 2.4. Another possible cause was that the magnetic field had been incorrectly mapped, although this is the most unlikely scenario because the field is mapped quite exhaustively.

The reconstructed mass of the K_s^0 from the two π decay, compared to the Λ decaying to a proton and pion, will be particularly sensitive to errors in momentum reconstruction. This is shown in equation (3.6), where $\mathbf{P}_\pm$ is the momentum vector. The telescope reconstructs the charged tracks of the V^0 to give the momenta of the decay tracks in equation (3.6) but the mass of these decay particles is unknown and taken from the Particle Data Book value [30] for the decay mode of interest.

$$\begin{aligned} Mass^2_{Parent} &= (E_+ + E_-)^2 - (\mathbf{P}_+ - \mathbf{P}_-)^2 \qquad (3.6) \\ \text{Where } +/- &\quad \text{are} \quad \text{the charged decay tracks} \end{aligned}$$

The sensitivity to the momentum reconstruction can be evaluated by looking at the mass difference of the parent and decay products. The larger this difference, the more sensitive the parent mass will be to errors in the momentum. For the two pion decay of the K_s^0 this is 497.7_{K^0} MeV -2 $\times$ 139.57_π, so about 64% of the reconstructed K_s^0 mass comes from the momentum measured by the telescope. For Λ decays this value is 1115.68_Λ - (938.27_{proton} + 139.57_π), or about 4% of the reconstructed mass coming from the momentum measured by the telescope, which explains why this shift was not visible in the Λ and $\overline{\Lambda}$ mass signals see figure 3.26.

A small mass shift in the K_s^0 signal can be tolerated if it is uniform in transverse momentum, as our interest lies with the final yields of particles and inverse slopes, which would remain intact under such a shift, see section 4.3. This translates as being uniform along the length of the decay the V^0 along the X axis.

To investigate the stability of the mass shift, the decay position of the K_s^0 along the X axis, the XVC position, figure 3.14, was split into bins. If each cowboy topology has approximately the same momentum, each region will be reconstructed to give a constant mass shift in each bin along this axis, see figure 3.24. Data from the experiment were taken in both magnetic field polarities to test that the mass shift was not correlated with the field direction. The mass shift per bin was found to be constant. The figures 3.24 shows that the mass shift is stable along the X axis and even though the width of the mass peak increases, this increase is 0.5 MeV over the 40 cm decay length and is stable. The field direction was also investigated, see figure 3.25, and did not affect the shift with a change in polarity. In conclusion, the K_s^0 mass shift was stable and could be tolerated in further analysis.

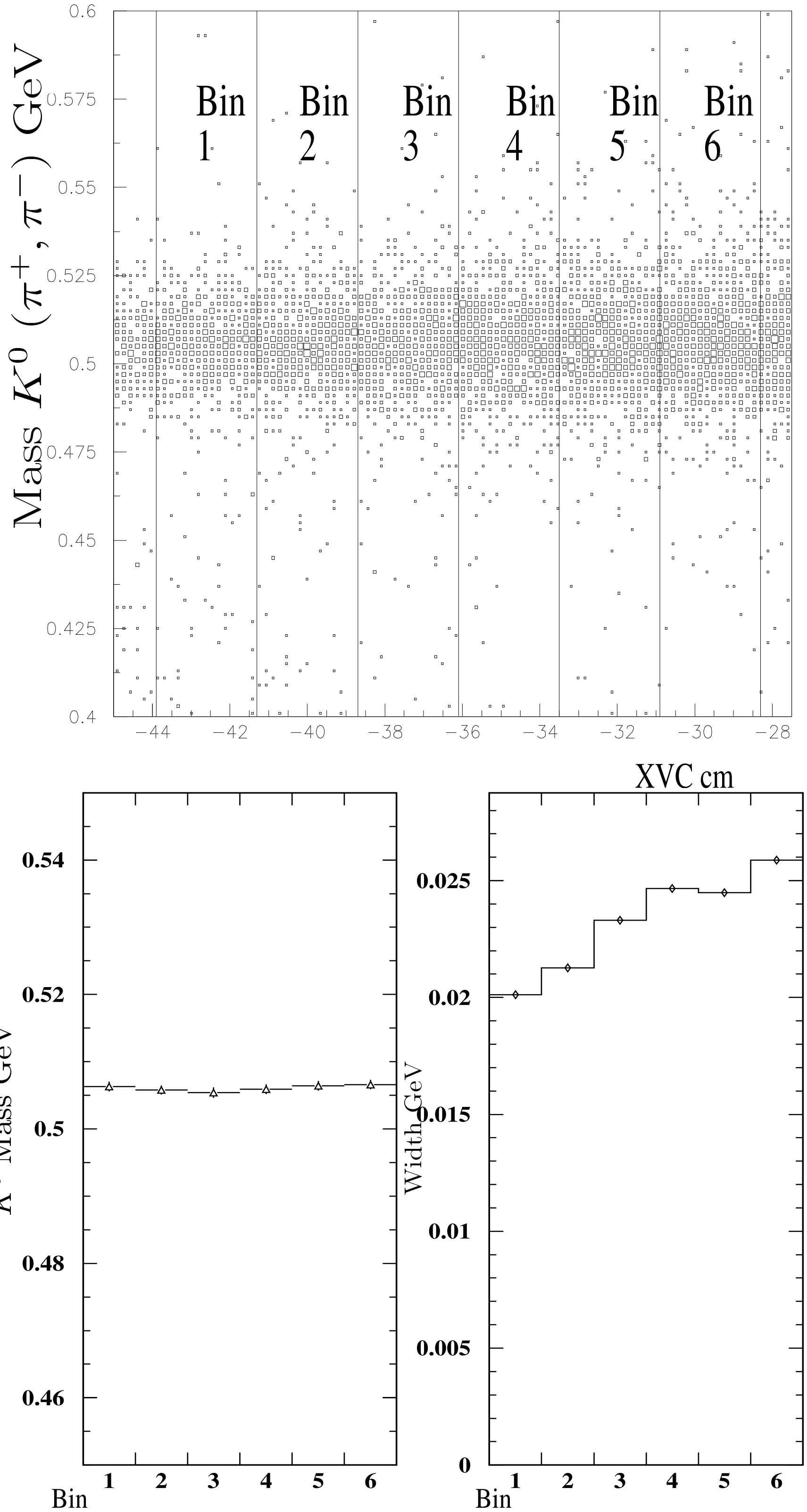

LHS plot shows mean. RHS plot shows 1σ fit per bin

Figure 3.24: K^0 mass shift vs. decay length over four bins.

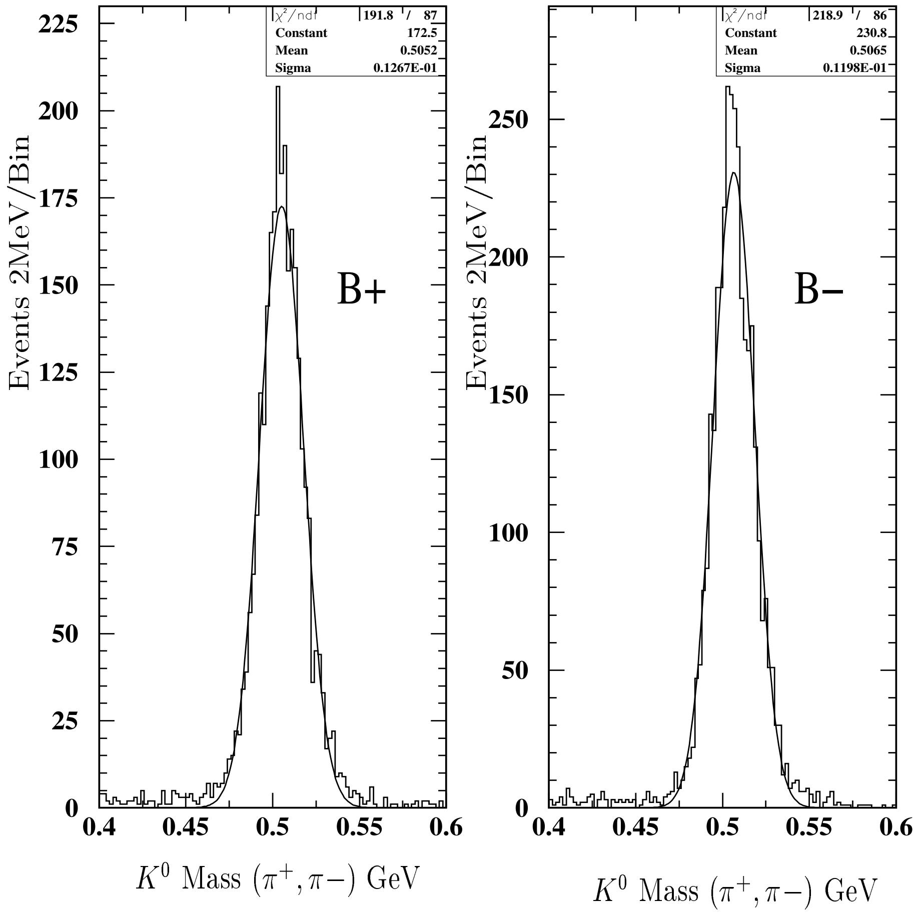

Figure 3.25: K^0 mass shift vs. field direction.

3.10 'Gold plated' Signals

Table 3.1 gives a list of final selections used to select 'gold plated' decays for the Λ data. Table 3.2 lists the differences between these selections and those used for the $\overline{\Lambda}$ decays and table 3.3 for the K_s^0 decays. With all the selections applied the mass signals are shown in figure 3.26. The window shows these plots with only the α selection, compared to the reduction in background achieved by the selection procedure. The gold plated selections were then corrected for acceptance and the geometry of the experiment and final yields and inverse slopes produced, as discussed in the next chapter. This procedure assumes that the background is small under the signals to be corrected and a mass cut can be applied to remove the tails of the distributions from the weighting procedure. These are shown as the 2.5σ lines on figure 3.26. The background under the $\overline{\Lambda}$ signal is too high to justify this assumption and a background correction procedure was applied to this signal, as discussed in the next chapter.

3.10.1 Candidates and Raw Ratios

Table 3.4, gives the number of gold plated candidates found and ratios from the uncorrected data with the background calculated in chapter 4 using V^0 mixing, at 24% to correct the $\overline{\Lambda}$ signal.

Table 3.1: Selections used for the Λ 'gold plated' decays

No.	Name	Λ Selection	Notes
Vertex			
1.	Remove bad runs. XY(Bend) plane. Plane at -17.85 in Z	7100>RUN No. -1cm<Y<1cm -67.5cm<X<-52.5cm	Selection in X removes the S4 counter. see sec 3.2
Armenteros			
2.	α	$\alpha > 0.45$	
3.	K_s^0 mass cut	|(Mass-0.504GeV)| $> 0.03GeV$	This will remove the large background from K_s^0. contamination.See sec. 3.2.1
4.	High/Low $Q_t$cuts	$0.02GeV$ $> Q_t >$ $0.30GeV$	The low Q_t selection removes e^+e^- pairs. See sec. 3.4
Geometric Selections			
5.	XVC	-45cm $> XVC >$ -27cm	See sec. 3.7
6.	BYV	$\mid BYV \mid < 0.6cm$	See sec. 3.7.1
7.	$BY\pi^-$	$\mid BY\pi^- \mid > 0.2cm$	See sec. 3.7.2
8.	$BZ\pi^-$	$\mid BZ\pi^- \mid > 0.05cm$	See sec. 3.7.2
9.	$Close$	$Close < 0.07cm$	See sec. 3.7.3
V^0 decay angle			
10.	ϕ	ϕ >0.10 rads.	See sec. 3.7.4

Table 3.2: Change in selections used for the $\overline{\Lambda}$ 'gold plated' decays from table 3.1

No.	Name	$\overline{\Lambda}$ Selection	Notes
Armenteros			
2.	α	$\alpha < -0.45$	
7.	$BY\pi^+$	$\mid BY\pi^+ \mid > 0.2cm$	Selection identical with track sign change
8.	$BZ\pi^+$	$\mid BZ\pi^+ \mid > 0.05cm$	Selection identical with track sign change

Table 3.3: Change in selections used for the K_s^0 'gold plated' decays from table 3.1

No.	Name	K_s^0 Selection	Notes
Armenteros			
2.	α	$-0.45 < \alpha < 0.45$	
3.	K_s^0 mass cut	No mass cut	This cut is not applied for K_s^0
Geometric Selections			
7.	$BY(\pi^-, \pi^+)$	$\mid BY(\pi^-, \pi^+) \mid > 0.4cm$	
8.	$BZ(\pi^-, \pi^+)$	$\mid BZ(\pi^-, \pi^+) \mid > 0.1cm$	
V^0 decay angle			
10.	ϕ	No cut applied	

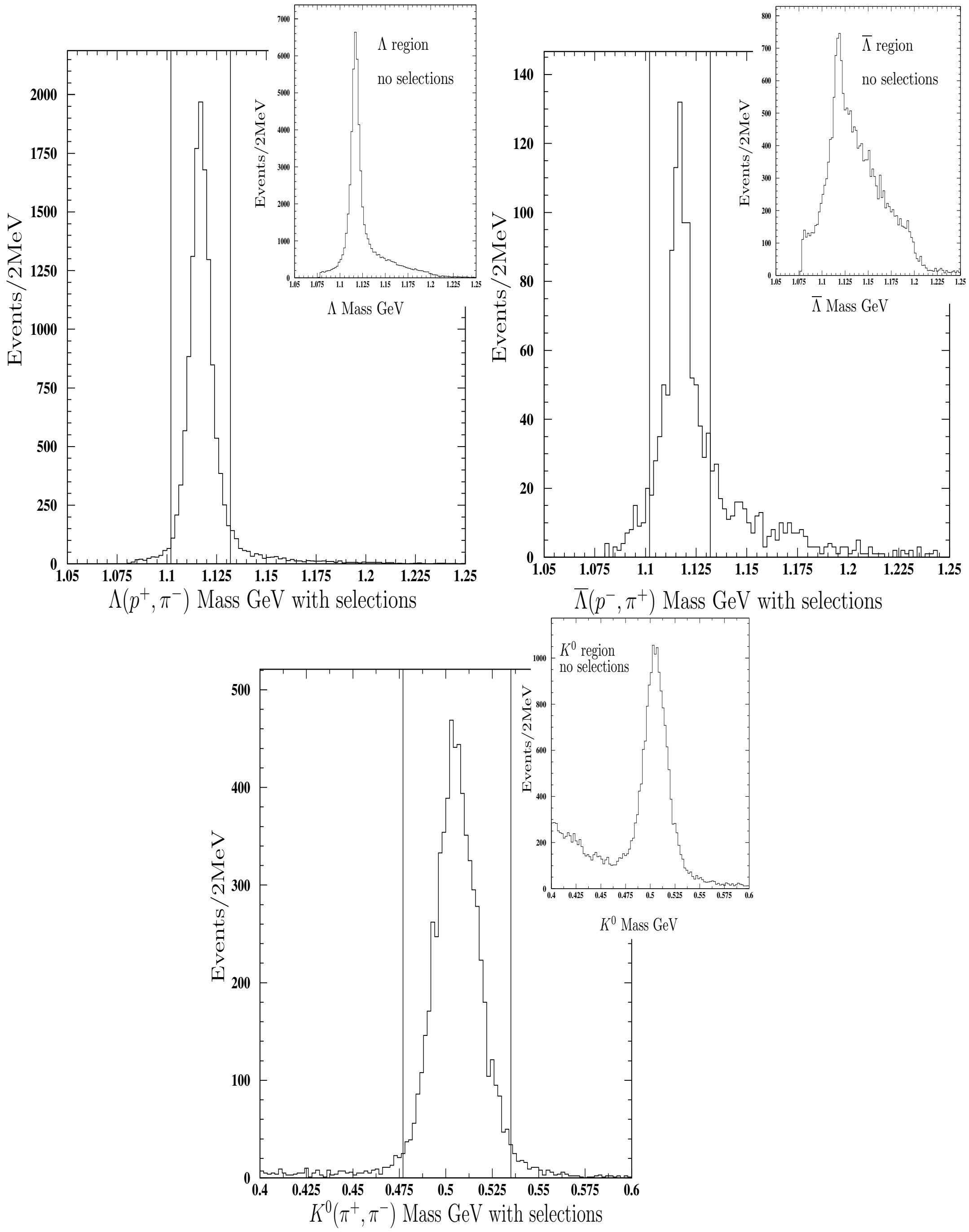

Figure 3.26: Final mass of Λ, $\overline{\Lambda}$ and K_s^0.

Table 3.4: Raw yields and ratios for the 'gold plated' decays

Type	Number Found	2.5σ Mass Cut
Λ	13,613	12,312
$\bar{\Lambda}$	1330	911
$\bar{\Lambda}_{BC}$ with 24% Background Correction	-	692
$\frac{\bar{\Lambda}_{BC}}{\Lambda}$	-	0.056 ± 0.002
K_s^0	7222	6160

Chapter 4

Event Correction and Results

In order to obtain physical results from raw measurements, the measured events have to be corrected for losses. Different hyperon species have different detection and acceptance efficiencies that have to be taken into account. The signal selections from the data were corrected using Monte Carlo simulations of the experimental setup and a 'weighting chain' to correct the sample. After the signals of interest have been weighted, the acceptance and reconstruction efficiency, both, in general, non-uniform functions of the kinematic variables, can be taken into account before the final calculation of results. A plot of the transverse mass (m_t) vs. the rapidity is correlated to the acceptance of the experiment, shown in figure. 4.1, (see appendices A and B). For a given particle, the m_t and rapidity are used by the Monte Carlo program, GEANT, to simulate particles coming from the target with a fixed beam angle, distributed in a cone, along the length of the target. These particles and their decay products are traced through the experimental setup. This continues until 5000 of these simulated decays have accumulated, which have passed through the detector volume. GEANT records the charged track hits on the pixel planes. This is fed into a mixing stage which adjusts the hits on the pixel planes to take account of the real pixel plane efficiencies, see table 4.1, and adds hits to the pixel planes from background data, recorded during the experimental data-taking.

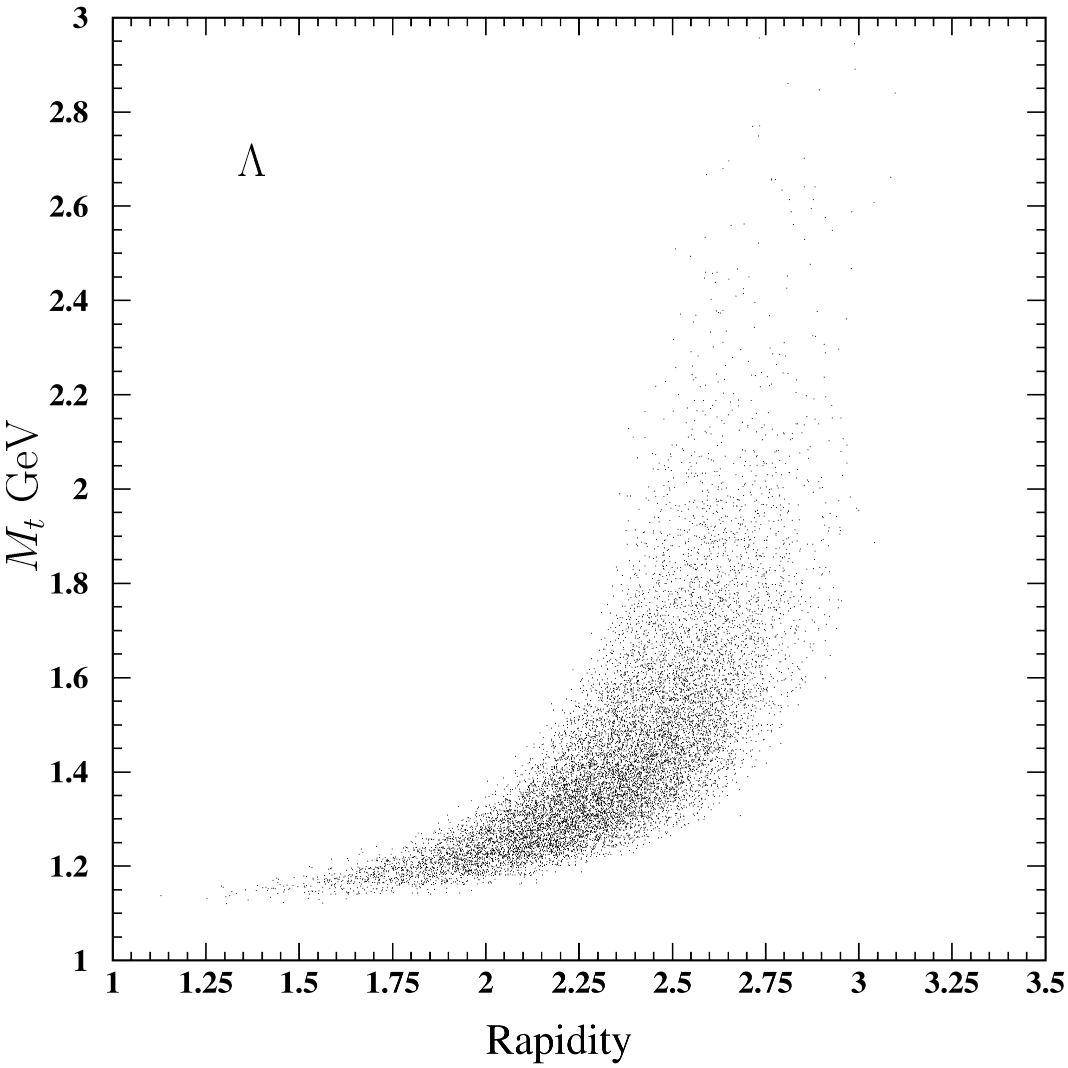

Figure 4.1: Scatter plot of transverse mass vs. rapidity for the uncorrected 1999 dataset

The background data were constructed from two experimental runs taken using both field polarities and the 1 track trigger condition, see Chapter 3. The overall efficiency of the pixel planes in the compact telescope was found to be around 80%, see table 4.1, [1]. These results are similar to the plane efficiencies for the 40 GeV/c 1999 lead-lead data-taking. The data from the mixing stage can then be fed into the same software that was used during the experimental data-taking to reconstruct the real signals. This process is referred to as the 'weighting chain'. The ratio

Table 4.1: Summary of 1999 p-Be plane efficiencies, (validity period 2-9)[1]

Plane	**Efficiency**	**Plane**	**Efficiency**
1	78.50 ± 0.22 %	6	89.77 ± 0.14 %
2	87.25 ± 0.15 %	7	69.12 ± 0.25 %
3	78.48 ± 0.22 %	8	90.74 ± 0.13 %
4	83.45 ± 0.17 %	9	78.71 ± 0.22 %
5	67.70 ± 0.25 %	10	79.53 ± 0.21 %

Average	80.33 ± 0.05%

of tries by GEANT to find a particle that passes through the telescope volume to the number of reconstructed particles for the signal of interest gives a weight, see equation (4.1). A weight is generated from the m_t and rapidity for each particle with a selection of the 'Gold Plated' particles found in the previous chapter. The process is shown diagrammatically in figure 4.2. Using just a sample of the gold plated V^0s, see table 3.4, it is still a computationally heavy task that would have been too time consuming for a single PC to generate statistically significant results. To improve the weight calculation times the weighting chain was tested and run on the new computer farms being installed at Birmingham University.

$$Weight = \frac{Number\ of\ particles\ generated}{Number\ of\ particles\ found} \tag{4.1}$$

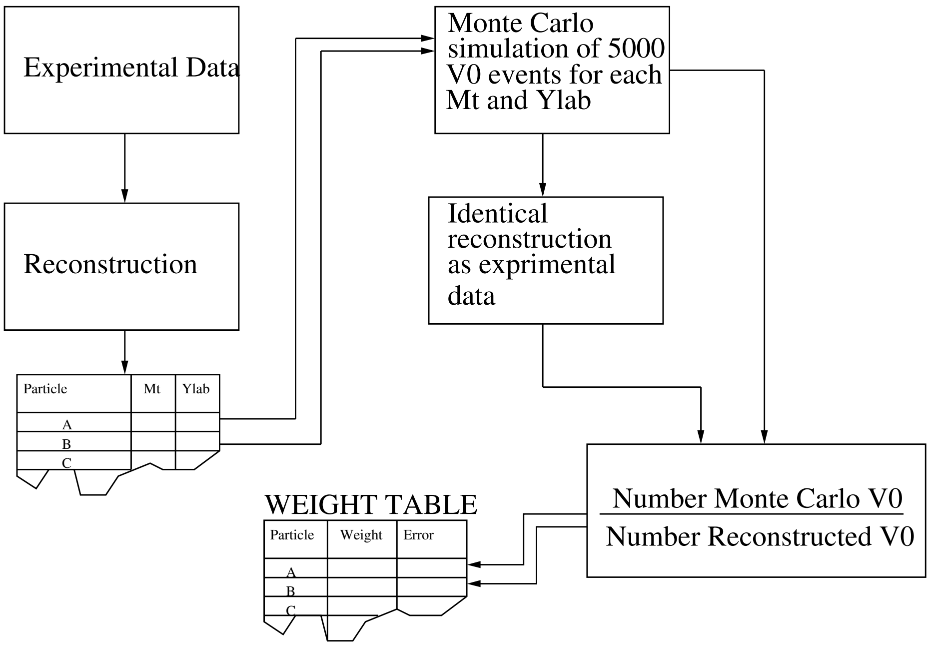

Figure 4.2: Flow diagram of data Correction Procedure

4.0.2 The Tuning of the Monte Carlo Program

The GEANT simulation needed a number of modifications to reproduce the correct beam interaction with the target. The beam spread was simulated using a Gaussian distribution of the generated V^0s in the YZ plane of the beam at the target. The thick target was simulated by using a uniform distribution of the V^0s generated along the 3.26 cm length of the X axis of the target. The wide beam was also shaped somewhat by the 4mm$\times$4mm S4 counter, as the tails of the beam distribution spread outside the active area of this counter, see figure 2.2 and section 2.6.

4.0.3 Beam Spread and S4

Beam interactions that did not trigger S4 would not have been recorded during data-taking. This needed to be taken into account within the weighting procedure. Any generated V^0 that were outside the S4 scintillator 'shadow' on the target should not be counted in the numerator of equation (4.1). Once the S4 trigger and the beam spread were added to the Monte Carlo they needed careful tuning to reproduce the real beam distributions and shadow effects correctly. The beam spot distribution was analysed from the V^0 intercept method, see section 3.2.2, but the resolution was too low to define the location of the beam centre in Z by setting the interaction peak at X to -60 cm and gave no information about the beam centre in the Y axis. The 'Target V^0' method, see section 3.3 and V^0 intercept method, see section 3.2.1, gave a measurement of the beam spread at 1 σ of .50 cm in Y and 1.0 cm in Z. The target V^0 method was then used to locate the beam centre at -17.85 cm in Z and 0.00 cm in Y for field up, -0.01 cm in Y for field down, (0.00/-0.1 cm for $B^{\pm}$).

The Monte Carlo program was modified to generate a distribution of V^0 decays over the m_t and rapidity range within the experimental range of the acceptance window of the real data, see figure. 4.1. This allowed the interaction vertex from the MC distributions to be compared to real data. Using this method the beam 'shape' and spread were found to agree with the real data.

After adding the S4 counter it was found that the location of the interactions along X at the target centre were strongly correlated to the location of this counter with respect to the beam centre. This is due to the distributions along the Z axis being correlated to the location of the target centre along X via equation (3.5). With the beam centre located at -17.85 cm, the centre of S4 along Z was offset from the beam centre from -17.85 cm to -17.90 cm, see figure 4.3. A value of S4 of -17.9 cm fixes the primary vertex to the measured value of the target centre at -60 cm. This agrees with the surveyed position of the S4 counter from the logbook of -17.9 cm, [30].

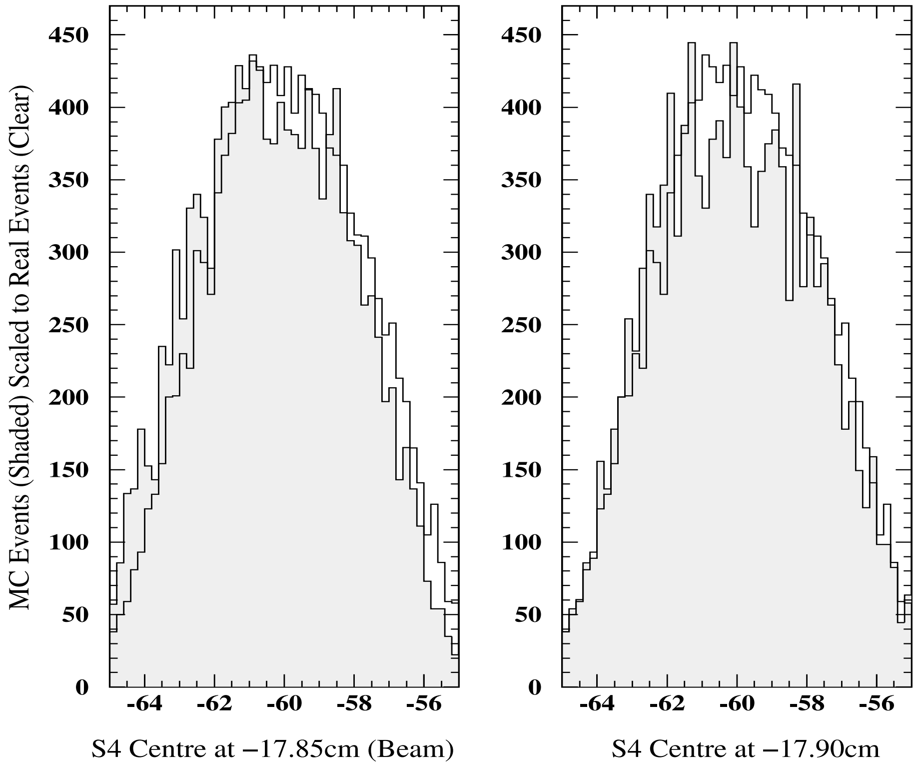

Figure 4.3: Sensitivity of target centre location to S4 centre along Z axis location. The preferred centre for the beam Z distribution is at 17.9 cm.

4.1 Weight Chain Validity

After a number of detailed tests were carried out to validate each stage of the chain, a final test was used to examine the overall functioning of the weighting chain procedure. The MC was altered to simulate particles coming from a source with a fixed temperature. This is related to the 'Inverse Slope' that will be calculated with the real data. Particles were simulated over all m_t and within one unit of rapidity around mid-rapidity, see section 4.3. This sample could then be weighted with the weighting chain as if it were the real data and the inverse slope calculated from the result. If the chain functioned correctly, the value of the simulated inverse slope would be reproduced from the inverse slope reconstructed from the weighted sample. It was found that there were small deviations which depended on the way an acceptance window was constructed for the weighted sample. This will have to be accounted for in the real samples, see section 4.3. With a MC (GEANT) simulation of decays at 169 MeV, the weighted inverse slope from the simulation was found to be 163 MeV $\pm$ 3 MeV (Statistical) $\pm$ 2 MeV(Window). The simulated inverse slope and weighted inverse slope were found to be in good agreement with each other.

4.1.1 Comparison of Real and Simulated Variables

In figure 4.4, the selections on the real data (points with error bars) were compared with the weighted data (dashed line). This allowed a fine tuning of the selections and that could be continued until the selections were optimised for the 1999 p-Be data set. The two figures show examples of a comparison between the weighted and unweighted data. The left hand side figure shows the V^0 line of flight intercept with the Y axis at the target, 'BYV'. The right hand side figure shows the V^0 decay position, 'XVC'. The left hand figure, shows a slightly wider peak for the real data along the leading edge. In the mixing stage the detection efficiency of the telescope's pixels are included as efficiency maps for groups of pixels. However, the finite resolution of the individual pixels may cause a smearing of the real data. The effect is close to the ±0.6cm selection made on this variable and the error on the real data means that this effect on the weighting chain is negligible.

The right hand side figure shows the decay position of the V^0 along the X axis. These plots were used to optimise the selections that remove contamination from the telescope scintillators (right side of figure) and secondary target interactions (left side of figure).

Figure 4.5 shows the final weighted mass plots for the real Λ signal compared

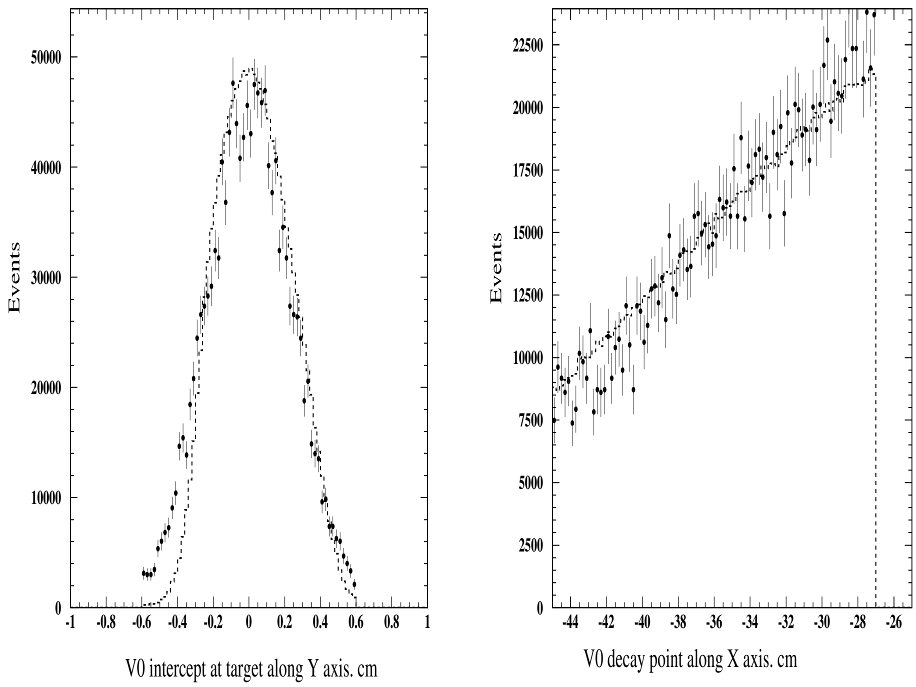

Figure 4.4: Real data (points with error bars) normalised to the weighted data (dashed line) for comparison. Left side plot shows the V^0 impact at the Y axis of the target, the right hand side plot shows the decay position of the V^0 along the X axis.

to the unweighted signal. Only a sample of candidate particles were weighted for the Λ and K_s^0 particles due to computing time considerations, but these plots show that the samples were compatible. For the $\overline{\Lambda}$ the full sample was weighted.

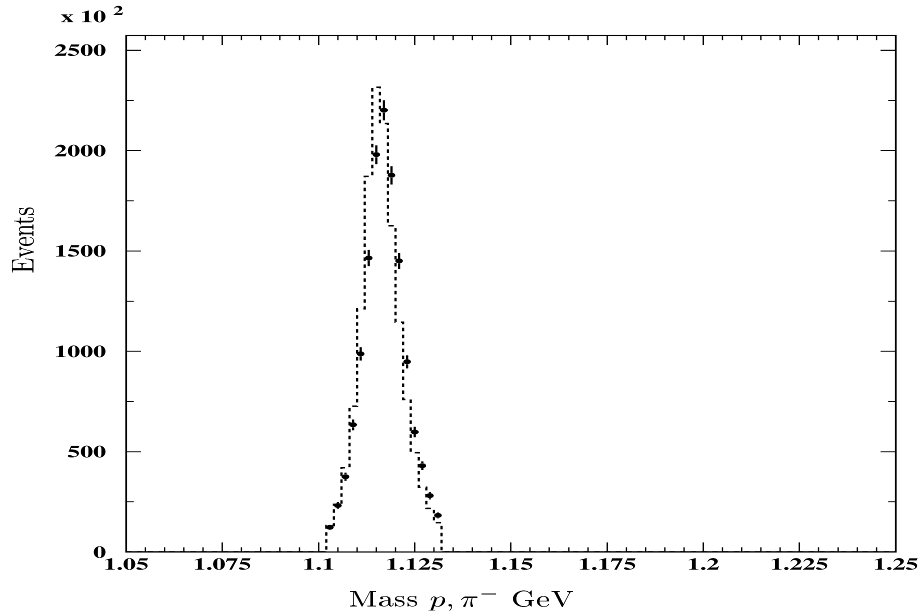

Figure 4.5: Real Λ mass signal (points with error bars) normalised to the mass signal after weighting (dashed line) for comparison.

4.2 Background Correction

To reduce the systematics of the final physics results the background under the signals should be kept as small as possible. In previous data runs of the NA57 experiment it has been found that the background is effectively negligible under the $\overline{\Lambda}$ signal. These runs were at a higher collision energy. This is not the case with the $\overline{\Lambda}$ from the 40 GeV, 1999 sample, see figure 3.26. A large background can be seen under the $\overline{\Lambda}$ signal when compared to the Λ signal that would need to be corrected. The level of background under the signal can be investigated if we have a source of pure background. There were two different ways to do this which gave a similar estimate of the result.

4.2.1 Background and the Weighting Chain

Before any background corrections could be made the effect of the weighting chain on the background had to be considered, as the background distribution may have been distorted by the weighting procedure. This could be tested by seeing if the weight distribution under the signal and the tails of background were uniform. In figure 4.6 the weights for the $\overline{\Lambda}$, (Y axis) have been plotted against the reconstructed $\overline{\Lambda}$ mass (X axis). The weights have been averaged for each bin (points with error bars) to allow the trend over the $\overline{\Lambda}$ mass and tails of the $\overline{\Lambda}$ background to be compared. The weights in the region of the signal peak, 1.1-1.3 GeV are flat and similar to the weights in the tails outside this region. It was concluded that weighting procedure would have a uniform effect on the background, allowing background corrections to the unweighted signal to be applied directly to the weighted signal.

4.2.2 Background Estimation using the Λ Signal

As the weighting does not distort the background the first estimate for a correction can be made by comparing the $\overline{\Lambda}$ and the Λ mass signals. The Λ signal has almost an order of magnitude more events than the $\overline{\Lambda}$ signal. It can be assumed that the background under the signal will therefore be negligible when compared to that of the $\overline{\Lambda}$. The width of the signal for the pure Λ and $\overline{\Lambda}$ will be the same, so, by scaling the two signals together and subtracting the remainder will be the background. It is assumed that the background should be uniform and wider than the signal if the scaling is correct. If the scaling of the signal to be subtracted is too large or small, after subtraction, the background will not be uniform. If the scaling is incorrect the signal peak distribution will be visible in the background distribution. The correct scaling can then be found using a fitting routine to optimise the scaling for a uniform background distribution. The scaled peak and background are shown in figure 4.7. The scaling had large errors and a value for this plot was chosen that matched the

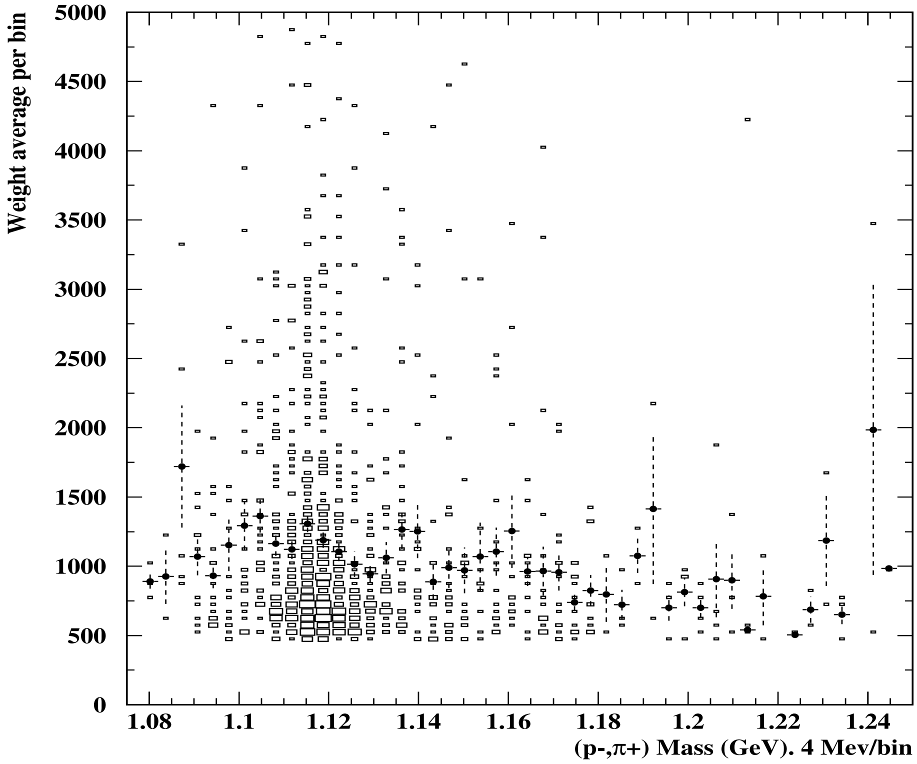

Figure 4.6: Weights (points) vs Λ mass. Lines with error bars show average weight per bin.

V^0 combinatorial mixing scaling, discussed in the next section, see section 4.2.3. The two lines show mass cuts applied to the weighted data. Between these lines the background makes up 24%±10% of the signal. The error however is very large as the Λ peak does not become clearly visible in the background over quite a large range of selections.

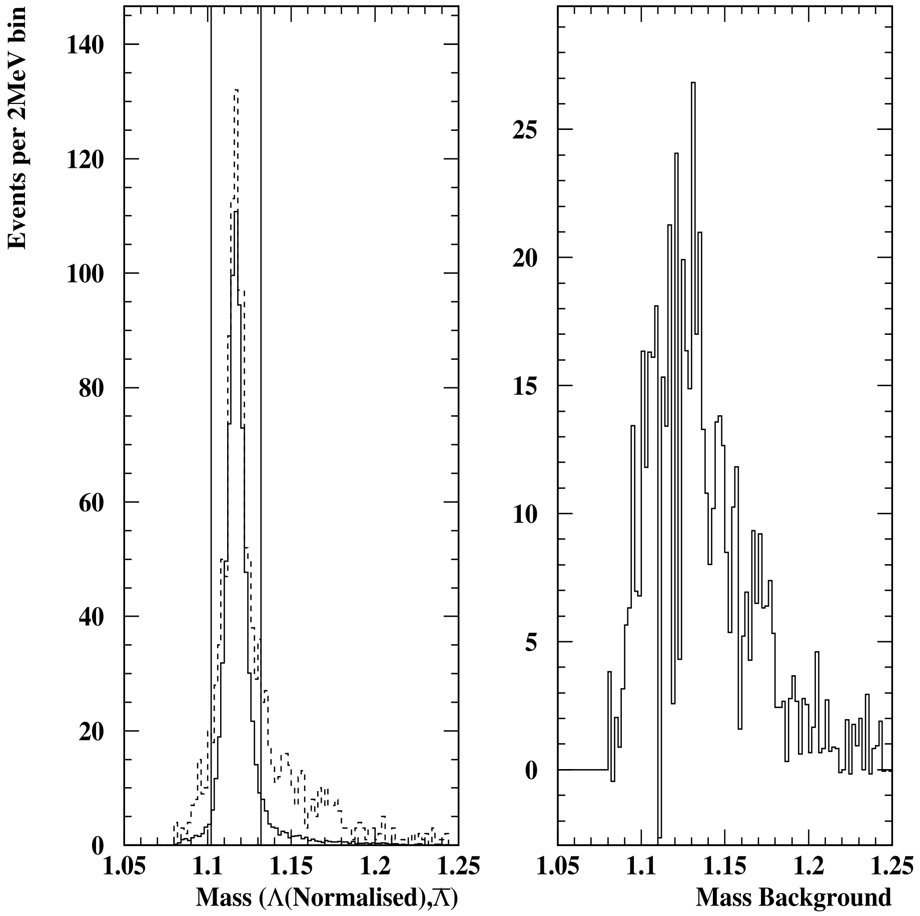

Figure 4.7: Background from $\overline{\Lambda}$ subtracted from 24% normalised Λ signal.

4.2.3 V^0 mixing; Combinatorial Background Subtraction

The previous method was suitable as a first iteration but relies on a fitting procedure to find the normalisation of the background which introduces a large error. If it were possible to generate background from an experimental source that can be normalised to the real data, it should also be possible to generate the normalisation for the background automatically. This is the concept behind the method of V^0 mixing. There are two sets of data available, the two track trigger, (2TT), used in normal data-taking and the data taken with the one track trigger, (1TT), used for normalisation of the final yields, see section 2.6.2

The left hand side of equation (4.2) gives the number of events in the corrected $\overline{\Lambda}$ signal and the right hand side, the 'Signal + Background', the number of events in the uncorrected $\overline{\Lambda}$ signal. The normalised background source is then subtracted from this. Equation (4.3) is used to normalise the background by taking the ratio of combinations of two tracks, per-event, that can be constructed to form a V^0 from all of the 2TT data and the combinations of 1TT 'mixed' V^0s constructed over multiple events. The mixing on the 1TT data sample works by buffering a number of events and mixing every positive track with every negative track. This forms a sample of mixed V^0s which is repeated over the whole 1TT sample.

The combinatorial background, Background_{1TT}, is found after the selections used to find the $\overline{\Lambda}$ signal are applied to mixed 1TT events. This normalised Background that can be subtracted is the last term from equation (4.2).

$$\begin{aligned}
\text{Signal} &= (\text{Signal} + \text{Background}) - \text{Background} && (4.2)\\
\text{Background} &= \text{Background}_{1TT}\frac{\text{Combs}_{2TT\ \text{per-event}}}{\text{Combs}_{1TT\ \text{mixed-events}}} && (4.3)\\
\text{Combs}_{2TT\ \text{per-event}} &= \left({}^{Tracks}\mathbf{C_2} - \left({}^{\mathbf{Tracks+}}\mathbf{C_2} + {}^{\mathbf{Tracks-}}\mathbf{C_2}\right)\right)_{Event} &&\\
&= \frac{1}{2}N_{tracks}(N_{tracks}-1) &&\\
&\quad -\frac{1}{2}N^{+}_{tracks}(N^{+}_{tracks}-1) - \frac{1}{2}N^{-}_{tracks}(N^{-}_{tracks}-1)) &&\\
\textbf{Simplify using } N_{tracks} &= N^{+}_{tracks} + N^{-}_{tracks} &&\\
&= (N^{+}_{tracks} \times N^{-}_{tracks})_{Event} && (4.4)\\
\text{Combs}_{1TT\ \text{mixed-events}} &= (N^{+}_{tracks} \times N^{-}_{tracks})_{All\ data} && (4.5)
\end{aligned}$$

Consider mixing the tracks from the 2TT data set. If these charged tracks are combined over an event, assuming the tracks per event were not correlated, any signal V^0s in the data may have a different distribution to the background in the data. Swapping background tracks across events will have no effect as a majority of background comes from charged pion decays which would give singly charged tracks. This method relies on the amount of signal in the 2TT sample being small with respect to the combinatorial background. If the signal in the 2TT sample is negligible then the normalisation for the background, equation (4.3), is simply the number of possible combinations that can form a V^0, per-event, as shown in equation (4.4) and (4.5).

There are issues to consider for normalising from data that will also generate the $\overline{\Lambda}$ signal, issues that are complicated further by this sample being p-Be and having fewer tracks per-event compared to Pb-Pb collisions. However, the selection procedure showed that the signals after the selection were small compared with the full

2TT data set combinations, and the effects of signal mixing could be assumed small compared to background mixing;

- Total tracks in Λ, $\overline{\Lambda}$ and K_s^0 signal : $\sum(12312)_\Lambda + (911)_{\overline{\Lambda}} + (6160)_{K^0} = 19383$
- Total number of 2 track combinations of charged tracks for all 2TT events : 223429
- 8.6% of the experimental data sample, (2TT), contains signal before selections are applied.

To further validate this assumption the 2TT events were mixed under the same conditions that the 1TT would be mixed and the distributions compared. The one track trigger events would have a negligible signal to background as the two track V^0 condition has been relaxed, the 1TT condition giving less than one real V^0 in 10^9 events.

By comparing the mixed 1TT and the 2TT background distributions, see figure 4.8 the distributions can be seen to follow one another closely, showing that the signal in the 2TT data set is not distorting the mixing process. The background can now be found by normalising the 1TT background to the ratio of 2TT and 1TT combinations.

The corrected $\overline{\Lambda}$ signal compared well with the Λ amplitude and width in figure 4.9. In these two plots the left hand side plot shows the uncorrected $\overline{\Lambda}$ signal with the self normalised 2TT data. Note; this is shown only for clarity as the distributions matched very well in figure 4.8, the 1TT data was used for the final correction. In the right hand side plot of 4.9 the corrected $\overline{\Lambda}$ signal has been normalised to the Λ signal and superimposed. This shows how well the $\overline{\Lambda}$ signal distribution matched the Λ distribution and the lack of any obvious distortion of the $\overline{\Lambda}$ signal from the correction procedure. This correction method was also found to be stable with respect to removing various selections applied simultaneously to the 2TT signal and

1TT mixed background. Table 4.2 gives the final background fractions. Also shown in this table is the background fraction under the Λ, which is reasonable, at around 5% which is within systematics that will be applied to the final sample. The Λ subtracted background found previously, see section 4.2.2, normalised to 24% compares well with the self normalised background. The self normalised 1TT was chosen to correct for the background under the $\overline{\Lambda}$ in the calculation of the final yields and inverse slope.

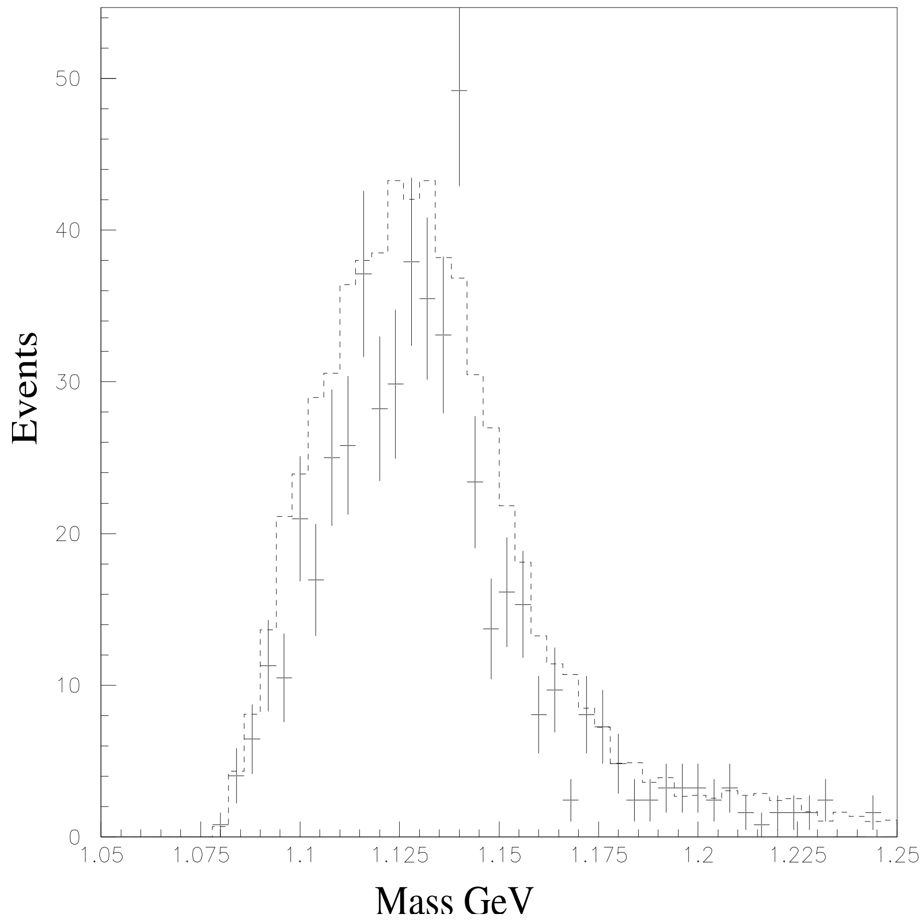

Figure 4.8: 2TT, broken line normalised to 1TT with error bars.

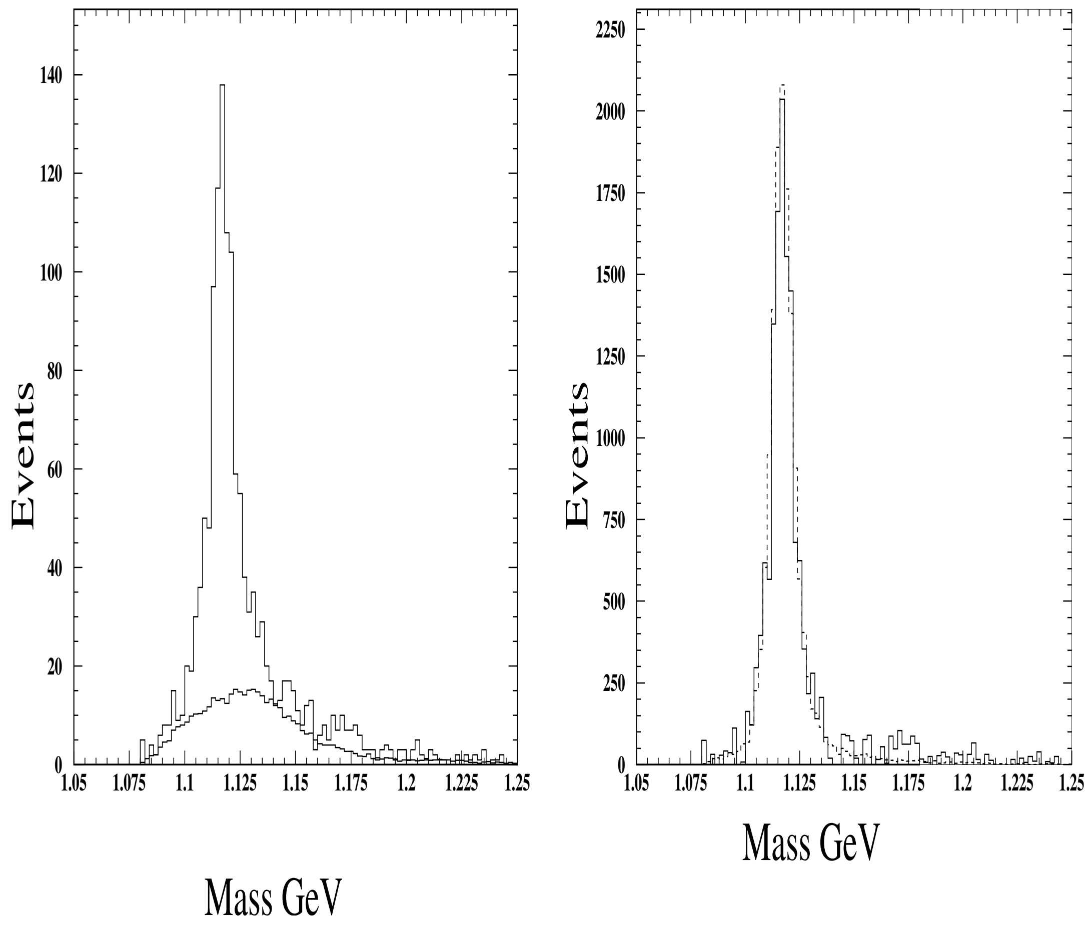

Figure 4.9: Left hand side plot shows $\overline{\Lambda}$ vs. self normalised 2TT mixed background; right hand side plot shows the background subtracted $\overline{\Lambda}$ (solid line) vs. Λ (dashed line).

Table 4.2: Table of corrected $\overline{\Lambda}$ signal for 1TT

1TT (No V^0 trigger)			
Particle	Corrected signal within mass range; $1.102 < \text{GeV} < 1.132$	Background within mass range	Uncorrected signal within mass range
Λ	11814	4.2%	12468
$\overline{\Lambda}$	693	24%	911

4.3 Acceptance Windows, Inverse Slopes and Yields

The two main physics results we can draw from the weighted data are the calculation of the inverse slope and the yield. There are a number of steps to extract this. The first is the definition of a suitable acceptance window. If the weighted transverse mass is plotted vs. rapidity and each weighted particle with a weight greater than a factor of ten times the minimum weight for the sample is highlighted, a clear band is seen around the edges of the sample. This is shown in the plot of weighted Λ decays in figure 4.10. The large points show the high weights and the outline shows the selection that has been defined to remove them. The acceptance plot is related to a distorted view of the compact telescope window. The curved bands are related to the angle at which the V^0 intercepts the beam, see appendix D. The upper and lower curved bands are then found to follow the upper and lower edges of the compact telescope and outline where the V^0 are passing close to the edges of the compact telescope. The high weights can then be described by decays that are close to the edge of the telescope and during the simulation would have had many tracks that pass outside the active telescope volume. This required more attempts to reconstruct the 5000 events required by GEANT giving a higher weight from the numerator in equation (4.1).

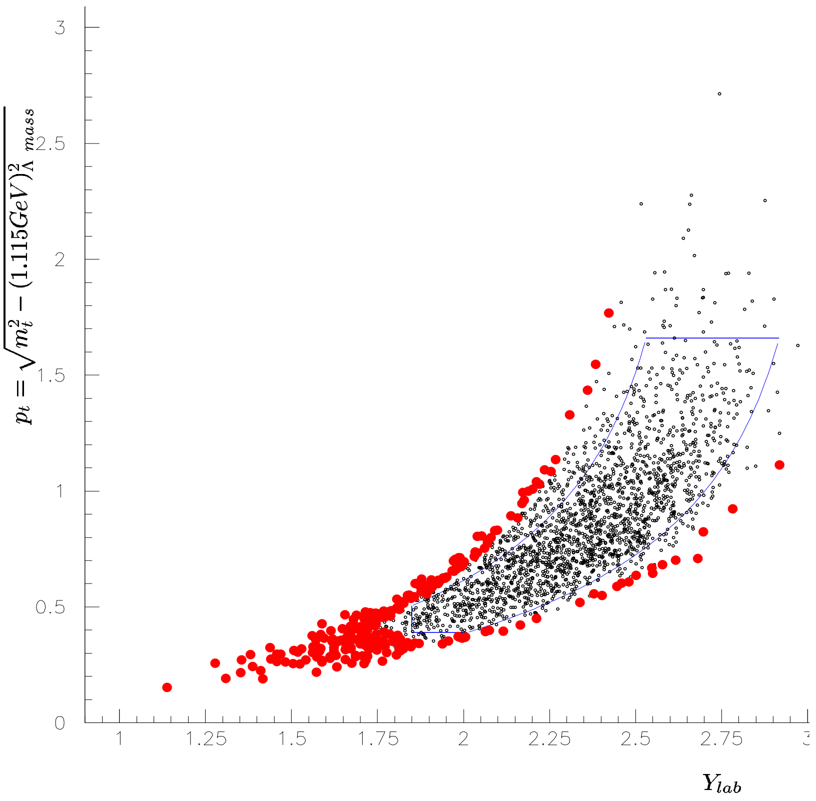

Figure 4.10: Acceptance window for Λ sample. High weights shown as large points.

In order for the final physics results to be independent of experimental conditions, the yields and the inverse slopes are fitted with data inside the window of low weights where the correction procedure works well. This selection defines a clear region where the decays are well within the compact telescope volume eliminating any edge detection effects. The selection was defined by minimum and maximum values for the transverse mass, rapidity and angle of the V^0s line of flight intercept with the beam. The V^0 angle with the beam is translated into a function of transverse mass and rapidity, see appendix D. A further condition was made that the windows chosen for the $\overline{\Lambda}$ and Λ are identical. From section 4.1 it was seen that the selection of the window can introduce a systematic error. A number of windows were chosen to test the stability of the final window and estimate this error, see section 4.4.

4.3.1 Transverse Mass Spectra

Consider a collision in the centre of mass frame. If the colliding particles are assumed to reach thermal equilibrium they will have a Boltzmann distribution of energies. This distribution can be written in terms of the transverse momentum, see equation (4.6), [9]. By fitting the corrected transverse mass spectra obtained from the experiment the inverse slope, $\frac{1}{T}$, will give a measure of the temperature reached during the collision and the value of α depends on the collision dynamics.

$$\frac{dN}{dm_t} \propto m_T^{\alpha} \exp\left(-\frac{m_T}{T}\right) \tag{4.6}$$

$$m_T = \sqrt{p_T^2 + m^2} \tag{4.7}$$

The fit of m_T, the transverse mass, used two methods. For the Λ and the K_s^0 a maximum likelihood method was used. The situation was slightly more complicated for the $\overline{\Lambda}$ as the background had to be accounted for. This method used a combination of maximum likelihood and binned m_t.

4.3.2 Inverse Slope for the $\overline{\Lambda}$

To fit the $\overline{\Lambda}$ signal the m_t distribution was separated into bins. The 1TT background was also separated into identical bins. This allows the background to be subtracted bin by bin. Once the signal in each bin was corrected to compensate for differing rapidity intervals in each m_t slice, an exponential fit was made that allowed the corrected inverse slope to be found. Because the data has been separated into bins and the statistics for the signal are low, the first task was to ensure that the correct bin widths had been chosen and was compatible with the maximum likelihood method. This was achieved by comparing an exponential fit to the binned, uncorrected $\overline{\Lambda}$ signal, to the fit found using the maximum likelihood method. With 8 bins, ranging from 1.18-2.00 in m_t, the binned fit was within 0.4 MeV of the likelihood method. This is an order of magnitude less than the error on the likelihood method and was chosen as a compatible binning.

With this binning the next task was to correct the values, per bin, for the background. Table 4.3 shows these corrections to each bin. The 'weight' is the sum of all the weights per bin, extrapolated to cover one unit of rapidity, 'Signal+Background (Sbg)' the sum of the unweighted events per bin and 'Background (Bg)' is the sum of the unweighted 1TT background events per bin. These background events were selected only within the acceptance window region for compatibility with the signal. Equation (4.8) gives the corrected average weight per bin. The factor of 0.8 in this equation accounts for the 1TT normalisation in equation (4.3).

$$Weight_{corr\ i} = Weight_i \left(\frac{Sbg_i - 0.8Bg_i}{Sbg_i} \right) \tag{4.8}$$

$$\mathrm{Error_i} = \left(\frac{\Delta W^2_{error\ i}(Sbg_i - 0.8Bg_i)^2 + 0.8Bg_i(Sgb_i)^2 Weight_i^2}{Sbg_i} \right)^{\frac{1}{2}} \tag{4.9}$$

With

Where

$$(0.8Bg(m_t)) \quad = \quad (\Delta Background)^2 \tag{4.10}$$

The error on the corrected weight, see equation (4.9) assumes that there are no errors on the unweighted signal events. This is because 'Sbg' defines the particle that is weighted and it is this error, $W_{error\ i}$, that is used.

Table 4.3: Values used for background correction to the $\overline{\Lambda}$ inverse slope

Values within Acceptance Window;					
Bin	Weight with no BG $\times 10^3$	% change	Weight with BG $\times 10^3$	Signal + Background $=Sbg$	Backgound $=Bg_{normalised}$ $(=0.8 \times Bg)$
Low 1	5514	-37%	8822	192	72
2	2847	-21%	3635	180	39
3	1448	-32%	1682	115	16
4	558	-20%	701	59	12
5	298	-6%	318	32	2
6	109	-14%	127	14	2
7	52	-15%	61	7	1
High 8	28	-28%	37	4	1

4.4 Inverse Slopes and Yields

It was found from section 4.1 that a possible source of systematic error could come from the selection of the acceptance window used to remove the high weights. This was estimated by selecting a number of windows for the data to test the stability of the results. Figure 4.11 show four windows used to select the Λ data. With these

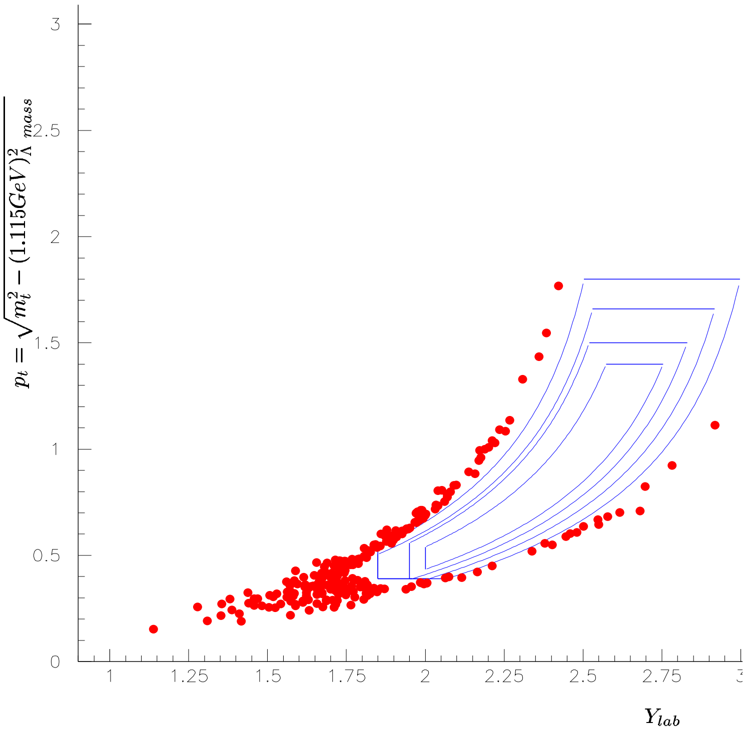

Figure 4.11: Acceptance windows used to test Λ stability. Only high weights are shown for clarity.

selections on the data it is seen that the inverse slope is within errors, with the largest systematic effect on the yield, see figure 4.12. The final windows used to select the signals are shown in table 4.4. The Big/Small values indicate the values used for the larger and smaller windows, used to produce the systematic errors in the final yields table 4.6.

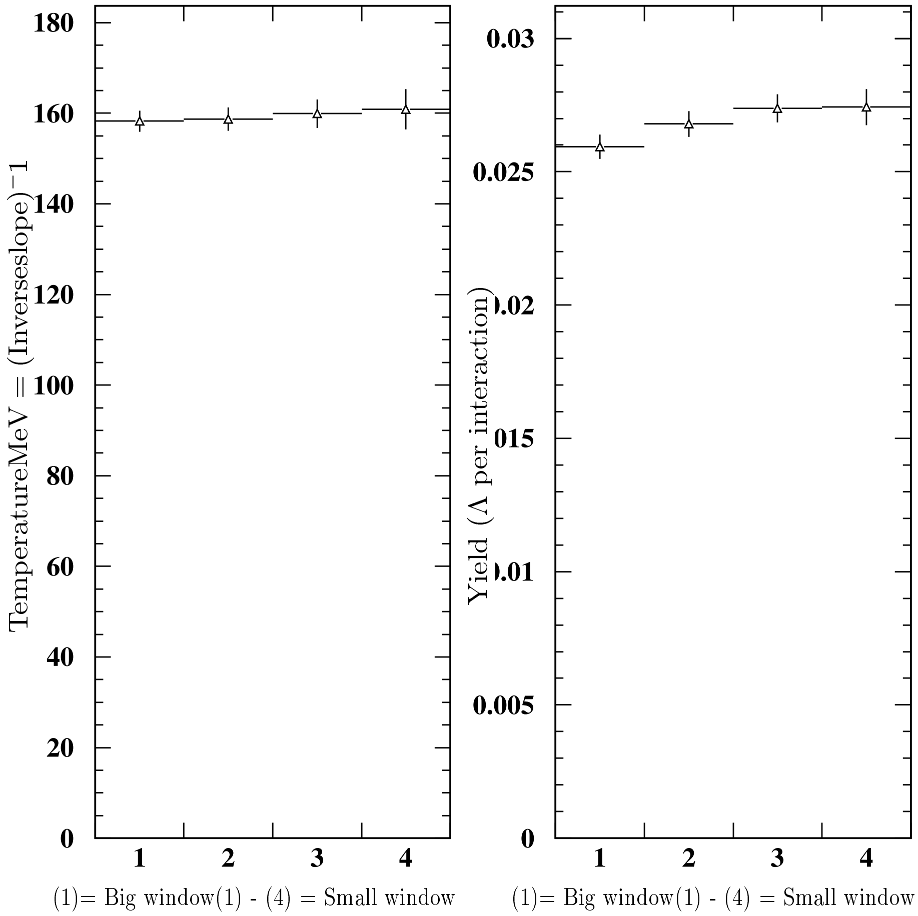

Figure 4.12: Change in inverse slope and yield with acceptance window.

Table 4.4: Windows used to sample data. ($\overline{\Lambda}$ parameters identical to Λ)

Particle	V^0-Beam: θ_{min} (mrads)	V^0-Beam: θ_{max} (mrads)	y_{min}	y_{max}	pt_{min} (GeV/c)	pt_{max} (GeV/c)
Λ Big	85	140	1.85	3	0.39	1.80
Λ Production	90	133	1.85	3	0.39	1.66
Λ Small	100	120	2.00	3	0.39	1.40
K_s^0 Big	-	-	-	-	-	-
K_s^0 Production	90	136	2.52	3	0.53 GeV/c	1.70
K_s^0 Small	95	126	2.52	3	0.60 GeV/c	1.50

4.4.1 Estimation of Systematic Errors

From various simulations of the beam and S4 counter it was deduced that a large effect on the weights could come from the location of the beam along the Z axis. However, the location of the target centre in X at -60 cm located the position of the beam accurately enough to eliminate this effect. The beam spread was not so accurately known but was found to be stable within the limits of the experiment. The next possible systematic cames from the weighting procedure, from section 4.1, with a simulated inverse slope of 169 MeV, the weighted value was 163 MeV, a 4% difference. The definition of the acceptance window is another possible source of error. From figure 4.12 the effect of the window selection on the inverse slope was less than 1%. For the yield, the average value changed by a maximum of 3%. This was also seen in the final yields, where the maximum deviation was found with the K^0 signal at 4%. Finally, a systematic has to be added to take account of normalisation and trigger efficiencies compared with the Pb-Pb data of 7%, see [51]. Together, this estimates a systematic of 8% for the inverse slope and yields. For the WA97 experiment [52], with a similar setup to the NA57 experiment, studies were done to determine the effect of telescope alignment and other effects on the physics results. The systematic here was estimated at 10% so the final systematic error was chosen to agree with WA97 to account for this.

4.4.2 Inverse Slope

The figures 4.13 show histograms binned in m_t for the Λ and $\overline{\Lambda}$ with $\alpha = 1$ from equation (4.6). α is a constant that depends on the dynamics of the system, in the CM frame for Pb-Pb interactions, the equal masses of the colliding ions means that the velocity of the colliding ions were equal and opposite in this frame. For a p-Be collision, the difference in mass would cause a velocity difference in the CM frame that would distort the distribution. α takes account of this, but is currently unknown for p-Be dynamics and could range between 1 and $\frac{3}{2}$. From table 4.5 the difference in the inverse slope is small compared to the statistical error and a value of $\alpha = 1$ was chosen for further analysis to agree with the Pb-Pb inverse slopes. The Λ and K_s^0 slope were found using the maximum likelihood method. The slope for the $\overline{\Lambda}$ is an exponential fitted to the histogram of 8 m_t bins, used to correct the background. The exponential fit shown gives the inverse slope and the errors are calculated using equation (4.9) . Table 4.5 gives the numerical values for the inverse slopes for both values of α.

Table 4.5: Table of inverse slope values for various signals. 40 GeV/c p-Be 1999. First error is statistical, second error is systematic

Particle	Slope (MeV)	Slope (MeV)
	$\alpha = 1$	$\alpha = \frac{3}{2}$
Λ	$158 \pm 3 \pm 16$	$151 \pm 3 \pm 15$
$\overline{\Lambda}$ (Background corrected)	$135 \pm 17 \pm 13$	$130 \pm 17 \pm 13$
K_s^0	$166 \pm 3 \pm 17$	$154 \pm 3 \pm 15$

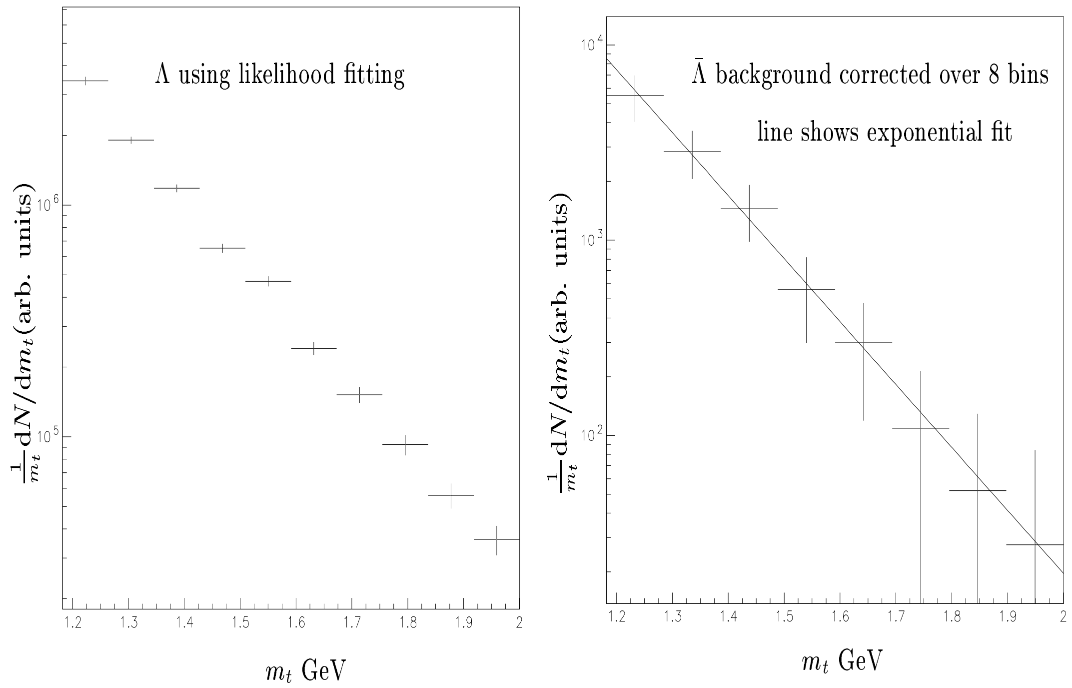

Figure 4.13: Inverse slope for Λ and $\overline{\Lambda}$, where $\alpha = 1$.

4.4.3 Yields

In order to find the yield, or the average particles produced per interaction, it is first necessary to extrapolate the acceptance window over m_t and around mid rapidity to make a common acceptance window. This is performed by binning the data in the region of the experimental acceptance and extrapolating it assuming an exponential distribution in m_t and a flat distribution within rapidity. After the data has been extrapolated the yield is found from equations (4.11) and (4.12).

$$\text{Raw Yield}_{\text{per interaction}} = \sum_{run} \frac{\sum Weights_{run}\left(\frac{Total\ runs}{Weighted\ runs}\right)}{0.08\left(\sum(Beam_{flux\ per\ run})(Protons_{int\ per\ run})\right)} \quad (4.11)$$

$$\text{Yield}_{\text{per interaction}} = \text{Raw Yield}_{\text{per interaction}} * (1 - Bg) * E_f * BR \quad (4.12)$$

For equation (4.11) the $\text{Weights}_{\text{run}}$ distribution has been calculated from the weighting chain for the signal of interest. The other variables are the ratio of total to weighted runs, this accounts for only a sample of the 'Gold Plated' events being used for a signal to reduce computing times. The denominator contains information about the flux of the beam and interaction rate with the target. The value of 0.08 is the number of interaction lengths in the Be target, see section 2.3. The beam flux at the target and fraction of protons were recorded from the target scintillators and Čerenkov counters as part of the trigger, see section 2.6. This is fed into equation 4.11 giving a 'raw' yield that has to be corrected for the background fraction (Bg), Branching Ratio (BR) and Extrapolation factor (E_F) in equation 4.12.

It is possible that the yields may have to be corrected for contamination from 'feed down decays'. This is a source of contamination from other decays, such as a Λ particle from Ξ or Ω decays, that satisfied all the selections but is not a direct Λ from the interaction. However, this source of contamination is very low for the NA57 experiment as the detector is situated close to the target, where feed down decays are less likely and have not been included in the data [53].

For the Pb-Pb collisions the number of participants were found by fitting the Glauber model [35] to the charged track multiplicity distribution. For these p-Be results the multiplicity is calculated by averaging over all possible impact parameters, this gives an average of 2.5 wounded nucleons per interaction [29]. Table 4.6 gives the final yields for the acceptance windows extrapolated, by one unit of rapidity, over mid-rapidity and over all p_t.

Table 4.6: Table of yields for 40 GeV/c p-Be 1999. First error is statistical, second error is systematic

Particle	Particles per interaction, $N_{part} = 2.5$ Final Yield		
Λ	0.0268 $\pm$0.0005 (stat.) $\pm$0.0028 (sys.)		
$\overline{\Lambda}$	0.00196 $\pm$ .00009 (stat.) $\pm$0.00020(sys.)		
K_s^0	0.0218 $\pm$ 0.0005 (stat.) $\pm$0.0022 (sys.)		
$\frac{\overline{\Lambda}}{\Lambda}$	0.073 + 0.004 - 0.002		
Particle	Background correction under signal	BR	E_f
Λ	0%	0.6390	4.0
$\overline{\Lambda}$	24%	0.6390	4.6
K_s^0	0%	0.6895	4.4
K^0	0%	0.6895$\times$2.0	-

Chapter 5

Comparison of 40 GeV/c p-Be with Pb-Pb Data

Table 5.1 compares the p-Be 40 GeV/c inverse slopes found in this thesis with Pb-Pb results from the NA57 runs where the inverse slopes have been taken over maximum centrality. Moving from p-Be interactions to Pb-Pb interactions, at both energies, shows an increase in the inverse slope of the fireball to over 200MeV, well within the region where QGP formation would be expected, see Chapter 1. At both beam energies, the K^0_s has the highest inverse slope in the p-Be interaction. The K^0_s is the most abundantly produced particle and the lightest meson of the group. The most difficult particle to produce through hadronic interactions is the $\overline{\Lambda}$ and this has the lowest inverse slope in p-Be interactions. The increase in inverse slope moving from 40 to 160 GeV/c for p-Be is 11% for K^0_s, 16% for Λ and 16% for $\overline{\Lambda}$. It seems that the increase in inverse slope from moving to the higher beam energy is approximately the same and small, as would be expected if the particles were not undergoing secondary interactions that would allow them to thermalise the increasing K.E. The much higher inverse slope seen in the Pb-Pb interactions suggests that secondary interactions in the colliding volume are allowing the system to thermalise. An interesting point to note here is the similarity of the inverse slope for the Λ and $\overline{\Lambda}$ particles. This suggests that $s\bar{s}$ production from a QGP is thermalising. Another point to note in the Pb-Pb interactions is the inverse slope of the K_s^0, light mesons, is now lower than the Λ and $\overline{\Lambda}$ baryons. A QGP will be undergoing a rapid expansion that has been shown to affect the m_t distributions when fits are made to the 'blast wave model' with the NA57 data [54]. In this model the particles are assumed to be in a local thermal equilibrium in a fireball that is rapidly expanding. It predicts a deviation from the exponential behaviour seen in equation (4.6) at low m_t. Due to its light mass the K^0 spectrum is predicted to be steeper, i.e, having a lower value of the inverse slope. The K^0 mesons would come from a hotter source than the more massive baryons. The more massive baryons are more affected by the flow, producing the effect seen in the table [9].

Table 5.1: Table of inverse slopes comparisons over all centrality. Errors are quoted as statistical (first) and systematic (second). For p-Be a 10% error has been added to the values in table 4.5 for normalisation and experimental alignment systematics. NA57 Pb-Pb events are shown at most central 53% of collisions [55, 54].

	Inverse Slope data at 40 A GeV/c		Inverse Slope data at 160 A GeV/c	
Particle	p-Be (NA57) **T** (MeV)	Pb-Pb (NA57) **T** (MeV)	p-Be (NA57) **T** (MeV)	Pb-Pb (NA57) **T** (MeV)
Λ	158±3±16	261±4±26	180±2	289±7±29
$\overline{\Lambda}$	135±17±14	263±6±26	157±2	287±6±29
K^0	176±3±18	-	197±4	237±4±24

Data for hyperon yields from other experiments is still fairly scarce at the energies mapped by NA57, but experiment NA49 has taken data at the same energies which allows such a comparison. NA49 did not take p-Be data, but has published data for the most central Pb-Pb Λ interactions at 40, 80, 160 A GeV/c. The 40 and 160 A GeV/c inverse slope data have been compared with NA57 160 GeV/c Pb-Pb for a similar centrality and are shown in table 5.2.

Table 5.2: Table of inverse slope comparisons for central events. Errors are quoted as statistical (first) and systematic (second). For the 40GeV/c p-Be results a 10% error has been added to the values in table 4.5 to account for normalisation and experimental alignment systematics. NA57 Pb-Pb events are shown at the most central 5% of collisions, (N_{part}=349±1) and cover one unit of rapidity, $|\mathrm{Y} - \mathrm{Y}_{\mathrm{lab}}| \leq 0.5$ [48, 40]. Results from NA49 are shown in the most central collisions, from maximum centrality (0%) to 7.2% centrality , (N_{part}=349) for 40 A GeV/c and 10%, (N_{part}=335), for 160 A GeV [56] and cover 3.2 units of rapidity $|\mathrm{Y} - \mathrm{Y}_{\mathrm{lab}}| \leq 1.6$

	Inverse Slope data at 40 A GeV/c		Inverse Slope data at 160 A GeV/c		
Particle	p-Be (NA57) **T** (MeV)	Pb-Pb (NA49) **T** (MeV)	p-Be (NA57) **T** (MeV)	Pb-Pb (NA57) **T** (MeV)	(NA49) (NA49) **T** (MeV)
Λ	158±3±16	231 ±8±20	180±2	305±15 ±30	304±16±23
$\overline{\Lambda}$	135±17±14	283 ±16±20	157±2	295±14 ±30	261±12±23

The NA49 160 A GeV/c values for the Λ and $\overline{\Lambda}$ differ by 8% where in the NA57 data this difference is 2%. Another observation that can be made with the 40 GeV/c NA49 data is that the inverse slope found in the Pb-Pb interactions is much greater than 200 MeV. This suggests that QGP formation is still likely at the 40 GeV/c beam momentum.

The inverse slopes showed that the conditions after an interaction would allow a QGP to form at 40 GeV/c. To investigate whether a QGP has formed, data from the yields allows us to generate the strangeness enhancement from equation (5.1). The numerator and denominator of this equation normalise the p-Be and Pb-Pb interactions to their centrality, generating the yield per nucleon. For example, the ratio of the yield per nucleon for Pb-Pb and p-Be would equal one if the yield in the Pb nucleus were simply equal to the yield in the p-Be interaction scaled by the number of wounded nucleons.

$$\text{Enhancement} = \frac{\left(\frac{\text{Yield}}{\text{N}_{\text{part}}}\right)_{Pb-Pb}}{\left(\frac{\text{Yield}}{\text{N}_{\text{part}}}\right)_{p-Be}} \tag{5.1}$$

To compare the measured yields the NA57 collaboration has made a comparison between the NA57 Pb-Pb data taken at 160 A GeV/c with the NA49 published 160 A GeV/c data, showing that particle yields ratios between the two experiments were in good agreement [55], see table 5.3. In the table the $\frac{\overline{\Lambda}}{\Lambda}$ Pb-Pb ratios have been compared as closely as possible with the most central events from both experiments. The values are in good agreement, differing by 12% for 40 A GeV/c and 5% for 160 A GeV/c. Considering that both experiments have a different rapidity range, experimental setup and reconstruction procedure, such a close agreement gives confidence in the data. The data from this thesis, for the p-Be 40 GeV/c interactions, has been compared with the NA57 Pb-Pb 40 A GeV/c data for different centralities. The Pb-Pb interactions were divided into five centrality bins, O-IV.

The centrality of the collisions is proportional to the number of wounded nucleons in the interaction, see table 5.4, the more central the collision, i.e. closer to class IV, the more nucleons were wounded which increases the chance of QGP formation. Figure 5.1 shows the enhancements from the data in table 5.5. The four figures are arranged as follows; with the p-Be data, at 40 GeV/c in the left hand side column and 160 GeV/c in the right hand side column. The top figures show the enhancement for the combined Λ and $\overline{\Lambda}$ sample and the lower figures show the K^0, Λ, and $\overline{\Lambda}$ separately. All the figures show a large enhancement for all signals as the centrality is increased. Small enhancements of a few percent may be explained by nuclear effects such as Cronin enhancement [28] but the particles are clearly experiencing very large enhancements and combined with the data that shows a hierarchy of increasing enhancements with increasing strangeness content of the particle, seen in the 160 A GeV/c data, see figure 1.12, currently, only QGP formation gives a satisfactory answer for these enhancements seen at 40 A GeV/c and 160 A GeV/c beam momenta.

Table 5.3: Comparison of $\frac{\overline{\Lambda}}{\Lambda}$ ratios for NA57 p-Be, Pb-Pb and NA49 Pb-Pb. NA57 Pb-Pb events are shown at the most central collisions, from maximum centrality (0%) to 5% centrality , (N_{part}=349±1) and cover one unit of rapidity, $|\mathrm{Y} - \mathrm{Y_{lab}}| \leq 0.5$ [48, 40]. Results from NA49 are shown in the most central collisions, from maximum centrality (0%) to 7.2% centrality, (N_{part}=349) for 40 A GeV/c and 10%, (N_{part}=335), for 160 A GeV/c [56] and cover 3.2 units of rapidity $|\mathrm{Y} - \mathrm{Y_{lab}}| \leq 1.6$

p-Be		Pb-Pb			
NA57		NA57	NA49	NA57	NA49
40 GeV/c	160 GeV/c	40 A GeV/c	40 A GeV/c	160 A GeV/c	160 A GeV/c
0.0731 ± 0.008	0.32 ± 0.04	0.021 ± 0.003	0.027 ± 0.002	0.133 ± 0.021	0.148 ± 0.019

Table 5.4: The five collision centrality classes for Pb-Pb interactions in NA57. Where shown, 0% centrality is a head on collision (Bin IV) increasing toward peripheral collisions (Bin O). [40]

160 A GeV				
O	I	II	III	IV
62$\pm$ 4 53-40%	121 $\pm$ 4 40-23%	209 $\pm$ 3 23-11%	290 $\pm$ 2 11-5%	349 $\pm$ 1 5-0%
40 A GeV				
57$\pm$ 5 53-40%	119 $\pm$ 5 40-23%	208 $\pm$ 4 23-11%	292 $\pm$ 1 11-5%	346 $\pm$ 1 5-0%

The purpose of the 40 GeV/c experiments was to investigate whether plasma formation continues at lower energy. It would have been expected that running at a lower energy than 160 A GeV/c data may have put us in a region outside plasma formation, but the 40 A GeV/c figures in figure 5.1 show that all the signals are significantly enhanced at this energy, suggesting that plasma formation is still occurring. Comparing the lower two figures in 5.1; for the K^0 and Λ signals from the 40 GeV/c data there is a steeper enhancement compared to the 160 GeV/c data. For the K^0 the enhancement is greater at 40 GeV/c than 160 GeV/c over all centrality ranges, and for the Λ signal the enhancement is greater at 40 GeV/c than 160 GeV/c for the final three bins. For the $\overline{\Lambda}$ the enhancement is roughly equal in both energy ranges. The K^0 and $\overline{\Lambda}$ particles have one strange quark in common with the valence quarks of the colliding lead ion and the $\overline{\Lambda}$ has none. The baryochemical potential has been computed using thermal models from SPS data, giving $\mu_b = 400$ MeV for 40 GeV/c and $\mu_b = 250$ MeV for 160 GeV/c data [57], almost a twofold increase in μ_b at the lower beam momenta. This suggests that the dramatic enhancement of the K^0 and Λ signals in the 40 GeV/c data may be due to a higher baryochemical potential in the plasma as a result of 'Stopping', see section 1.8.1. This effect has been reported by NA49 [58] where a similar strong enhancement at 40 GeV/c, before a saturation at 160 GeV/c, has been seen with the K^+. This has with one quark in common with the valence quarks of the colliding ions and has been normalised to number of π^+. This is shown in figure 5.2, the triangular and square markers show central nucleon-nucleon collisions and the circular markers show proton-proton collisions. The 40 A GeV/c and 160 A GeV/c beam momenta in $\sqrt{s}$ have been marked with lines. No similar enhancement was seen with proton-proton interactions. This peak in enhancement at 40 GeV/c which saturates at higher energies is called a 'Kink'. In the kink region, the plasma is predicted to be more stable, with a longer lifetime, termed the *slow burning* regime [59] where the plasma is not undergoing the same violent longitudinal expansion found in the higher energy plasma.

Table 5.5: Table of yields. p-Be data for 40 A GeV, from table 4.6, the 40 A GeV/c Pb-Pb data had a 10% systematic added to the results. The 40 GeV/c p-Be data had a 10% systematic, combined with the largest error from the window selection procedure, added to the result. Errors shown as statistical (first line) and systematic (second line) . 160 A GeV/c Pb-Pb data quoted from NA57 results 160 GeV/c P-Be data taken from WA97 [48, 60, 61, 62]

Yields at 40 A GeV/c						
Particle	p-Be	Pb-Pb				
		O	I	II	III	IV
Λ	0.0268	1.549	3.824	9.147	15.238	21.117
	$\pm$ 0.0005	$\pm$ 0.133	$\pm$ 0.167	$\pm$ 0.293	$\pm$ 0.532	$\pm$ 0.775
	$\pm$ 0.0028	$\pm$ .155	$\pm$ 0.382	$\pm$ 0.915	$\pm$ 1.524	$\pm$ 2.112
$\overline{\Lambda}$	0.00196	0.044	0.136	0.246	0.350	0.446
	$\pm$ 0.00009	$\pm$ 0.006	$\pm$ 0.008	$\pm$ 0.013	$\pm$ 0.019	$\pm$ 0.030
	$\pm$ 0.00020	$\pm$ 0.004	$\pm$ 0.014	$\pm$ 0.025	$\pm$ 0.035	$\pm$ 0.045
K_s^0	0.0218	1.284	3.693	7.971	14.064	18.384
	$\pm$ 0.0005	$\pm$ 0.172	$\pm$ 0.214	$\pm$ 0.383	$\pm$ 0.679	$\pm$ 1.100
	$\pm$ 0.0022	$\pm$ 0.128	$\pm$ 0.370	$\pm$ 0.797	$\pm$ 1.406	$\pm$ 1.838

.

Yields at 160 A GeV/c						
Particle	p-Be	Pb-Pb				
		O	I	II	III	IV
Λ	0.0344	2.30	5.19	9.5	15.0	18.5
	$\pm$ 0.0005	$\pm$ 0.22	$\pm$ 0.29	$\pm$ 0.5	$\pm$ 0.8	$\pm$ 1.1
	$\pm$ 0.0034	$\pm$ 0.23	$\pm$ 0.52	$\pm$ 0.95	$\pm$ 1.5	$\pm$ 1.85
$\overline{\Lambda}$	0.0111	0.417	0.82	1.60	1.84	2.47
	$\pm$ 0.0002	$\pm$ 0.035	$\pm$ 0.04	$\pm$ 0.07	$\pm$ 0.10	$\pm$ 0.14
	$\pm$ 0.0011	$\pm$ 0.041	$\pm$ 0.082	$\pm$ 0.16	$\pm$ 0.18	$\pm$ 0.24
K_s^0	0.1	3.08	8.14	15.5	21.8	26.2
	$\pm$ 0.01	$\pm$ 0.34	$\pm$ 0.48	$\pm$ 0.8	$\pm$ 1.2	$\pm$ 1.7
	$\pm$0.01	$\pm$ 0.30	$\pm$ 0.81	$\pm$ 1.5	$\pm$ 2.1	$\pm$ 2.6

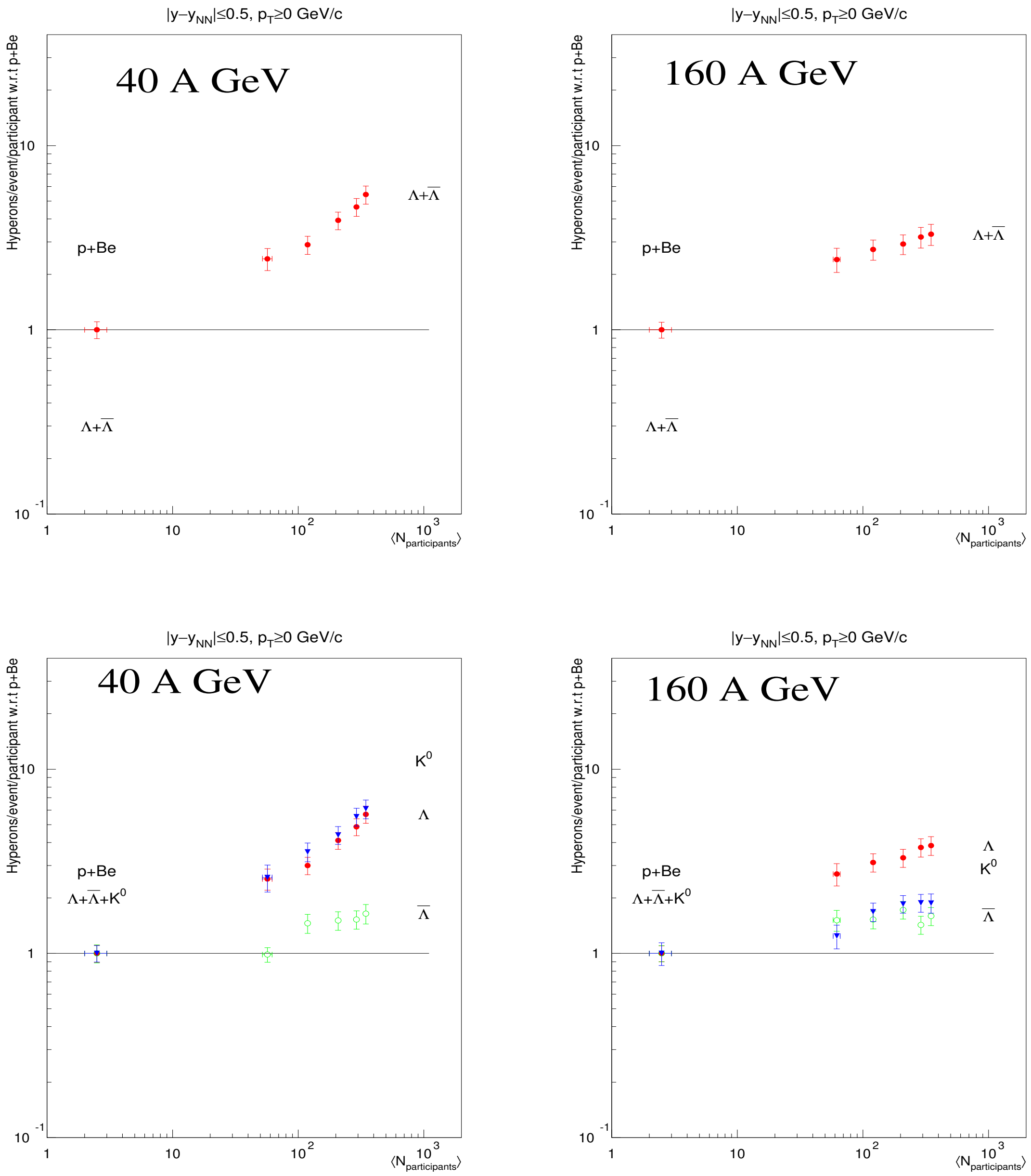

Figure 5.1: Enhancements of NA57 data at 40 and 160 GeV/c. The Y axis shows the enhancement of Pb-Pb interactions (points) with respect to p-Be (line along X) with increasing centrality along the X axis. The left hand column shows 40 GeV/c data and the right hand column 160 GeV/c data. The top row figures shows the combined $\Lambda + \overline{\Lambda}$ signal and the bottom row figures compares the K^0, Λ and $\overline{\Lambda}$ signals

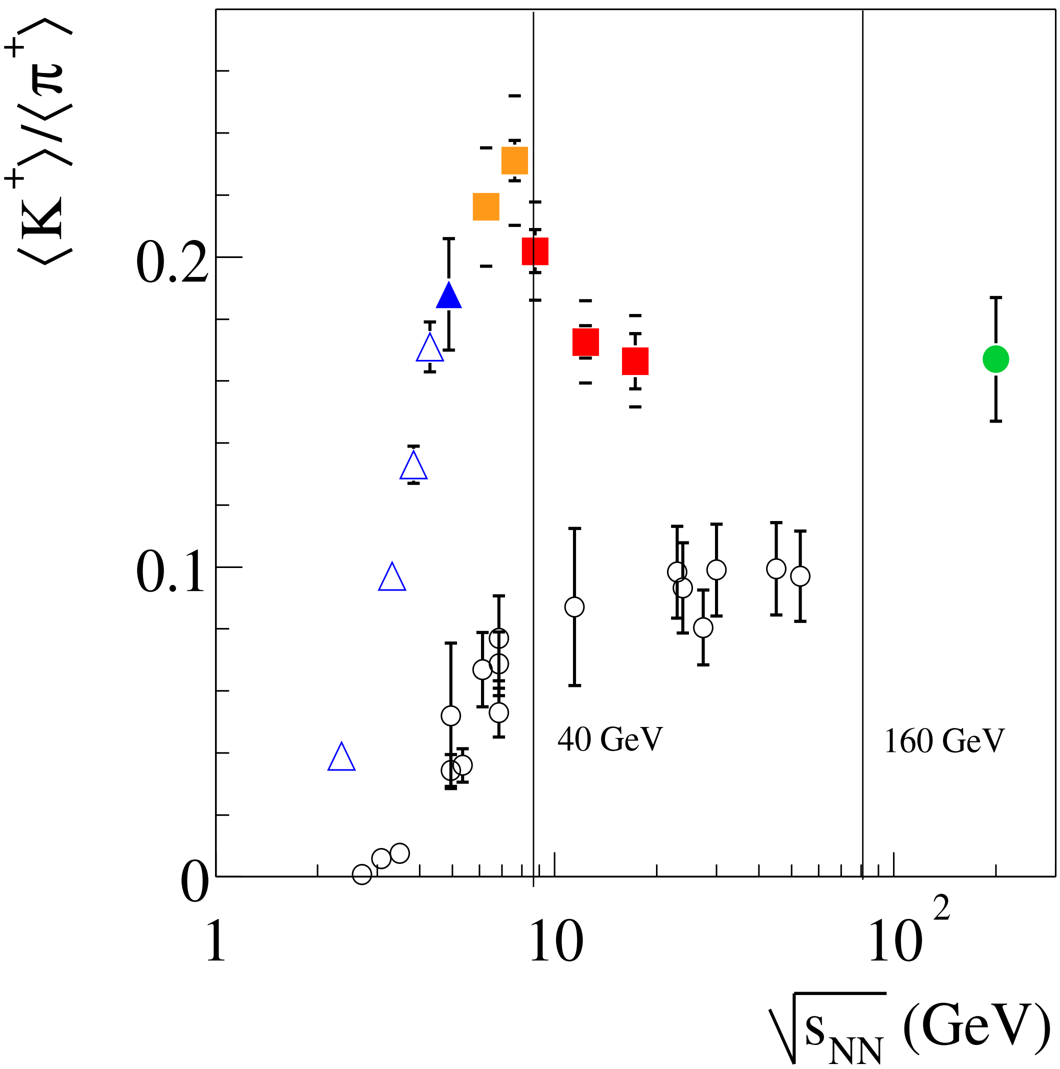

Figure 5.2: K^+/π^+ ratio for increasing $\sqrt{s}$. The triangular and square markers show data for central nucleon-nucleon collisions and the circular markers show proton-proton collisions. The 40 A GeV/c and 160 A GeV/c beam momenta in $\sqrt{s}$ have been marked with lines[58]

Chapter 6

Summary and Conclusions

This thesis began by discussing the QCD vacuum in relation to the Quark Gluon Plasma. This vacuum is not empty but a highly complex structure that accounts for 98% of the mass of hadrons that make up the world around us. The properties of this vacuum mean that the quarks that make hadronic matter are confined to distances of about 1 fm. However, at extreme conditions of temperature or pressure this vacuum may 'melt' and the virtual gluons and $q\overline{q}$ pairs that form it will be released as real particles. Under these conditions, the quarks will no longer be confined by their interactions with the vacuum and their mass will drop to their bare mass. In this state the QGP is said to have been formed.

The NA57 experiment built on the work of the WA97 experiment by measuring over a greater centrality range and extending the measurements down to a lower beam momentum of 40 GeV/c per nucleon. The NA57 experiment was designed to measure strange baryons for P_t greater than 0.5 GeV over one unit of rapidity.

6.0.4 Overview of Results

The subject of this thesis has been the extraction of inverse slopes and yields for the Λ, $\overline{\Lambda}$ and K^0_s particles from the 40 GeV/c p-Be 1999 data sample. After extraction, these signals have been corrected for acceptance and reconstruction efficiencies using a Monte Carlo weighting chain procedure. The background for the $\overline{\Lambda}$ signal has been investigated and corrected using a combinatorial procedure to generate a self-normalised background. From the corrected data the inverse slopes and yields have been calculated and presented in table 4.5 for the inverse slopes and table 4.6 for the yields. The 40 A GeV/c Pb-Pb data from the NA57 experiment was normalised to this data and enhancements were seen for all signals, as shown in the lower two figures in figure 5.1. The enhancements for the K^0 over all centrality and for Λ over the last three centrality bins, which have one valence quark in common with the colliding lead ions, were greater, and increased more steeply, than in the 160 A GeV/c data. The enhancements for the $\overline{\Lambda}$, with no valence quarks in common with the colliding ions, remained roughly constant.

Appendices

Appendix A

Rapidity

In a fixed target experiment the distribution of particles in the laboratory is seen 'boosted' from the CM frame of the interaction of Pb-Pb ions. Spacetime dependent coordinates are not Lorentz invariant so boosting to a different frames changes the distribution of particles. To simplify this a quantity called 'rapidity' is defined. It is a dimensionless variable that is related to the magnitude of the boosted momentum. A boost from the CM frame to the lab frame only changes the rapidity by a constant value and the distribution of particles in the interaction will be preserved. Rapidity is defined using the longitudinal components of momentum. The formula for rapidity is given by equation A.1.

$$y = \frac{1}{2} \ln \frac{E + P_l}{E - P_l} \tag{A.1}$$

where E= Energy, P is the total momentum, $E = (P^2 + M^2)^{1/2}$ and $P_l = P.\cos\theta$ is the longitudinal momentum. The rapidity only changes by a constant under a Lorentz boost, see equation A.2,

$$y' = y + \frac{1}{2} \ln \frac{1 - \beta}{1 + \beta} \tag{A.2}$$

Where β is the velocity of the lab frame with respect to the CM frame. In the CM frame $P_l = y = 0$ and the region around $y = 0$ is called the central rapidity region. This is the region where a QGP is expected to form.

Appendix B

V0 decay Kinematics

In a fixed target experiment the decay products in the CM frame are seen in the laboratory moving along the X axis at close to the speed of light. This is shown in figure B.1. This is related to a 'boost', $\beta = \frac{v}{c}$, where 'v' is the velocity along the X axis and 'c' is the speed of light.

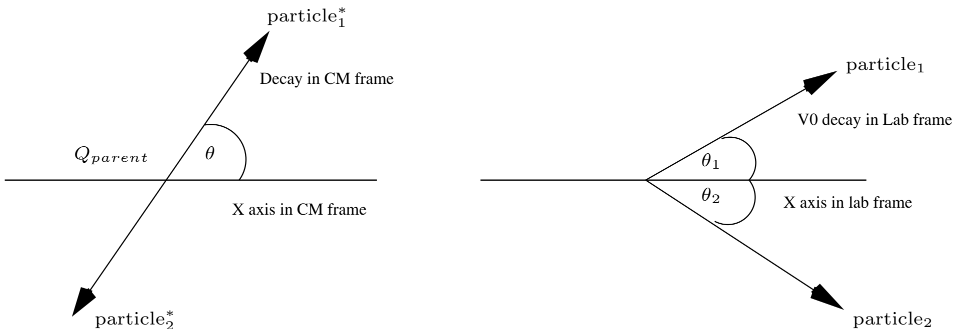

Figure B.1: Two particle decay in the CM and Lab frames.

The conservation of momentum in the centre of mass frame gives the relations between decay particles total, transverse, longitudinal momentum and energy. It also gives their relation to the mass of the original parent particle, Q, in figure B.1

$$|particle_1| = |-particle_2| = P^* \tag{B.1}$$

$$P_t = \sin\theta P^* \tag{B.2}$$

$$P_l = \cos\theta P^* \tag{B.3}$$

$$E_1 = \sqrt{[(P^*)^2 + M_1^2]} \tag{B.4}$$

$$E_2 = \sqrt{[(P^*)^2 + M_2^2]} \tag{B.5}$$

$$M_{parent}^2 = (E_1 + E_2)^2 \tag{B.6}$$

$$\tag{B.7}$$

The transverse momentum, P_t is the same in both frames but the the longitudinal momentum in both frames is related by the boost β,

$$P'_{lab,1} = P'_1 = \gamma(+P_l + \beta E_1) \tag{B.8}$$

$$P'_{lab,2} = P'_2 = \gamma(-P_l + \beta E_2) \tag{B.9}$$

Where $\gamma = 1/\sqrt{1-\beta^2}$
Taking $\frac{P'_t}{P'_l}$ gives θ_1 and θ_2 in terms of θ

$$\theta_1 = \tan^{-1}\left(\frac{\sin\theta P^*}{\gamma(P_l + \beta E_1)}\right) \tag{B.10}$$

$$\theta_2 = \tan^{-1}\left(\frac{\sin\theta P^*}{-\gamma(P_l - \beta E_2)}\right) \tag{B.11}$$

As the velocity along the X axis tends to the speed of light, $\beta \to 1$, $\gamma \to \infty$ and $\frac{P'_t}{P'_l} \to 0$. Therefore θ_1 and θ_2 will tend to zero. So, for a two body decay in the CM frame, with a boost close to the speed of light, the decay products will lie along the direction of the boost, forming the 'Vee' seen in the laboratory shown in figure B.1.

Appendix C

The Podolanski-Armenteros Plot

The Podolanski-Armenteros plot [50] is used to separate mass signals of the various V^0 decays. The transverse component of momentum for the V^0 decay products, Q_t=$P_{t\ V^0}$ is plotted against the Armenteros α, defined by equation C.1.

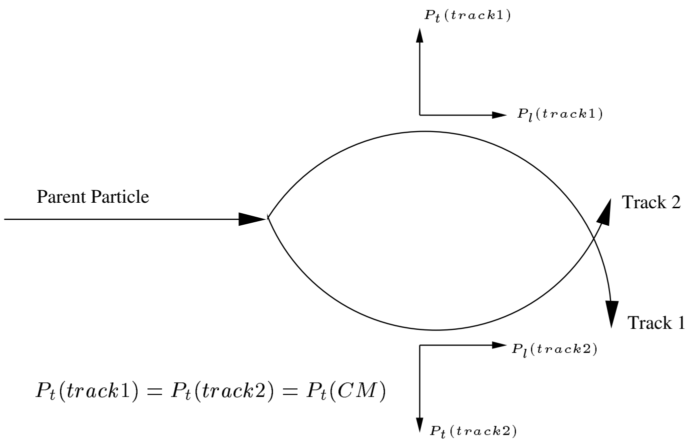

Figure C.1: Track momenta along V0 decay axis.

$$\alpha = \frac{(P_l^{'+} - P_l^{'-})}{(P_l^{'+} + P_l^{'-})} \tag{C.1}$$

Where $\pm$ refer to the charge of the decay track and q_l is the longitudinal component of the momentum along the direction of the V^0 decay, see figure C.1. Boosting to the CM frame, momentum conservation demands that $P_1 = -P_2 = P^*$. See, see equation B.1.

$$E_{1,2}^2 = m_{1,2}^2 + P^{*2} \tag{C.2}$$

$$\alpha = \frac{\gamma(P_l + \beta E_1) - \gamma(-P_l + \beta E_2)}{\gamma(P_l + \beta E_1) + \gamma(-P_l + \beta E_2)} \tag{C.3}$$

$$\alpha = \frac{2P_l + \beta(E_1 - E_2)}{\beta(E_1 + E_2)} \tag{C.4}$$

In the CM the decay $M_{\mathrm{parent}}^2 = (E_1 + E_2)^2$ so, reordering in terms of P_l,

$$P_l = \frac{\alpha\beta M_{\mathrm{parent}}^2 - \beta(E_1 - E_2)}{2} \tag{C.5}$$

Using $P^{*2} = P_l^2 + P_t^2$,

$$1 = \left(\frac{\alpha\beta M_{\mathrm{parent}}^2 - \beta(E_1 - E_2)}{2P^*}\right)^2 + \left(\frac{P_t}{P^*}\right)^2 \tag{C.6}$$

Equation C.6 is the equation of an ellipse with the semi-major axis given by equation C.7

$$\frac{2P^*}{\beta M_{parent}^2}, \tag{C.7}$$

and the semi-minor axis by equation C.8

$$P^*. \tag{C.8}$$

A plot of P_t vs. α will show regions for the V^0 decay as ellipses that are dependent on the momenta and charge of the two decay tracks. With typical V^0 momenta of $P'_{lab} = 10GeV/c$, $\beta \approx 1$ and the ellipse will not depend on the initial momenta of the parent particle, only differences in decay track momenta. Decay tracks of equal mass, e.g. the π^+ π^- decay of the K^0, will give $E_1 - E_2 = 0$ and P_t will have a maximum at $\alpha = 0$. However in a Λ decay most of the momentum will be carried by the positive track (proton) and $E_1 > E_2$. P_t will have a maximum when α is positive. For a $\bar{\Lambda}$ most of the momentum will be carried by the negative track

(anti-proton) and $E_1 < E_2$ giving a maximum of P_t when α is negative.
Selection cuts in α will not only identify M^2_{parent} on the mass of the decay tracks but also whether M^2_{parent} was a particle or an anti-particle. For a V0 type decay, the semi-major axis is related to the parent M_{V^0} and decay tracks $M_{1,2}$ via equation C.9, see [30] and table C.1

$$p^* = \frac{1}{2M_{V^0}}\sqrt{(M_{V^0}+M_1+M_2)(M_{V^0}-M_1-M_2)(M_{V^0}-M_1+M_2)(M_{V^0}+M_1-M_2)} \tag{C.9}$$

Table C.1: Table for identification of particles on the Armenteros plot

V^0 mass	M_1	M_2	p*
1.115 GeV (Λ)	.938 GeV(Proton)	.139 GeV (π)	.101 GeV
.498 GeV (K^o)	.139 GeV (π)	.139 GeV (π)	.206 GeV

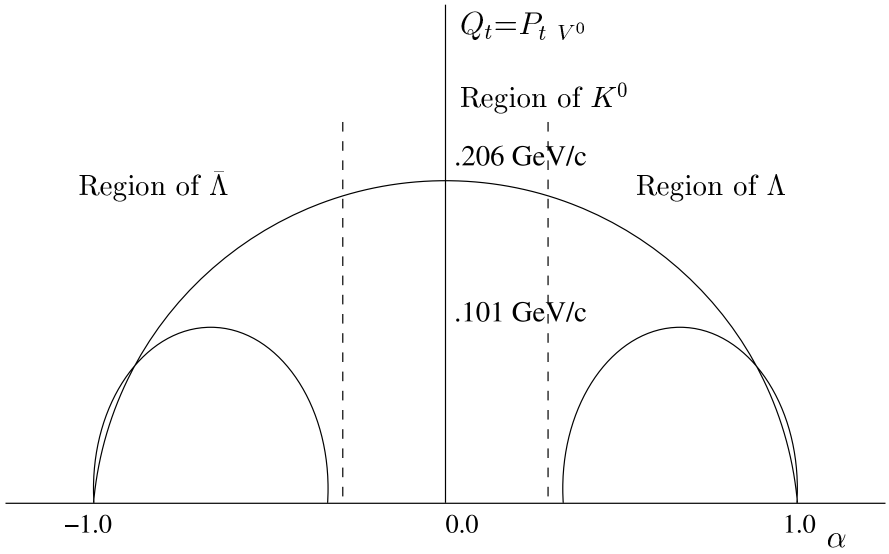

Figure C.2: Decay ellipses for V^0 particles on the Podolanski-Armenteros plot.

Appendix D

Acceptance window

A weighted event was selected if its weight was less than ten times the minimum accepted weight. This selection procedure involved plotting P_t vs. Y_{lab} for the weights and then using the three variables, P_t, the transverse momentum, Y_{lab} the rapidity in the lab frame and ϕ, the angle between the axis of the beam and the axis of the V^0 decay to select the window of weighted events. The angle of the V^0 decay, ϕ, is a function of the $\mathrm{M_{parent}}$, P_t and $\mathrm{Y_{lab}}$ only.

The upper and lower limit of ϕ will be bound by the upper and lower angles that the compact telescope makes with the beam, see fig. 2.4. This selection can be made using a P_t vs. Y_{lab} plot when P_t is expressed as a function of ϕ and Y_{lab}. Starting from the rapidity,

$$Y_{lab} = \frac{1}{2} \ln \left(\frac{E + P_l'}{E - P_l'} \right) \quad \text{(D.1)}$$

$$e^{Y_{lab}} = e^{\frac{1}{2}} \left(\frac{E + P_l'}{E - P_l'} \right) \quad \text{(D.2)}$$

$$e^{2Y_{lab}} = \left(\frac{E + P_l'}{E - P_l'} \right) \quad \text{(D.3)}$$

$$e^{2Y_{lab}} \left(E - P_l' \right) = E + P_l' \quad \text{(D.4)}$$

$$\left(\left(e^{2Y_{lab}} \right) - 1 \right) E = \left(\left(e^{2Y_{lab}} \right) + 1 \right) P_l' \quad \text{(D.5)}$$

$$P_l' = \frac{\left(\left(e^{2Y_{lab}}\right) - 1\right) E}{\left(\left(e^{2Y_{lab}}\right) + 1\right)} \tag{D.6}$$

Using the trig ids. $\frac{\left(e^{y} - e^{-y}\right)}{\left(e^{y} + e^{-y}\right)} = \frac{\sinh y}{\cosh y}$,

$$P_l' = \frac{\sinh y}{\cosh y} E \tag{D.7}$$

The angle of the V^0 decay axis w.r.t to beam is $\phi = \tan^{-1}\left(\frac{P_t'}{P_l'}\right)$,

$$P_l'^2 = \frac{\sinh^2 y}{\cosh^2 y}\left(P_t'^2 + P_l'^2 + M_{parent}\right) \tag{D.8}$$

$$\frac{\sinh^2 y}{\cosh^2 y} = \tau \tag{D.9}$$

$$\frac{P_t'^2}{\tan^2 \phi} = \tau^2 \left(P_t'^2 + \frac{P_t'^2}{\tan^2 \phi} + M_{parent}^2\right) \tag{D.10}$$

$$\tag{D.11}$$

Gathering all the P_t terms gives,

$$P_t = \frac{\tau \tan \phi M_{parent}}{\sqrt{(1-\tau^2) - \tau^2 \tan^2 \phi}} \tag{D.12}$$

$$\cosh^2 y + \sinh^2 \phi = 1 \tag{D.13}$$

$$\tan \phi = \frac{\sin \phi}{\cos \phi} \tag{D.14}$$

$$P_t = \frac{\sinh y \sin \phi M_{parent}}{\sqrt{\cos^2 \phi - \sinh^2 y \sin^2 \phi}} \tag{D.15}$$

A selection on the angle of ϕ, along with minimum and maximum values of P_t and Y_{lab} define an acceptance region of weighted V_0 decays for the final yields.

If this angle is small, as in the case of the NA57 experiments where the typical telescope to beam angle will be of the order of tens of milli-radians, as indicated in figure 2.4, this equation reduces to,

$$P_t = \frac{\sinh y \phi M_{parent}}{\sqrt{1 - \sinh^2 y \phi^2}} \tag{D.16}$$

Bibliography

[1] P. Norman, Private notes taken at NA57 collaboration meeting, *http://wa97.web.cern.ch/WA97/* (2003).

[2] T D Lee, Particle Physics and Introduction to Field Theory, Fourth edition Contemporary Concepts in Physics, pages p395–p401 (June 1990).

[3] F. Halzen and Alan D. Martin, Qarks and Leptons: A Introductory Course In Modern Particle Physics, New York, Usa: Wiley (1984) 396p.

[4] Savely G. Karshenboim, The hydrogen Lamb shift and the proton radius, (1998), hep-ph/0008137.

[5] L. H. Ryder, Quantum Field Theory, Cambridge, Uk: Univ. Pr. (1996) Second Edition.

[6] A. Pich, Quantum Chromodynamics, (1995), hep-ph/9505231.

[7] T. D. Lee, PARTICLE PHYSICS AND INTRODUCTION TO FIELD THEORY, *Contemp. Concepts Phys.* **1**, 1–865 (1981).

[8] S. Margetis, K. Safarik, and O. Villalobos Baillie, Strangeness production in heavy-ion collisions, *Ann. Rev. Nucl. Part. Sci.* **50**, 299–342 (2000).

[9] Jean Letessier and Johann Rafelski, Hadrons and quark - gluon plasma, *Cambridge Monogr. Part. Phys. Nucl. Phys. Cosmol.* **18**, 1–397 (2002).

[10] Krishna Rajagopal, Free the quarks, *SLAC Beam Line* **31N2**, 9–15 (2001).

[11] Simon Hands, The phase diagram of QCD, *Contemp. Phys.* **42**, 209–225 (2001), physics/0105022.

[12] Edward V. Shuryak, the QCD Vacuum and Quark - Gluon Plasma, *Z. Phys.* **C38**, 141–145 (1988).

[13] O. Villalobos Baillie, PhD thesis, School of Physics, University of Birmingham, 1983.

[14] D. Evans, PhD thesis, School of Physics, University of Birmingham, 1992.

[15] M. Le Bellac, Quantum and statistical field theory, Oxford, UK: Clarendon (1991) 592 p.

[16] NA49, Christine Meurer, Hyperon production in Pb + Pb collisions at the CERN-SPS, *J. Phys.* **G30**, S1325–S1328 (2004), nucl-ex/0406016, http://fokay.home.cern.ch/fokay/Press/na49phys.html.

[17] Helmut Satz, The SPS heavy ion programme, (2004), hep-ph/0405051.

[18] Jorgen Randrup, Formation of DCCs with the linear sigma model, (1996), hep-ph/9611228.

[19] F. Mandl, Statistical Physics, The Manchester Physics series, second edition edition.

[20] Ajit M Srivastava, Formation of disoriented chiral condensates in relativistic heavy-ion collisions, *PRAMANA-journal of physics* **55**(1,2), 56–62 (July,August 2000).

[21] F. Cooper, Y. Kluger, E. Mottola, and J. P. Paz, Nonequilibrium quantum dynamics of disoriented chiral condensates, *Phys. Rev.* **D51**, 2377–2397 (1995), hep-ph/9404357.

[22] T. Matsui and H. Satz, J / ψ Suppression by Quark - Gluon Plasma Formation, *Phys. Lett.* **B178**, 416 (1986).

[23] Helmut Satz, A brief history of J/ ψ suppression, (1998), hep-ph/9806319.

[24] NA50, M. Gonin et al., Anomalous J $/\psi$ suppression in Pb + Pb collisions at 158- A-GeV/c, *Nucl. Phys.* **A610**, 404c–417c (1996).

[25] NA38, S. Ramos et al., The Evolution of cross-section ratio psi-prime / J $/\psi$ from p A to S U interactions: Direct photon emmission in correlation with Phi and J $/\psi$, *Nucl. Phys.* **A590**, 117c–126c (1995).

[26] Memorandum: NA57 Status report, SPSC/M663 CERN/SPSC-2001-011, Technical report, CERN, Geneva, 13th March 2001.

[27] STAR, J. Adams et al., Evidence from d + Au measurements for final-state suppression of high p(T) hadrons in Au + Au collisions at RHIC, *Phys. Rev. Lett.* **91**, 072304 (2003), nucl-ex/0306024.

[28] J. W. Cronin et al., Production of hadrons with large transverse momentum at 200-GeV, 300-GeV, AND 400-GeV, *Phys. Rev.* **D11**, 3105 (1975).

[29] P. Norman, PhD thesis, School of Physics, University of Birmingham, 1999.

[30] Springer, Particle Physics Booklet, (June 2002), Available from LBNL and CERN.

[31] NA50, M. C. Abreu et al., Results on open charm from NA50, *J. Phys.* **G27**, 677–684 (2001).

[32] C. Cicalo et al., Study of dimuon and charm production with proton and heavy ion beams at the CERN SPS, CERN-SPSC-99-15.

[33] Lenkeit.B *et al* NA60, Prompt dimuons and D meson production in heavy-ion collisions at the SPS, *nucl-ex/0108015* (14 Aug 2001).

[34] P. Koch, B. Muller, and J. Rafelski, Strangeness in Relativistic Heavy Ion Collisions, *Phys. Rept.* **142**, 167–262 (1986).

[35] NA57, F. Antinori et al., Experiment NA57 at the CERN SPS, *J. Phys.* **G25**, 473–479 (1999).

[36] CERN/SPSLC, WA97 Proposal, Technical report, CERN, Geneva, 1991.

[37] F. Blas et al., Acceleration of lead ions in the CERN PS booster and the CERN PS, Prepared for 16th IEEE Particle Accelerator Conference (PAC 95) and International Conference on High-energy Accelerators (IUPAP), Dallas, Texas, 1-5 May 1995, See http://accelconf.web.cern.ch/accelconf/p95/ARTICLES/MPG/MPG09.PDF.

[38] Lead Ion Accelerating Facility, H. D. Haseroth, The CERN heavy ion accelerating facility, Presented at the 16th Biennial Particle Accelerator Conference - PAC 95, Dallas, TX, USA, 1 - 5 May 1995, See http://accelconf.web.cern.ch/accelconf/p95/ARTICLES/MPG/MPG05.PDF.

[39] NA57 trigger, Private Communication, Lietava, R. and Villalobos Baillie,O. and Evans, D.

[40] NA57, F. Antinori et al., Multiplicity of charged particles in Pb Pb collisions at SPS energies, (2004), hep-ex/0406004.

[41] NA35, T. Alber et al., Charged particle production in proton, deuteron, oxygen and sulphur nucleus collisions at 200-GeV per nucleon, *Eur. Phys. J.* **C2**, 643–659 (1998), hep-ex/9711001.

[42] NA35, P. Foka, Strange particle production in nuclear collisions, *Nucl. Phys.* **A583**, 687c–692c (1995).

[43] E. Andersen et al., Production of Lambda, Anti-lambda, and Xi-, Anti-xi+ particles in S + Pb collisions at 200-GeV/c per nucleon. NA36 Collaboration, *Phys. Lett.* **B327**, 433–438 (1994).

[44] NA36, E. Andersen et al., Results from CERN experiment NA36 on strangeness production, *Nucl. Phys.* **A544**, 309–320 (1992).

[45] WA85 Collaboration: S.Abatziz *et al*, *Nucl. Phys* **A590**, 307c–315c (1995).

[46] WA94 Collaboration: S.Abatziz *et al*, *Nucl. Phys* **A590**, 317c–331c (1995).

[47] Peter Seyboth et al., Search for deconfinement in NA49 at the CERN SPS, *Heavy Ion Phys.* **15**, 257–268 (2002), hep-ex/0206046.

[48] NA57, G. E. Bruno, New results from the NA57 experiment, *J. Phys.* **G30**, S717–S724 (2004), nucl-ex/0403036.

[49] NA57, Logbook for 1999 NA57 p-Be data taking, Technical report, Copy at Birmingham HEP, main document held at CERN by NA57 group.

[50] Podolanski J and R.Armenteros, *Phil. Mag* **45**, 13 (1954).

[51] L. Roman, Internal document from NA57 collaboration for 40 GeV normalisation, *http://wa97.web.cern.ch/WA97/* (2003).

[52] WA97, F. Antinori et al., Transverse mass spectra of strange and multiply-strange particles in Pb - Pb collisions at 158-A-GeV/c, *Nucl. Phys.* **A661**, 481–484 (1999).

[53] WA97, E. Andersen et al., Strangeness enhancement at mid-rapidity in Pb Pb collisions at 158-A-GeV/c, *Phys. Lett.* **B449**, 401–406 (1999).

[54] NA57, F. Antinori et al., Study of the transverse mass spectra of strange particles in Pb - Pb collisions at 158-A-GeV/c, *J. Phys.* **G30**, 823–840 (2004), nucl-ex/0403016.

[55] NA57, F. Antinori et al., Energy dependence of hyperon production in nucleus nucleus collisions at SPS, *Phys. Lett.* **B595**, 68–74 (2004), nucl-ex/0403022.

[56] NA49, T. Anticic et al., Lambda and anti-Lambda production in central Pb - Pb collisions at 40-AGeV, 80-AGeV, and 158-AGeV, *Phys. Rev. Lett.* **93**, 022302 (2004), nucl-ex/0311024.

[57] Peter Braun-Munzinger, Krzysztof Redlich, and Johanna Stachel, Particle production in heavy ion collisions, (2003), nucl-th/0304013.

[58] NA49, M. Gazdzicki et al., Report from NA49, *J. Phys.* **G30**, S701–S708 (2004), nucl-ex/0403023.

[59] C. M. Hung and Edward V. Shuryak, Hydrodynamics near the QCD phase transition: Looking for the longest lived fireball, *Phys. Rev. Lett.* **75**, 4003–4006 (1995), hep-ph/9412360.

[60] G. E. Bruno, K0 production in Pb-Pb at 160 GeV, (10-11th Apr. 2003), Internal notes from NA57 Collaboration meeting.

[61] NA57, F. Antinori et al., Hyperon yields in Pb Pb collisions from the NA57 experiment, Prepared for 31st International Conference on High Energy Physics (ICHEP 2002), Amsterdam, The Netherlands, 24-31 Jul 2002.

[62] WA97, E. Andersen et al., Strangeness enhancement at mid-rapidity in Pb Pb collisions at 158-A-GeV/c, *J. Phys.* **G25**, 181–188 (1999).